

Copyright
by
Onur Taylan
2014

**The Dissertation Committee for Onur Taylan
certifies that this is the approved version of the following dissertation:**

Synthesis Gas Production using Non-thermal Plasma Reactors

Committee:

Halil Berberoglu, Supervisor

Ofodike A. Ezekoye

Matthew J. Hall

John R. Howell

Laxminarayan L. Raja

**SYNTHESIS GAS PRODUCTION
USING NON-THERMAL PLASMA REACTORS**

**by
Onur Taylan, B.S.; M.S.**

Dissertation

Presented to the Faculty of the Graduate School of
The University of Texas at Austin
in Partial Fulfillment
of the Requirements
for the Degree of

Doctor of Philosophy

**The University of Texas at Austin
August 2014**

*To my mother and father
for their unconditional love and support*

Acknowledgements

I would like to thank and express my gratitude to my supervisor, Dr. Halil Berberoglu, for his effort, support and guidance in my doctoral studies over past four years. I would like to thank Dr. Laxminarayan Raja for his discussion and suggestions on my work and bringing the non-thermal reactor geometry to our attention. I would also like to acknowledge my other committee members, Drs. John Howell, Ofodike Ezekoye, and Matthew Hall for serving on my committee, reviewing my work, their support, discussion and suggestions.

I would like to express my genuine appreciation to Dr. Derek Baker. Without his support and encouragement, I may not have pursued doctoral studies and academic career. I would also like to express my gratitude to Dr. Bilgin Kaftanoglu for his advices and guidance.

I would like to sincerely thank Dr. Altan Ozkan, Dr. Thomas Murphy and Akhil Kulkarni for their friendship and generous help in my studies. I would also like to acknowledge Dr. Onur Ferhanoglu for his discussion on the equivalent circuit modeling of my experimental setup, Dr. Jayant Sirohi for his guidance in eliminating electric field interference, and Daniel Pinero for taking the microscope pictures of the reactor and for his help on the electrode degradation part of this study. I would also like to thank all the previous and current officemates of the Solar Energy and Renewable Fuels Lab, here in Austin, TX for creating a friendly working environment: Angel Wileman, Edwin Peng, Andrew Gilbert, Babak Nasouri, Mahesh Vankatesan, Luis Galindo, Rudy Torres, David Navar, Ethan Rohrer, Keith Macon, Cody Bond, Joey Anthony, Daniel Campbell and Begum Baysan. Additionally, I had the privilege to meet many individuals throughout my

journey. I cannot fully express my appreciation and pleasure enough to all of my dear friends for the good times we shared and their encouragement in difficult times. Without them, this study would not be possible.

I would also like to express my grateful feelings to my parents, to whom this dissertation is dedicated, for their unconditional love and support on my decisions at any point of my life. At this point, it is so much momentous than ever to have them by my side. I am forever indebted to them.

Finally, I would like to acknowledge National Science Foundation, Heat Transfer Division of American Society of Mechanical Engineers, Office of Graduate Studies and Graduate Engineering Council at The University of Texas at Austin for their financial support in various conferences that I attended during my doctoral studies.

Synthesis Gas Production using Non-thermal Plasma Reactors

Onur Taylan, Ph.D.

The University of Texas at Austin, 2014

Supervisor: Halil Berberoglu

Today we face the formidable challenge of meeting the fuel needs of a growing population while minimizing the adverse impacts on our environment. Thus, we search for technologies that can provide us with renewable fuels while mitigating the emission of global pollutants. To this end, use of non-thermal plasma processes can offer novel methods for efficiently and effectively converting carbon dioxide and water vapor into synthesis gas for the production of renewable fuels. Particularly, non-thermal plasma technologies offer distinct advantages over conventional methods including lower operating temperatures, reduced need for catalysts and potentially lower manufacturing and operation costs. The non-thermal plasma reactors have been studied for ozone generation, material synthesis, decontamination, thruster for microsattellites, and biomedical applications. This dissertation focuses on producing synthesis gas using a non-thermal, microhollow cathode discharge (MHCD) plasma reactor.

The prototype MHCD reactor consisted of a mica plate as a dielectric layer that was in between two aluminum electrodes with a through hole. First, electrical characterization of the reactor was performed in the self-pulsing regime, and the reactor was modeled with an equivalent circuit which consisted of a constant capacitance and a variable, negative differential resistance. The values of the resistor and capacitors were

recovered from experimental data, and the introduced circuit model was validated with independent experiments. Experimental data showed that increasing the applied voltage increased the current, self-pulsing frequency and average power consumption of the reactor, while it decreased the peak voltage. Subsequently, carbon dioxide and water vapor balanced with argon as the carrier gas were fed through the hole, and parametric experiments were conducted to investigate the effects of applied voltage (from 2.5 to 4.5 kV), flow rate (from 10 to 800 mL/min), CO₂ mole fraction in influent (from 9.95% to 99.5%), dielectric thickness (from 150 to 450 μm) and discharge hole diameter (from 200 to 515 μm) on the composition of the products, electrical-to-chemical energy conversion efficiency, and CO₂-to-CO conversion yield. Within the investigated parameter ranges, the maximum H₂/CO ratio was about 0.14 when H₂O and CO₂ were dissociated in different reactors. Additionally, at an applied voltage of 4.5 kV, the maximum yields were about 28.4% for H₂ at a residence time of 128 μs and 17.3% for CO at a residence time of 354 μs. Increasing residence time increased the conversion yield, but decreased the energy conversion efficiency. The maximum energy conversion efficiency of about 18.5% was achieved for 99.5% pure CO₂ at a residence time of 6 μs and an applied voltage of 4.5 kV. At the same applied voltage, the maximum efficiency was about 14.8% for saturated CO₂ at a residence time of 12.8 μs. The future work should focus on optimizing the conversion yield and efficiency as well as analyzing the temporal and spatial changes in the gas composition in the plasma reactor.

Table of Contents

Table of Contents	ix
List of Tables	xiii
List of Figures	xiv
Chapter 1 Introduction	1
1.1 Motivation.....	1
1.2 Objectives of the Study.....	5
1.3 Organization of the Dissertation	6
Chapter 2 Current State of Knowledge.....	8
2.1 Conventional Dissociation Methods	8
2.1.1 Thermolysis.....	8
2.1.2 Thermochemical Cycles.....	9
2.1.3 Cracking of Gaseous Hydrocarbons	14
2.1.4 Gasification and Reforming of Coal and Biomass	17
2.2 Introduction to Plasmas.....	19
2.2.1 Different Operating Regimes of Plasma	22
2.2.2 Electron Avalanche (Townsend Breakdown) Mechanism	24
2.2.3 Paschen Curve.....	26
2.2.4 Glow Discharge	31
2.2.5 Hollow Cathode Discharge	35
2.3 Plasma Dissociation	36
2.3.1 Plasma Studies and Plasma Reactor Designs.....	36
2.3.2 Microdischarge Plasma Studies	46
2.4 State-of-the-art Syngas Production Methods from CO ₂ and H ₂ O	51
Chapter 3 Materials and Methods.....	54
3.1 Microhollow Cathode Discharge Reactor Prototype	54
3.2 Experimental Setup.....	55

3.3 Analyses.....	57
Chapter 4 Electrical Characterization Model of MHCD Plasma Reactor	60
4.1 Introduction.....	60
4.2 Current State of Knowledge.....	61
4.3 Experimental Parameters.....	67
4.4 Results.....	68
4.4.1 Experimental Characterization of the Reactor.....	68
4.4.2 Equivalent Circuit Model.....	73
4.4.3 Analysis.....	75
4.4.4 Modeling Parameters and Simulation Results	76
4.5 Chapter Summary	80
Chapter 5 Dissociation of Carbon Dioxide using MHCD Plasma Reactor	82
5.1 Introduction.....	82
5.2 Experimental Parameters.....	83
5.3 Results and Discussion	84
5.3.1 Effects of Applied Voltage	86
5.3.2 Effects of Flow Rate.....	89
5.3.3 Effects of Concentration	93
5.3.4 Assessment of Electrode Degradation	96
5.3.5 Implications on the Operation of MHCD Reactor for CO ₂ Dissociation.....	99
5.4 Chapter Summary	100
Chapter 6 Dissociation of Water-Saturated Carbon Dioxide using MHCD Plasma Reactor	102
6.1 Introduction	102
6.2 Experimental Parameters.....	103
6.3 Results and Discussion	104
6.3.1 Voltage and Current Characteristics of Dissociation Process.....	104
6.3.2 H ₂ and CO Generation from Saturated Ar and CO ₂	109

6.4 Chapter Summary	115
Chapter 7 Effects of Design Parameters on Dissociation using MHCD Plasma Reactors.....	116
7.1 Introduction.....	116
7.2 Experimental Parameters	117
7.3 Results and Discussion	119
7.3.1 Effects of Dielectric Thickness on Dissociation.....	120
7.3.2 Effects of Discharge Hole Diameter on Dissociation.....	125
7.4 Chapter Summary	130
Chapter 8 Summary, Conclusions and Recommendations.....	131
8.1 Summary.....	131
8.2 Conclusions.....	136
8.3 Recommendations for Future Research.....	139
Appendices.....	143
Appendix A Nomenclature	144
Appendix B Numerical Codes Used in the Study.....	146
B.1 Paschen Curve Calculation.....	146
B.2 Energy Efficiency and Conversion Yield Calculation	147
Appendix C Gas Chromatograph Analysis.....	151
C.1 Calibration of Gas Chromatograph	151
C.1.1 Carbon Dioxide	152
C.1.2 Methane.....	153
C.1.3 Carbon Monoxide.....	154
C.1.4 Hydrogen.....	155
C.1.5 Oxygen	156
C.1.6 Nitrogen.....	157
C.2 Sample Chromatogram.....	157

Appendix D Modeling of Electric Field Distribution in a Microhollow Cathode	
Discharge Reactor prior to Carbon Dioxide Dissociation	161
D.1 Modeling Analysis	162
D.1.1 Governing Equation	163
D.1.2 Boundary and Initial Conditions	164
D.1.3 Material Properties	164
D.1.4 Method of Solution	164
D.2 Simulation Results	166
D.2.1 Effects of Dielectric Material and Applied Voltage	166
D.2.2 Effects of Hole Size and Dielectric Thickness.....	169
D.3 Modeling Summary.....	171
References.....	173

List of Tables

Table 2.1.	Summary of thermochemical cycles [50].	13
Table 2.2.	Compositions of natural gas from different sources [55].	15
Table 2.3.	Operating conditions of different reactor designs for methane cracking.	16
Table 2.4.	Parameters for calculation of breakdown voltage [25, 75, 83].	28
Table 2.5.	Work function of some metal electrodes [84].	30
Table 2.6.	Conversion and energy cost for methane reforming into C ₂ hydrocarbons and H ₂ using different atmospheric non-thermal plasma discharge methods [104].	46
Table 4.1.	Coefficients used in Equation (4.2), and parameters used in the equivalent circuit model.	78
Table C.1.	Sample gas chromatograph results of Channel 1 (FID) for CO ₂ dissociation at different applied voltages and inlet flow rate of 100 mL/min.	159
Table C.2.	Sample gas chromatograph results of Channel 2 (TCD) for CO ₂ dissociation at different applied voltages and inlet flow rate of 100 mL/min.	160
Table D.1.	Electrical properties of the materials used in MHCD plasma reactor simulations at room temperature and pressure [151].	165
Table D.2.	Lower and upper limits for operating voltage range of microdischarge plasma reactor.	167

List of Figures

Figure 1.1.	Comparison of different fuels in terms of their energy produced and CO ₂ emission [3].	2
Figure 1.2.	Schematic for the synthetic fuel production and carbon and hydrogen cycles for carbon neutral fuel generation and use.	3
Figure 2.1.	Flowchart for thermochemical hydrogen production from zinc-oxide using concentrated solar energy [40].	11
Figure 2.2.	Classification of plasmas in terms of electron temperatures and number densities [25, 75].	20
Figure 2.3.	Voltage and current characteristics of DC discharges [25, 75].	24
Figure 2.4.	Schematic illustrating the Townsend breakdown mechanism and electron avalanche [81].	25
Figure 2.5.	Paschen curves for selected gases.	29
Figure 2.6.	The glow discharge regions and the distribution of some key parameters between the electrodes [25, 75].	34
Figure 2.7.	Schematic of a hollow cathode discharge [80].	35
Figure 2.8.	Schematic of plasma reactor design of Subrahmanyam <i>et al.</i> [87].	37
Figure 2.9.	Experimental representation of Jahanmiri <i>et al.</i> [89].	39
Figure 2.10.	Different plasma reactor designs given in Indarto [90]; (a) Larkin <i>et al.</i> [93], (b) Okumoto and Mizuno [96], (c) Nozaki <i>et al.</i> [97].	41
Figure 2.11.	Experimental setup of Mfora <i>et al.</i> [98].	42
Figure 2.12.	DBD reactor by Siemens, Germany [101].	44
Figure 2.13.	Schematic of the experimental setup for the study of Zheng <i>et al.</i> [103].	46
Figure 2.14.	Schematic of hybrid DBD microdischarge plasma reactor by Shin and Raja [105].	47
Figure 2.15.	Schematic of and pressure distribution within the tubular microdischarge thrusted modeled by Sitaraman and Raja [18].	48
Figure 2.16.	Schematic of microdischarge device modeled by Kushner [107].	50
Figure 3.1.	Schematic of the microdischarge reactor used in the study, (a) cross-sectional, and (b) top view.	55

Figure 3.2.	(a) Schematic, (b) picture of the experimental setup (gas chromatograph, relative humidity controller and CO ₂ /H ₂ O gas analyzer not shown in the picture), and (c) close-up picture of the reactor with flow chamber.	56
Figure 4.1.	(a) The equivalent circuit proposed by Hsu and Graves [120], and (b) corresponding current and (c) voltage characteristics.	62
Figure 4.2.	(a) The equivalent circuit model by Aubert <i>et al.</i> [121], and (b) simulated voltage and current results at applied voltages of 1 kV (solid lines) and 2 kV (dashed lines).	63
Figure 4.3.	(a) Proposed equivalent circuit by Chabert <i>et al.</i> [122], (b) the modeled resistance as a function of discharge current, and (c) the simulated voltage and current characteristics of the proposed circuit.	65
Figure 4.4.	Comparison of experimental and simulated results by Lazzaroni and Chabert [123], (a) voltage, and (b) current as functions of time.	66
Figure 4.5.	(a) The equivalent circuit proposed by Du <i>et al.</i> [125], and (b) corresponding simulation results.	67
Figure 4.6.	Voltage and current characteristics of the MHCD plasma reactor used in the experiments of this study at an applied voltage of 2000 V, (a) voltage and current as a function of time, (b) impedance of the reactor as a function of current.	70
Figure 4.7.	(a) Peak, time-averaged and minimum current, (b) peak and time-averaged voltage (c) time-averaged power and self-pulsing frequency as functions of applied voltage.	72
Figure 4.8.	Equivalent circuit of the experimental setup.	74
Figure 4.9.	Comparison of experimental data and modeling results for (a) voltage across and (b) current through the reactor as functions of time.	79
Figure 4.10.	Comparison of experimental data and modeling results for peak and average power required for the reactor as functions of applied voltage.	80
Figure 5.1.	Voltage and current of the MHCD plasma reactor as a function of time in the self-pulsing regime.	85
Figure 5.2.	Concentrations of CO ₂ , O ₂ and CO in the reactor effluent as a function of applied voltage at a flow rate of 100 mL/min.	87
Figure 5.3.	Average energy density and self-pulsing frequency as a function of applied voltage at a flow rate of 100 mL/min.	88

Figure 5.4.	Electrical-to-chemical energy conversion efficiency and CO ₂ -to-CO conversion yield as a function of applied voltage at a flow rate of 100 mL/min.....	89
Figure 5.5.	Concentrations of CO ₂ , O ₂ and CO in the reactor effluent as a function of inlet flow rate at an applied voltage of 4.5 kV.	91
Figure 5.6.	Average energy density and frequency of self-pulsing discharges as a function of inlet flow rate at an applied voltage of 4.5 kV.....	92
Figure 5.7.	Power efficiency and CO ₂ -to-CO conversion yield as a function of inlet flow rate at an applied voltage of 4.5 kV.....	93
Figure 5.8.	Concentrations of CO ₂ , O ₂ and CO in the reactor effluent as a function of inlet CO ₂ concentration at a total inlet flow rate of 100 mL/min and an applied voltage of 4.5 kV.....	94
Figure 5.9.	Average energy density and self-pulsing frequency as a function of inlet CO ₂ concentration at a total inlet flow rate of 100 mL/min and an applied voltage of 4.5 kV.....	95
Figure 5.10.	Electrical-to-chemical energy conversion efficiency and CO ₂ -to-CO conversion yield as a function of inlet CO ₂ concentration at a total inlet flow rate of 100 mL/min and an applied voltage of 4.5 kV.....	96
Figure 5.11.	(a) Microscope image of the reactor after 25 minutes of operation showing the affected electrode region around the discharge hole, and (b) degraded electrode diameter and area as a function of time for MHCD reactor operated in stagnant air at an applied voltage of 4.5 kV.....	98
Figure 6.1.	(a) Voltage drop across and (b) current through the reactor as functions of time for H ₂ O-saturated CO ₂ , H ₂ O-saturated Ar and 99.5%-pure CO ₂ at a flow rate of 10 mL/min and an applied voltage of 4.5 kV.....	107
Figure 6.2.	Time-averaged discharge voltage versus time-averaged discharge current of the experimental cases at flow rates of 10, 50 and 100 mL/min and an applied voltage of 4.5 kV.	109
Figure 6.3.	Concentrations of gases in the reactor effluent as functions of inlet flow rate for (a) H ₂ O-saturated Ar, and (b) H ₂ O-saturated CO ₂	111
Figure 6.4.	(a) Conversion yield, (b) average discharge power and energy conversion efficiency as functions of inlet flow rate.....	113
Figure 7.1.	Breakdown voltage for CO ₂ as a function of pressure times the discharge distance, and the breakdown voltages that correspond to the discharge distances used in this study.....	119

Figure 7.2.	Concentrations of CO ₂ , CO and O ₂ in the reactor effluent as functions of residence time for three different dielectric thicknesses. The legend shows the dielectric thickness in μm.	121
Figure 7.3.	Energy density and self-pulsing frequency of the microdischarge plasma reactor as functions of residence time for three different dielectric thicknesses. The legend shows the dielectric thickness in μm.	123
Figure 7.4.	Energy conversion efficiency and CO ₂ -to-CO conversion yield of the microdischarge reactor as functions of residence time for three different dielectric thicknesses. The legend shows the dielectric thickness in μm.	124
Figure 7.5.	Concentrations of CO ₂ , O ₂ and CO in the reactor effluent as functions of residence time for three different hole diameters. The legend shows the hole diameter in μm.	126
Figure 7.6.	(a) Energy density, and (b) self-pulsing frequency of the microdischarge plasma reactor as functions of residence time for three different hole diameters. The legend shows the hole diameter in μm.	128
Figure 7.7.	(a) Electrical-to-chemical energy conversion efficiency, and (b) CO ₂ -to-CO conversion yield as functions of residence time for three different hole diameters. The legend shows the hole diameter in μm.	129
Figure C.1.	Calibration curve for carbon dioxide.	152
Figure C.2.	Calibration curve for methane.	153
Figure C.3.	Calibration curve for carbon monoxide.	154
Figure C.4.	Calibration curve for hydrogen.	155
Figure C.5.	Calibration curve for oxygen.	156
Figure C.6.	Calibration curve for nitrogen.	157
Figure C.7.	Sample chromatogram of Channel 1 (FID) of the gas chromatograph for CO ₂ dissociation at different applied voltages and an inlet flow rate of 100 mL/min.	158
Figure C.8.	Sample chromatogram of Channel 2 (TCD) of the gas chromatograph for CO ₂ dissociation at different applied voltages and an inlet flow rate of 100 mL/min.	159
Figure D.1.	Maximum electric field in the gas and the dielectric as a function of applied voltage for the microdischarge plasma reactor with aluminum electrodes.	167

Figure D.2. Estimated discharge gas volume as a function of applied voltage for the MHCD plasma reactor with aluminum electrodes and mica as the dielectric material.....	168
Figure D.3. Required power as a function of applied voltage for the MHCD plasma reactor with aluminum electrodes.....	169
Figure D.4. Estimated discharge gas volume as a function of discharge hole diameter of the MHCD plasma reactor at an applied voltage of 10 kV with aluminum electrodes and mica as the dielectric material.	170
Figure D.5. Estimated discharge gas volume as a function of dielectric thickness of the MHCD plasma reactor at an applied voltage of 10 kV with aluminum electrodes and mica as the dielectric material.	171

Chapter 1

Introduction

1.1 MOTIVATION

Limited reserves of fossil fuels and their negative environmental effects impose significant problems in our energy security and sustainability. Figure 1.1 shows the energy potential and carbon emissions by most commonly used fuels along with hydrogen. Carbon dioxide as combustion product of fossil fuels contributes to global climate change as the International Energy Agency predicted that 31.6 gigatonnes was released to the atmosphere due to combustion of fossil fuels in 2011, and 32.6 gigatonnes of CO₂ emission would yield to 2°C increase in the global average temperature [1]. Since this contribution is significant, there is a global effort to reduce the CO₂ emissions, sequester or reutilize CO₂ as a carbon source. However, CO₂ is a fairly stable molecule and requires temperatures on the order of 8600 K at 1 atm for its complete dissociation [2]. Renewable energy sources can be used as alternatives to supplement and ultimately replace the use of fossil fuels. However, these sources generate electricity which requires storage for (i) powering transportation vehicles, (ii) mitigating the temporal mismatch of electricity demand and production rates, and (iii) dealing with the absence of electricity transmission lines through locations with abundant renewable energy resources. Storage of electricity can be done through batteries, ultra capacitors, or renewable fuels. Among these options, chemical storage through generation of renewable fuels have a number of advantages including (i) large energy density to weight ratio, (ii) extremely long energy storage durations, and (iii) not requiring expensive and scarce materials. Hydrogen is preferable based on its energy potential as shown in Figure 1.1, but storage and transportation of hydrogen require high pressures, liquefaction or use of pipelines. These

are all costly solutions and have some problems. Alternatively, the renewable energy can be used to produce more complex synthetic fuels, commonly in two steps as shown in Figure 1.2: gas dissociation process to generate synthesis gas (syngas), followed by a synthesis process to produce the fuel. This study focuses on the dissociation part for syngas production.

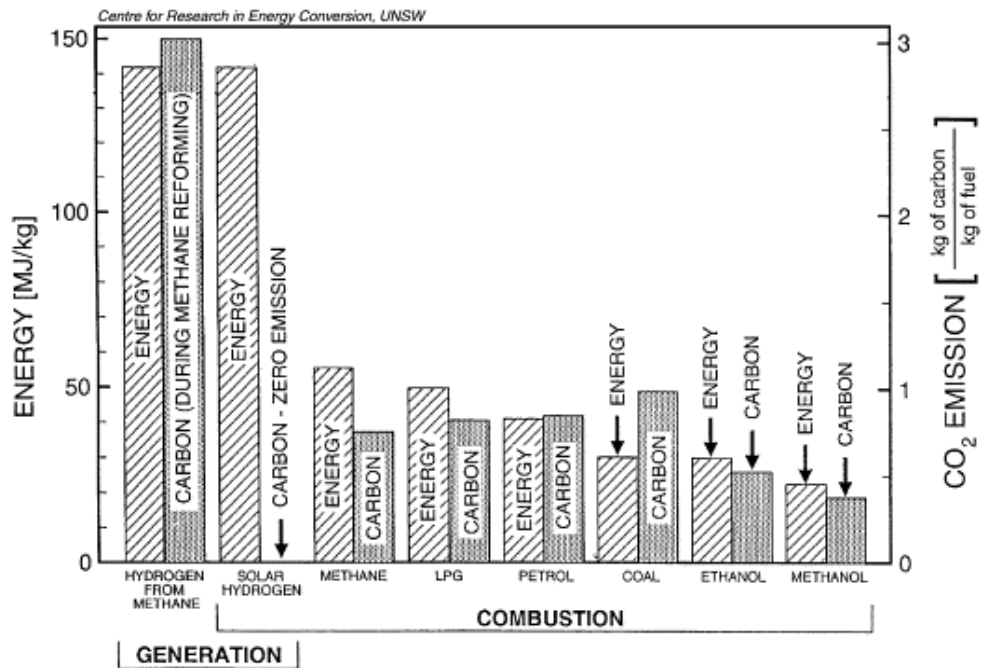


Figure 1.1. Comparison of different fuels in terms of their energy produced and CO₂ emission [3].

Most common and available methods for dissociation are thermolysis, cracking, reforming, gasification and through thermochemical cycles. Although these processes have been considered as promising paths for dissociation gases, they have some disadvantages and technical challenges which form the basis for future research including [4-7]:

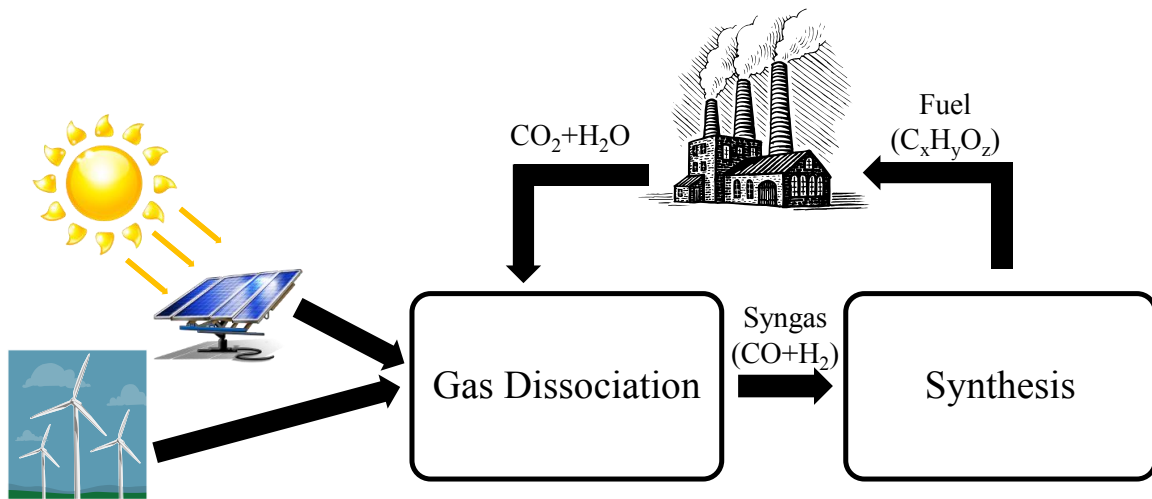


Figure 1.2. Schematic for the synthetic fuel production and carbon and hydrogen cycles for carbon neutral fuel generation and use.

- High temperatures needed for dissociation processes. High temperatures can be reached using solar concentrators with high concentrating ratios. However, high concentrating ratios bring high cost to the system, and high temperatures restrict the material choice.
- Recombination of product gases, especially in thermochemical cycles, is a significant problem. This recombination significantly decreases both the process and energy conversion efficiency.
- Quenching is introduced to products in order to cool the products and reduce the recombination. However, quenching adds additional cost and complexity to the reactor and the process management. For some processes, membranes are also required to separate product gases.
- Particle accumulation at the exit of the reactor is a problem, especially in thermochemical cycles. This problem can be eliminated by introducing an inert gas with high flow rates to the reactor which further complicates the

management of reaction in the reactor. Another solution is to heat the reactor indirectly which reduces the energy conversion efficiency.

An alternative path to dissociate gases and produce syngas is through the use of plasma [8-10]. Specifically, the non-thermal plasma reactors are preferable because they can operate at about room temperatures, so that these reactors do not need to withstand high temperatures. Therefore, the use of non-thermal plasma reactors is expected to reduce the material and manufacturing cost of the reactor. Non-thermal plasma reactors have been used to generate plasma for various applications, including ozone generation [11-13], material synthesis [14, 15], decontamination [16, 17], microdischarge thruster for microsattellites [18-22], and biomedical applications [23, 24]. In particular, gas dissociation and syngas production using non-thermal plasma technologies can offer an alternative to conventional dissociation technologies. To this end, use of non-thermal plasmas can offer distinct advantages including (1) no need for catalysts, (2) lower cost due to simple metallic or carbon based electrodes, (3) lower temperatures involved, and (4) ability to work with a broad range of gases [6, 25-27]. There are different configurations of microdischarge plasma reactors, and in this study the focus was on microhollow cathode discharge (MHCD) plasma reactor which is more suitable for stable plasma generation at atmospheric pressure [28-30]. This reactor can be operated with direct (DC), alternating (AC) and pulsed excitation. However, in order to generate stable non-thermal plasma with DC excitation, the reactor needs to be operated in its self-pulsing regime at which current and voltage of the discharges inherently oscillate [31-33]. In this regime, voltage decreases with increasing current as the regime is characterized with a negative differential resistance [31-33]. A review of microdischarge

plasma reactors were given in detail by Foest *et al.* [34] and Papadakis *et al.* [35], and more information about plasmas and MHCD reactor is given in Chapter 2.

This present study used a non-thermal microhollow cathode discharge reactor for dissociating humidified carbon dioxide for syngas production. Electrical characterization of the introduced reactor was performed using DC voltage in the self-pulsing regime, and the reactor was successfully represented with an equivalent circuit model. Additionally, the dissociation rate of pure and humidified CO₂, power requirement, CO₂-to-CO conversion yield and energy conversion efficiency of a prototype reactor were quantified. The parameters considered in this study included the applied voltage, flow rate of the gases, concentration of CO₂ and H₂O in the reactor influent, as well as the discharge hole size and the thickness of the dielectric material.

1.2 OBJECTIVES OF THE STUDY

The main objective of this study was to demonstrate and quantify the performance of a microhollow cathode discharge reactor for dissociating humidified carbon dioxide stream for producing synthesis gas. More specifically, this study aimed at:

- Characterizing the microhollow cathode discharge reactor in the self-pulsing mode for non-thermal plasma generation, and represent the reactor with an equivalent circuit model for understanding the operating scheme of the reactor
- Quantifying and optimizing the performance of microhollow cathode discharge reactor for syngas production under following operating conditions and design parameters;
 - Applied voltage
 - Flow rate at the reactor influent

- Gas mole fraction at the reactor influent, balanced with an inert carrier gas
 - Dielectric layer thickness
 - Discharge hole diameter
- Assessing the effects of these parameters on the performance of the reactor in terms of the following metrics;
 - Gas concentrations at the reactor effluent
 - Conversion yields
 - Electrical-to-chemical energy conversion efficiency
- Finally, providing guidelines for improving the performance of the microdischarge reactor in future studies.

1.3 ORGANIZATION OF THE DISSERTATION

Chapter 2 provides the background information on the conventional dissociation processes, plasmas and the dissociation processes using plasma reactors. Chapter 3 presents the design of the plasma reactor used in this study, the experimental setup and performance metrics used in this study to quantify the performance of this reactor. Chapter 4 presents the electrical characterization of the reactor along with a semi-empirical equivalent circuit model that captures its voltage and current behavior under different operating conditions. Chapter 5 presents the performance of the plasma reactor on carbon dioxide dissociation under different applied voltages, flow rates and inlet concentration of the gas in terms of electrical-to-chemical energy conversion efficiency and conversion yield. Chapter 6 presents the same performance metrics for dissociation of water-saturated carbon dioxide and argon and discusses the performance of the reactor for carbon monoxide and hydrogen production. Chapter 7 investigates the effects of the

design parameters of the reactor, namely the dielectric thickness and the discharge hole size, on carbon dioxide dissociation. Finally, Chapter 8 summarizes the main findings of this study and presents recommendations for future research.

Chapter 2 Current State of Knowledge

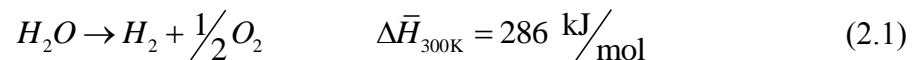
This chapter presents the current state of knowledge on different dissociation processes that have been used conventionally, as well as some important background information about the plasmas and their characteristics. In Section 2.3, a number of dissociation processes using plasma technologies reported in the literature are given. In the final part of this chapter, Section 2.4, the state-of-the-art syngas production methods are summarized for simultaneous production of carbon monoxide and hydrogen from carbon dioxide and water.

2.1 CONVENTIONAL DISSOCIATION METHODS

The different methods of dissociation presented in this section are revised from previously published book chapter by Taylan and Berberoglu [36]. The focus of this section is hydrogen production as an alternative fuel; however, it is also possible to dissociate carbon dioxide into carbon monoxide if water is replaced by carbon dioxide in the corresponding chemical reactions.

2.1.1 Thermolysis

The term “thermolysis” refers to the thermal decomposition of water molecules into hydrogen and oxygen gases. Historically, due to high availability and simple molecular form of water, researches on solar fuel production started with direct hydrogen production by thermolysis of water as,

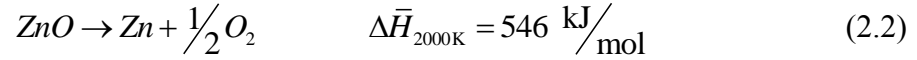


The reaction given in Equation (2.1) is an endothermic process, i.e., it requires energy to break the bonds. However, breaking all the bonds in water molecules requires temperatures as high as 2500 K [37]. At lower temperatures, partial decomposition occurs. Although it is possible to reach 2500 K with concentrated solar energy, the reactor where this process takes place shows material issues related to high temperatures. Additionally, after the dissociation of water molecules, hydrogen and oxygen gases require separation at high temperatures in order to prevent back-bonding, i.e., reproduction of water molecules with an exothermic process. Some solutions include cooling the reactor down by injecting a gas or expanding these gases through nozzle at the end of the reactor [37, 38]. Other solutions include using double or tubular membranes or using multi-stage steam ejectors to lower the exit pressure [39]. However, these solutions further reduce the efficiency of the process, and thus no commercial plant using this technology exists.

2.1.2 Thermochemical Cycles

The thermochemical cycles consist of at least two steps or reaction, reduction of a metal oxide and oxidation of gases. Some metal oxides are reduced in thermochemical cycles since metals provide good storage and transport of energy, such as solar energy. Such metal oxides include, but not limited to ZnO, MgO, SnO₂, CaO, Al₂O₃ and Ce₂O₃. The reduction step of these metal oxides is generally followed by an oxidation step at lower temperatures than reduction step in order to convert or dissociate gases. The reduced metal oxides generally react with CO₂ or steam. If steam is used in oxidation that step is called hydrolysis. The thermochemical cycles of different metal oxides are generally compared based on their temperature requirements for the reduction step, the reaction or dissociation rates and reaction kinetics.

ZnO is one of the most popular oxides mainly due to its abundance and relatively low temperature requirement for complete dissociation when compared to other metal oxides. Additionally, since ZnO is a simple metal oxide, it does not undergo multiple reactions before its full dissociation. The dissociation of ZnO occurs as according to,



The complete dissociation of ZnO to Zn requires temperatures higher than about 2300 K whereas, for instance, the dissociation of MgO as another simple metal oxide requires about 3700 K at atmospheric pressures [38, 40]. As in water thermolysis, partial dissociations can occur at lower temperatures. Although hydrolysis of zinc is exothermic as given by Equation (2.3), only 24% of Zn could be oxidized to produce H₂ at a reactor temperature of 800 K and an atmospheric pressure [41].



Figure 2.1 shows the overall process of hydrogen production from zinc-oxide.

As an alternative to ZnO reduction, Abanades *et al.* [42] proposed SnO₂ reduction. Once the SnO₂ is reduced to SnO in gaseous form at temperatures nearly 1600°C, hydrolysis of SnO with steam at about 550°C and ambient pressure takes place in another step to form hydrogen gas as,



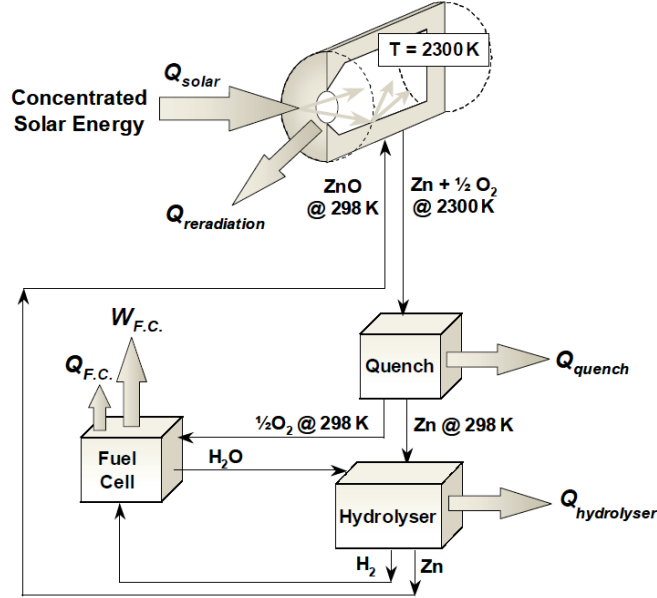


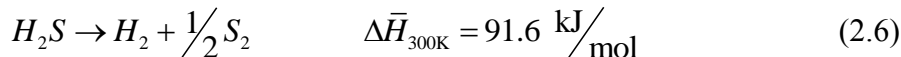
Figure 2.1. Flowchart for thermochemical hydrogen production from zinc-oxide using concentrated solar energy [40].

The advantages of SnO_2/SnO reduction when compared to ZnO/Zn reduction are that (i) the SnO_2 -to- SnO conversion yield can be increased in Equation (2.4) by decreasing the pressure of the reactor which increases the overall conversion efficiency [42], (ii) SnO has higher melting and boiling points when compared to those of Zn , so that quenching rate of SnO is not as important as of Zn [42]. In ZnO/Zn dissociation, Zn needs to be quenched rapidly below its condensation temperature to prevent recombination, while this is not the case with SnO_2/SnO system.

There are some other metals that can be reduced with faster reaction kinetics such as Ce_2O_3 . However, the reduction of Ce_2O_3 to CeO_2 starts at temperatures about 2300 K [43, 44]. Full dissociation requires higher temperatures. This requirement of high temperatures creates some material limitations on the material of the reactor and increases the cost of the reactor significantly. Although there are some lab-scale

prototypes of Ce_2O_3/CeO_2 reactor, it is not preferred due to these limitations and high cost.

Another research was also started with producing hydrogen gas from hydrogen sulfide, H_2S , as,



Hydrogen sulfide is a toxic by-product gas of sulfur removing process from natural gas, petroleum and coal. Thermal decomposition of hydrogen sulfide requires about 1800 K [45]. It is advantageous over the other metal oxide reduction processes discussed above since this thermochemical process is only a one-step process that does not require additional oxidation step to produce hydrogen. Additionally, the temperature requirement for dissociation is lower than that for the direct water thermolysis. However, the product gases need to be cooled down after the dissociation as in the water thermolysis or other metal oxide reduction processes [46]. Some studies showed that the temperature of reduction could be reduced to about 1500 K, and they showed that the recombination of products into hydrogen sulfide is insignificant below 1500 K [38, 47, 48].

In general, the chemical processes are clean ways to produce hydrogen or syngas without any carbon prints. Therefore, the hydrogen as a product of the chemical process can be used in fuel cells directly, or syngas can be directly synthesized in a Fischer-Tropsch process. The chemical reduction steps of these chemical processes produce nanoparticles with high surface area to volume ratio, e.g., Zn, SnO which also create additional reaction centers for the dissociation to occur [42]. Therefore, the oxidation or gas dissociation occurs fast due to high mass transport of gases in the solid phase [42]. As

in the other dissociation processes, the products of the dissociation also need to be cooled in order to prevent recombination of products into reactants. Sandia National Laboratories of US released a comprehensive report on the thermochemical cycle selection with initial selection for further research [49], and Table 2.1 summarizes the studied thermochemical cycles [50].

Table 2.1. Summary of thermochemical cycles [50].

Cycle	Reaction Steps
<i>High Temperature Cycles</i>	
Zinc oxide	$\text{ZnO} \xrightarrow{1600-1800^\circ\text{C}} \text{Zn} + \frac{1}{2}\text{O}_2$ $\text{ZnO} + \text{H}_2\text{O} \xrightarrow{400^\circ\text{C}} \text{ZnO} + \text{H}_2$
Iron oxide	$\text{Fe}_3\text{O}_4 \xrightarrow{2000-2300^\circ\text{C}} 3\text{FeO} + \frac{1}{2}\text{O}_2$ $3\text{FeO} + \text{H}_2\text{O} \xrightarrow{400^\circ\text{C}} \text{Fe}_3\text{O}_4 + \text{H}_2$
Cadmium carbonate	$\text{CdO} \xrightarrow{1450-1500^\circ\text{C}} \text{Cd} + \frac{1}{2}\text{O}_2$ $\text{Cd} + \text{H}_2\text{O} + \text{CO}_2 \xrightarrow{350^\circ\text{C}} \text{CdCO}_3 + \text{H}_2$ $\text{CdCO}_3 \xrightarrow{500^\circ\text{C}} \text{CO}_2 + \text{CdO}$
Hybrid cadmium	$\text{CdO} \xrightarrow{1450-1500^\circ\text{C}} \text{Cd} + \frac{1}{2}\text{O}_2$ $\text{Cd} + 2\text{H}_2\text{O} \xrightarrow{25^\circ\text{C, electrochemical}} \text{Cd}(\text{OH})_2 + \text{H}_2$ $\text{Cd}(\text{OH})_2 \xrightarrow{375^\circ\text{C}} \text{CdO} + \text{H}_2\text{O}$
Sodium manganese	$\text{Mn}_2\text{O}_3 \xrightarrow{1400-1600^\circ\text{C}} 2\text{MnO} + \frac{1}{2}\text{O}_2$ $2\text{MnO} + 2\text{NaOH} \xrightarrow{627^\circ\text{C}} 2\text{NaMnO}_2 + \text{H}_2$ $2\text{NaMnO}_2 + \text{H}_2\text{O} \xrightarrow{25^\circ\text{C}} \text{Mn}_2\text{O}_3 + 2\text{NaOH}$

Table 2.1 continued.

Cycle	Reaction Steps
<i>M</i> -Ferrite (<i>M</i> = Co, Ni, Zn)	$Fe_{3-x}M_xO_4 \xrightarrow{1200-1400^\circ C} Fe_{3-x}M_xO_{4-y} + \frac{y}{2} O_2$ $Fe_{3-x}M_xO_{4-y} + yH_2O \xrightarrow{1000-1200^\circ C} Fe_{3-x}M_xO_4 + yH_2$
Low Temperature Cycles	
Sulfur-Iodine	$H_2SO_4 \xrightarrow{850^\circ C} SO_2 + H_2O + \frac{1}{2} O_2$ $I_2 + SO_2 + 2H_2O \xrightarrow{100^\circ C} 2HI + H_2SO_4$ $2HI \xrightarrow{300^\circ C} I_2 + H_2$
Hybrid sulfur	$H_2SO_4 \xrightarrow{850^\circ C} SO_2 + H_2O + \frac{1}{2} O_2$ $SO_2 + 2H_2O \xrightarrow{77^\circ C, \text{electrochemical}} H_2SO_4 + H_2$
Hybrid copper chloride	$Cu_2OCl_2 \xrightarrow{550^\circ C} 2CuCl + \frac{1}{2} O_2$ $2Cu + 2HCl \xrightarrow{425^\circ C} H_2 + 2CuCl$ $4CuCl \xrightarrow{25^\circ C, \text{electrochemical}} 2Cu + 2CuCl_2$ $2CuCl_2 + H_2O \xrightarrow{325^\circ C} Cu_2OCl_2 + 2HCl$

2.1.3 Cracking of Gaseous Hydrocarbons

The term “thermal cracking” or “cracking” is used for thermal decarbonization of natural gas or other hydrocarbons. As a result of cracking, hydrogen, carbon and other possible products are formed without CO₂ emissions. Therefore, this process is another method for clean fuel production. Cracking requires high temperatures of about 1500 K [51] that can be reached using concentrating solar collectors. For example, Maag *et al.* [52] tested a concentrated solar collector with a concentrating factor of 1720, and obtained a maximum temperature of 1600 K within the solar cavity reactor. In general, the advantages of solar cracking are the increase in value of feedstock using solar energy, pure and uncontaminated products and no CO₂ emission [51].

As being the simplest hydrocarbon and the main constituent of natural gas as given in Table 2.2, methane has been mainly considered for cracking. Chemical reaction of evolution of carbon black and methane is given in Equation (2.7) [53, 54]. The kinetic mechanism of methane cracking at 1500 K and atmospheric pressure was proposed as [55, 56],

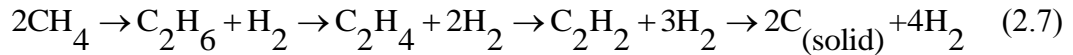


Table 2.2. Compositions of natural gas from different sources [55].

	Volume Fractions (%)					
	CH ₄	C ₂ H ₆	C ₃ H ₈	C ₄ H ₁₀	CO ₂	N ₂
Modified Algeria Gas	91.2	6.5	2.1	0.2	-	-
Modified Groningen Gas	83.5	4.7	0.7	0.2	-	10.8
North Sea Gas	88.2	5.4	1.2	0.4	1.4	3.2

Another important aspect of producing hydrogen and carbon black (solid carbon) is their market values. Hydrogen and carbon black have a market value of about \$135 billion per year and between \$7 and \$11 billion per year depending on the grade of the carbon black in the world, respectively [57].

Under an EU project named SOLHYCARB, a 50-kW_{th} indirectly heated, cavity type solar reactor was developed for methane cracking [43]. Its 10-kW_{th} prototype was built and tested using natural gas, and 97% conversion was obtained with a maximum temperature above 2000 K under concentrated solar irradiation of 4 MW/m² [58]. The difficulties that prevent this technology to become commercial are mainly the cost of the reactor and the complicated flow pattern inside the reactors. For example, in order to

prevent particle accumulation on the window, some inert gas is introduced to the reactor with high flow rates and pressures, or indirectly heated solar reactors are used which decreases the solar-to-fuel conversion efficiency or further increase the cost.

Summary of the operating conditions of a number of designs for methane cracking is given in Table 2.3.

Table 2.3. Operating conditions of different reactor designs for methane cracking.

Reference	Maximum Temperature (°C)	Inlet CH ₄ Dilution (%vol.)	Reactor Dimensions (mm)	Aperture Diameter (mm)	Inlet Flow Rate (l/min)	Catalytic or Particle Fed
<i>Directly Irradiated Solar Reactors</i>						
Maag <i>et al.</i> [52]	1327	6-30 (in Argon)	100 (diameter) 200 (length)	60	8.6-15.6	Carbon black seeded
Yeheskela and Epstein [59]	1450	98 (in catalysts)	200 (diameter) 300 (length)	200	5-9.7	Flow with Fe(CO) ₅ , Fe(C ₅ H ₅) ₂
Abanades and Flamant [60, 61]	1110	11-20 (in Argon)	10 (diameter) 65 (length)	10	0.9	No particle feeding
Klein <i>et al.</i> [62]	1471	10-24 (in Argon or CO ₂)	160 (diameter) 266 (length)	60	37-60	Carbon black seeded
<i>Indirectly Heated Solar Reactors</i>						
Rodat <i>et al.</i> [63]	1800	10-20 (in Argon)	18 (tube diameter) 200 (cube side)	90	-	No particle feeding
German Aerospace Center [47]	1400	5 (in Argon)	-	-	3.8	Reactor walls with Rh
Maag <i>et al.</i> [64]	1600	10-20 (in Argon)	24 (tube diameter) 200 (cube side)	9	10-48	No particle feeding

2.1.4 Gasification and Reforming of Coal and Biomass

Gasification is a chemical process that converts carbonaceous feedstock into gaseous fuels under a controlled amount of oxygen and/or steam [65]. Main difference between gasification and combustion is that products in gasification have useful heating value. In gasification, pressure inside the gasifier is generally in the range from 20 to 40 bar, whereas methanol or ammonia synthesis requires 50 to 200 bar [66]. In addition, temperatures inside the gasifier is generally in the range from 1400 to 1700°C [66].

Dissociation of coal and biomass can be made in steps. Pyrolysis is a thermochemical process that occurs before gasification, and it decomposes the complex hydrocarbons into smaller and less complex molecules in the absence of oxidizers. In pyrolysis, the yield of char can be maximized by slowing the heating rate, lowering the temperature or allowing a longer residence time [67]. On the contrary, a higher heating rate and a higher temperature maximize the gas yield. Additionally, liquid yield at an intermediate temperature can be maximized by increasing the heating rate or minimizing the residence. Tar is an undesired by-product of gasification and pyrolysis. It can cause condensation and consequent plugging, formation of aerosols and polymerization into more complex structures [67].

Gasification is an endothermic process and requires energy to occur. In case of conventional gasification, this energy is supplied from the partial combustion or gasification of feedstock which emits CO₂ to the atmosphere. Use of concentrated solar energy eliminates or reduces the CO₂ emission and utilizes the clean high-temperature gasification process. Additionally, fuel value of the feedstock is increased with solar gasification. For example, fuel value of coal can be increased by about 45% using solar

coal gasification [68], and CO₂ emission can be reduced by about 30% when compared to conventional coal gasification [69].

Gasification of coal and other carbonaceous products is the process of converting these feedstock materials into syngas as well as unreacted CO₂ and water vapor [70]. The gasification products can be further processed. For example, syngas can be processed to form methanol or ammonia or used in cement production, and lean gas can be combusted for heating or used in power stations to generate electricity [51, 71]. Gasification can be performed using CO₂ or steam. In general, steam gasification of coal can be written as,



This process is endothermic and requires temperatures above 1000°C. Similar to coal and other carbonaceous feedstock, biomass can also be gasified in reactors. Conventionally, gasification of biomass has been done using the exhaust gas of combustion of fossil fuels or biomass itself. Biomass includes demol wood, wood chips, sewage sludge, almond shells, straw, etc. If biomass is used, nearly 30% of the initial biomass has to be combusted with oxygen to drive the gasification process due to the temperature requirement [50]. This temperature requirement varies from 600 to 1000°C [72]. Additionally, one of the other disadvantages of conventional biomass gasification is the formation of tar which blocks and clogs the equipment. There have been some efforts to eliminate the tar formation with proper selection of materials, operating conditions and the design of the gasifier [72].

Solar-assisted gasification of biomass has advantages over the conventional process. The main advantages are the elimination of tar formation, even at temperatures as high as 1200°C, and high and rapid conversion of biomass to syngas. At the National

Renewable Energy Laboratory (NREL) in USA, bluegrass was gasified with a maximum conversion of 95% and about 5% of the products were hydrocarbons, ash and char [73]. The resident times can be less than 5 seconds [73]. There is also a solar reactor design to combine solar biomass gasification and steam reformation [73].

The previous studies showed the operating conditions and limitations of the conventional dissociation methods, such as high temperature and catalysts requirements. This study aims to address their issues and propose a simple and efficient plasma reactor for syngas production that can be further processed to produce synthetic fuels.

2.2 INTRODUCTION TO PLASMAS

Plasma is as a cloud of charged particles, often referred as “ionized gas” that respond strongly to electromagnetic field. Plasmas have free charge carriers, so that they are electrically conductive, and as bulk, plasmas are assumed to be electrically neutral. The three parameters that characterize the plasmas are (1) their particle density, (2) temperature of their particles, given in eV where 1 eV corresponds to 11,605 K, and (3) their steady state magnetic field [74]. Figure 2.2 shows the classification of plasmas in terms of their characteristic electron temperatures and number densities.

In terms of particle densities, plasmas can be categorized into three types according to Bellan [74]: (1) non-fusion terrestrial, (2) fusion terrestrial, and (3) space. Non-fusion terrestrial plasmas have particle densities in the range from 10^{14} to 10^{22} m^{-3} , and the particles in these plasmas are weakly ionized. These plasmas feature temperatures of a few eV, and they do not impose or self-produce magnetic field. Magnetic confinement devices produce fusion terrestrial plasmas which have particle densities in the range from 10^{19} to 10^{21} m^{-3} , and the particles in these plasmas are fully ionized. These

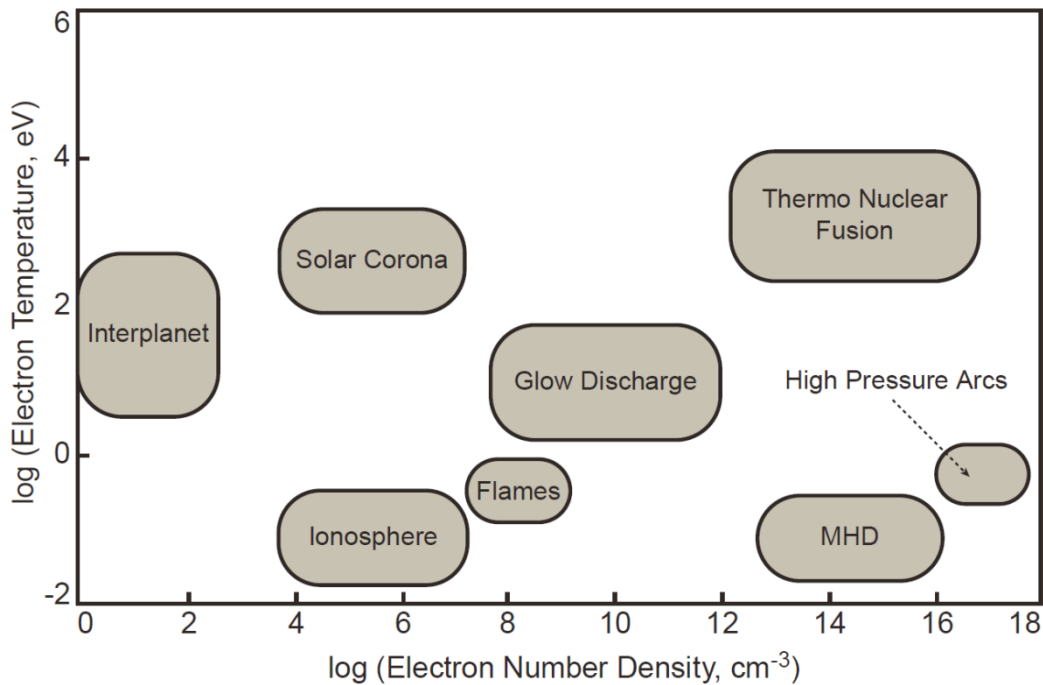


Figure 2.2. Classification of plasmas in terms of electron temperatures and number densities [25, 75].

plasmas have temperatures from tens to tens of thousands of eV, and produce magnetic fields from 1 to 10 Tesla. Extra-terrestrial or space plasmas have a particle density from 10^6 to 10^{20} m^{-3} , and feature temperatures from 1 to 100 eV. The particles in these plasmas are fully ionized.

Plasmas are used in (1) abating low VOC emissions, (2) coating industry, (3) arc welding, and (4) surface modification as printing, painting, metallization, etc. Additionally, plasmas can be used in dissociating gases due to their (1) compact and low weight reactor, (2) high conversion yield, (3) low manufacturing cost due to simple metallic or carbon electrodes, (4) fast response time, (5) ability to work with a broad range of gases, (6) low power requirement, and (7) no need for catalysts [6].

Plasmas can be also categorized in terms of the electron temperatures, such as thermal and non-thermal plasmas. In thermal plasmas, electron and heavy particle (neutrons, protons, etc.) temperatures are the same. On the other hand, non-thermal or cold plasma refers to a plasma state that is not in thermal equilibrium, where electron temperatures are in the range from 10,000 to 100,000 K, and heavy particle temperatures are in the range from the room temperature to 1000 K [76]. The equilibrium is not attained as the electron number density is not high enough when compared to other heavy particles to achieve sufficient energy transfer between the electrons and the heavy particles [76]. Therefore, the temperature of the electrons increases whereas the temperature of the heavy particle can remain at or near the ambient temperature.

Non-thermal plasmas can be further categorized according to their generation mechanism as [26]. The mechanisms include, but not limited to the following types,

- Glow discharge: Glow discharges are commonly used in fluorescent lightings. Two electrodes are placed in a dielectric tube at pressures of a few Torr. The gap between electrodes at low pressure poses a high resistance that prevents high current to flow and form a glow discharge.
- Corona discharge: Corona discharge occurs when electric field near one of the electrodes is significantly higher or lower than the rest of the system.
- Dielectric barrier discharge or silent discharge: Dielectric barrier discharge reactors (DBD) use two parallel-plate metal electrodes, separated by a few millimeters. One of the electrodes is covered by a dielectric layer. Plasma is generated within the gap between the electrodes. A historical perspective, applications and physics of DBD plasmas were given in detail by Kogelschatz [77].

- Microwave discharge: Microwave induced plasmas have no electrodes, and require frequencies higher than about 1 GHz. In cold microwave plasmas, as the frequency of the electrons in the plasma is increased, the electrons start to follow the oscillations of the electric field whereas the heavy particles follow the average temporal local values of the magnitude of electric field.
- Radio frequency discharge: The mechanism is similar to microwave discharges, except radio frequency discharges require frequencies on the order of 1 to 100 MHz.

Mechanism of non-thermal plasma formation were given by Moreau [78] and Forte *et al.* [79] in detail. In all these mechanisms, if the gap between the electrodes is less than a millimeter, the plasma is referred as “microplasma” or “microdischarge.” Microplasmas and applications are reviewed by Becker *et al.* [80]. This review paper summarized the electrode geometries, materials and fabrication methods, electron and gas temperatures in the reactors. The authors also mentioned the applications of microplasma reactors and modeling studies. In this study, the focus is given in glow discharges with direct current (DC) excitation in microplasmas, and further detail is given in the next subsections.

2.2.1 Different Operating Regimes of Plasma

Figure 2.3 shows the voltage and current characteristics of discharges [25, 75]. The region AB in this figure shows the abnormal regime in which a small increase in current results with significant increase in voltage. At low currents, the dark discharge regime occurs which corresponds to region BC in Figure 2.3. In this regime, the current is so low that the electric field is not disturbed and stays uniform. The plasma is confined in

the discharge hole in these low-current regimes. As the current increases, transition from dark to glow discharge occurs. With the increase of current, the number density of positive space charges becomes higher near the cathode. Therefore, this layer of positive space charges causes the electric field between the electrodes to be disturbed. The current density and electric field increase near cathode, and they both decrease near anode. This redistribution of electric field yields to lower voltages in glow discharge than that in the dark discharge. Additionally, a significant voltage drop occurs near cathode due to positive charge accumulation [25, 75]. This transitional regime corresponds to region CD in Figure 2.3. This regime is also referred as the “self-pulsing regime” in DC plasmas. This study focuses on this self-pulsing regime with DC excitation to generate non-thermal plasmas.

As the current further increases, the normal glow discharge occurs which corresponds to region DE in Figure 2.3. The normal glow discharge regime has constant voltage and current density regardless of the current. The normal current density can be obtained if the cathode surface area is large enough to carry the current which is larger than the ones for transition and dark discharges. This mechanism keeps the voltage constant in the normal glow discharge regime. When the current is greater than the current that can be sustained in the normal discharge regime, the discharge covers the entire cathode surface, and current density increases [25, 75]. This regime is called the abnormal glow regime and corresponds to region EF in Figure 2.3. As the current density increases, the thickness of cathode layer and the voltage drop in the cathode layer decrease, whereas the electric field increases. Additionally, due to the increase in current density, gas heating occurs such that transition from abnormal glow to arc discharge

happens in some cases [25, 75]. The regions FG and GH show the transitional regime from glow to arc and arc discharge regime, respectively.

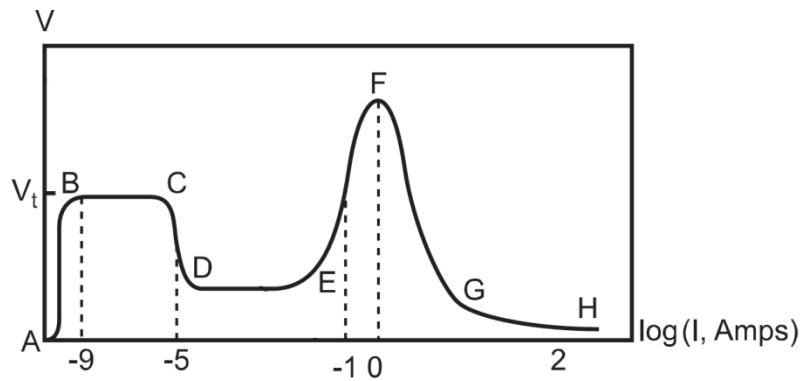


Figure 2.3. Voltage and current characteristics of DC discharges [25, 75].

2.2.2 Electron Avalanche (Townsend Breakdown) Mechanism

The breakdown mechanism considers an electron that is liberated at cathode surface and accelerated due to presence of the electric field between the electrodes. As the electron is drifted towards the anode, it collides with molecules and causes ionization if it has enough energy for ionization. In general, ways of ionization for gas particles can be listed as,

- electron impact with heavy particles
- collisions among heavy particles
- excitation of particles
- photo-ionization of particles
- electron attachment to and detachment from particles

Then, the generated electrons continue to accelerate and move towards the anode under the effect of electric field and create a cascade of ionizations. As the electrons

reach the anode, breakdown occurs, medium between the electrodes neutralize, and another avalanche starts forming if the discharges are stable and continuous. Figure 2.4 illustrates the breakdown mechanism and cascade of ionizations due to electron avalanche.

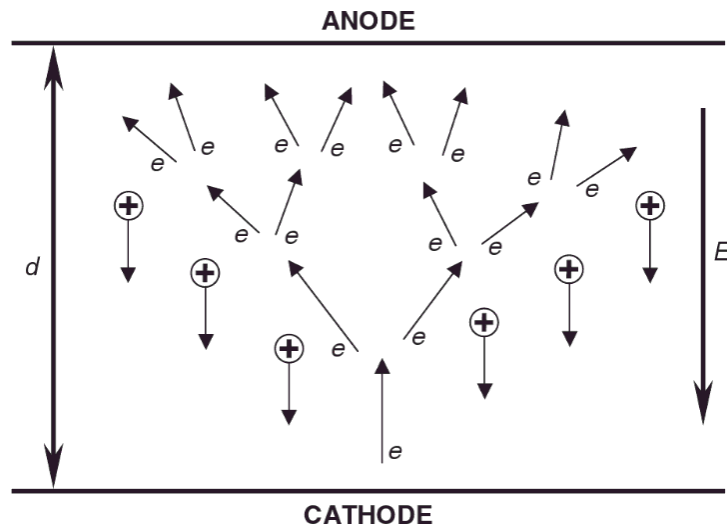


Figure 2.4. Schematic illustrating the Townsend breakdown mechanism and electron avalanche [81].

In order to mathematically analyze the cascade of ionizations, the Townsend ionization coefficient, α , is used rather than the ionization rate coefficient which is for a single ionization process. Each electron generated near cathode leaves $[\exp(\alpha d) - 1]$ positive ions which eliminate $\gamma[\exp(\alpha d) - 1]$ electrons from the plasma phase where γ is the secondary emission coefficient and d is the distance between the electrodes. Secondary ionization coefficient shows the probability of electron generation on the cathode surface by positive ion impact on the cathode. This coefficient depends on the cathode material, surface condition, the medium (gas) and reduced electric field (E/p).

Additionally, the Townsend breakdown analysis does not consider electron losses due to recombination and attachment to electronegative molecules. Based on the current due to primary electrons, I_o , the current considering the secondary emissions becomes,

$$I = \frac{I_o \exp(\alpha d)}{1 - \gamma [\exp(\alpha d) - 1]} \quad (2.9)$$

At the instant of breakdown, the current tends to go to infinity which requires the nominator goes to zero. Therefore, for self-sustained breakdown, the following condition is necessary,

$$\gamma [\exp(\alpha d) - 1] = 1 \quad (2.10)$$

Therefore, if this condition is met, the current flows continuously between the electrodes. In some cases, such as in the self-pulsing regime, it requires some time to accumulate the charges in the discharge gap, i.e., between the electrodes, to meet this condition. Although the current is not continuous in this regime, the discharges are self-sustained at a particular frequency.

2.2.3 Paschen Curve

When a gas is subjected to electric fields larger than its breakdown threshold, it can be ionized and form plasma between the electrodes. During this process, electrons of the gas molecules receive energy from electric field due to their high mobility and low weights compared to those of heavy particles. Due to high surface-to-volume ratio, the electron number densities in microdischarge plasma are on the order of 10^{12} - 10^{16} cm^{-3} which is on the same order for thermo nuclear fusion [75]. Electric field is reduced in the discharge gap as the charges accumulate near the electrodes caused by electrode

polarization. After a short duration on the order of 10 ns, the current is terminated [25]. The plasma in the gap can remain non-thermal because of this short duration of discharges. Therefore, heating of the reactor and the gas in the discharge gap is avoided. In a non-thermal plasma, also known as non-equilibrium plasma, the temperature of the electrons is significantly higher than that of heavy particles, often exceeding 10,000 K [75], whereas the effective temperature of the gas being at about room temperature. The plasma phase is maintained for continuous operation by successive discharges which occur at locations other than the preceding discharge locations due to residual charges [25]. However, if the electric field is applied for a long period of time or higher electric field is applied, non-thermal plasma can reach thermal equilibrium and thermal plasma can be generated.

The breakdown voltage, V_{br} , which is the minimum required value for plasma generation is computed using the approach of Townsend breakdown mechanism for gases [82]. This mechanism assumes uniform electric field and considers independent electron avalanches which occur at electron separation gaps smaller than 50 mm at atmospheric pressure [25]. Additionally, as mentioned in the previous section, the Townsend mechanism does not consider electron losses due to recombination and attachment to electronegative molecules [25]. Using this mechanism, the breakdown voltage, V_{br} , was calculated as [25, 82, 83],

$$V_{br} = \frac{A_2 pd}{A_3 + \ln(pd)} \quad (2.11)$$

where A_2 is a gas-specific constant given in Table 2.4, p is the pressure of the gas in Torr, d is the distance between the electrodes in cm and A_3 is a parameter defined as,

$$A_3 = \ln A_1 - \ln(\alpha d) \quad (2.12)$$

where A_1 is a gas-specific constant given in Table 2.4, and α is the Townsend coefficient defined as,

$$\alpha = pA_1 \exp\left(\frac{A_2}{V_{br}/pd}\right) \quad (2.13)$$

Since V_{br} is a function of A_3 , and A_3 is a function of α which is a function of V_{br} , V_{br} cannot be solved explicitly. For this reason, V_{br} was calculated iteratively using Equations (2.11) through (2.13).

Table 2.4. Parameters for calculation of breakdown voltage [25, 75, 83].

Gas	A_1 (cm ⁻¹ Torr ⁻¹)	A_2 (V cm ⁻¹ Torr ⁻¹)
Air	15	365
Ar	12	180
CO ₂	20	466
H ₂	5	130
H ₂ O	13	290

Figure 2.5 shows the breakdown electric field and voltage for some selected gases as a function of the pressure times the discharge gap, referred as the Paschen curve. In Appendices, Section B.1 shows the numerical code used in this study for Paschen curve calculations.

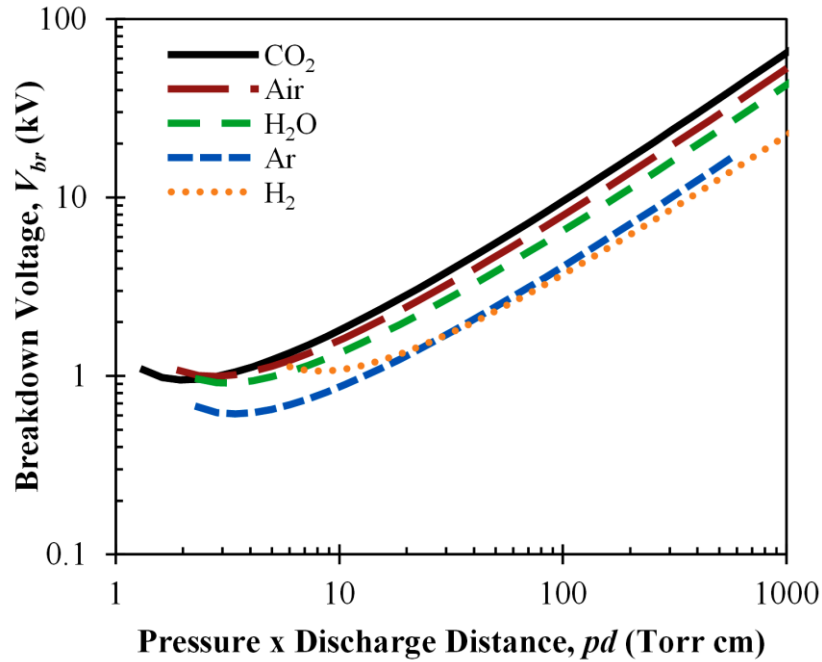


Figure 2.5. Paschen curves for selected gases.

The Paschen curves can be used to estimate the applied voltages to generate plasma. However, these curves are valid for uniform electric fields. Therefore, as the electron avalanches occur, the electric field is disturbed and the Paschen curves fail to estimate the voltage requirement. Additionally, for electrode separations larger than 50 mm at atmospheric pressure, i.e., where Townsend breakdown mechanism cannot be used, Spark mechanism was introduced [25, 75]. This mechanism considers a concept of streamers which are highly ionized, more confined beams of charges between the electrodes.

Moreover, the pd values less than the one that corresponds to the minimum breakdown voltage (referred as the left hand side of Paschen curve) correspond to discharges called obstructed glow discharge. In these discharges, the actual pd is less than required pd for normal current density in the reactor. Therefore, the normal current

density cannot be achieved in the reactor, and electron avalanches cannot continue for self-sustained discharges. This condition causes unstable plasma generation, and thus, it is not preferred.

In order to sustain the discharges, the electrons must be continuously supplied by the cathode, and the work function is defined as the minimum energy required to be supplied to a metal to pull an electrode from the surface. It is the difference between the electrochemical potential (Fermi level) of electrons and the potential of the medium near the electrode. Table 2.5 shows work functions of some metal electrodes for clean surfaces. Work function changes with the condition of the surface, such as its contamination and roughness [84].

Table 2.5. Work function of some metal electrodes [84].

Electrode Material	Work Function (eV)
Barium	2.49
Aluminum	4.25
Molybdenum	4.3
Iron	4.31
Copper	4.4
Nickel	4.5
Tungsten	4.54
Carbon	4.7
Platinum	5.32

The ways to create sustainable discharges can be summarized as follows,

- Photoelectric emission: a photon with enough energy hits the electrode and an electron is emitted from the electrode.

- Thermionic emission: if an electrode is heated enough, it will emit electrons.
- Field emission: when the potential near the electrode surface is small enough that it creates a “potential well,” electrons can tunnel from the electrode to this well.
- Secondary electron emission: when the positive ions hit the electrode surface with enough energy, they both get neutralize and can pull an electrode from the electrode.

2.2.4 Glow Discharge

Glow discharge shows higher degree of ionization than dark discharge and has more effective volume than arc discharges. Therefore, the dissociation studies focus on glow discharges as shown in the next section, Section 2.3. Figure 2.6 shows the general structure of a glow discharge as well as the distribution of some parameters in a tubular reactor. In general, a glow discharge consists of the following regions, in order according to their distances from cathode,

- **Cathode layer:** This region is dominated by positive ions as the electrons are repelled from cathode and drifted under the effect of electric field. This region consists of sub-regions, namely Aston dark space, cathode glow, cathode dark space, negative glow and Faraday dark space. In Aston dark space, the electrons liberated from cathode is accelerated towards anode, but they do not have enough energy to cause excitation. Therefore, no phonon emission is observed and this sub-region seems dark. As they reached the energy to excite the gas particles, cathode glow sub-region forms. As the electrons are further accelerated, they cause ionization rather

than excitation. This cause cathode dark space formation. The high density of electrons significantly causes phonon emission at the end of cathode dark space at which negative glow sub-region starts. Due to collisions in the negative glow sub-region, the electrons lose energy and this cause transition to Faraday dark space.

- **Positive column:** This region occurs if electrodes are separated enough from each other, so that cathode and anode layers do not overlap. As the electron energy reaches enough energy under the electric field, the excitation happens and the excited species start emitting phonons. The plasma in the positive column is independent of the phenomena of cathode and anode layers. The rate of ionization and loss of electrons due to diffusion do not depend on the electron density in the positive column according to Engel-Steenbeck relation [25, 75]. Therefore, the electric field in this region only depends on the gas type, pressure and the diameter of the tube, and the electric current in the positive column is determined by external resistance or the load.
- **Anode layer:** This region is dominated by electrons and negative space charges. Similar to cathode layer, there exists an anode dark space and anode glow sub-region in the anode layer. In this layer, the ionization is about three orders of magnitude smaller than that in the cathode layer [25, 75]. Therefore, the voltage drop in the anode layer is smaller as shown in Figure 2.6c.

In general, the plasma in the glow discharge is quasi-neutral, i.e., the number of electrons and negative ions is equal to number of positive ions in all regions, except the

“sheath” regions. Figure 2.6f and g show that sheath regions occur near the electrodes due to the interaction of electrodes with ions. The electrons move away from the cathode under the effect of applied electric field which decreases the electron density near cathode. This depreciation of electrons induces an opposing electric field and makes the electrons diffuse towards the cathode. Under the effect of electric field, positive ions move towards the cathode. However, the flux of ions towards the cathode is significantly smaller than that of electrons due to their mass differences. These differences in fluxes cause deviation from quasi-neutrality and define the sheath regions. Similar approach can be discussed for the anode.

Instabilities might occur in glow discharges. These instabilities are mainly in terms of discharge contraction due to overheating (thermal) instability and stepwise ionization instability [25, 75, 85]. These instabilities can cause nonlinear electron ionization and it happens if the current or current density exceeds a critical value. As a result, contracted glow discharge filaments occur along the axis of the tube. After contraction, the required energy for ionization decreases due to increase in the number density of excited species. This may yield to thermal plasma after the contraction. The common solution is the cathode segmentation in which each segment of the cathode is externally applied voltage so that the voltage drop due to contraction is no longer significant. Increasing flow rate with more uniform flow is another solution to contraction. Additionally, the transverse and longitudinal instabilities cause striations or grooves. This kind of instabilities is mainly due to localized high or low electron or ion densities. However, these instabilities do not affect the non-thermal nature of glow discharges unlike the discharge contraction.

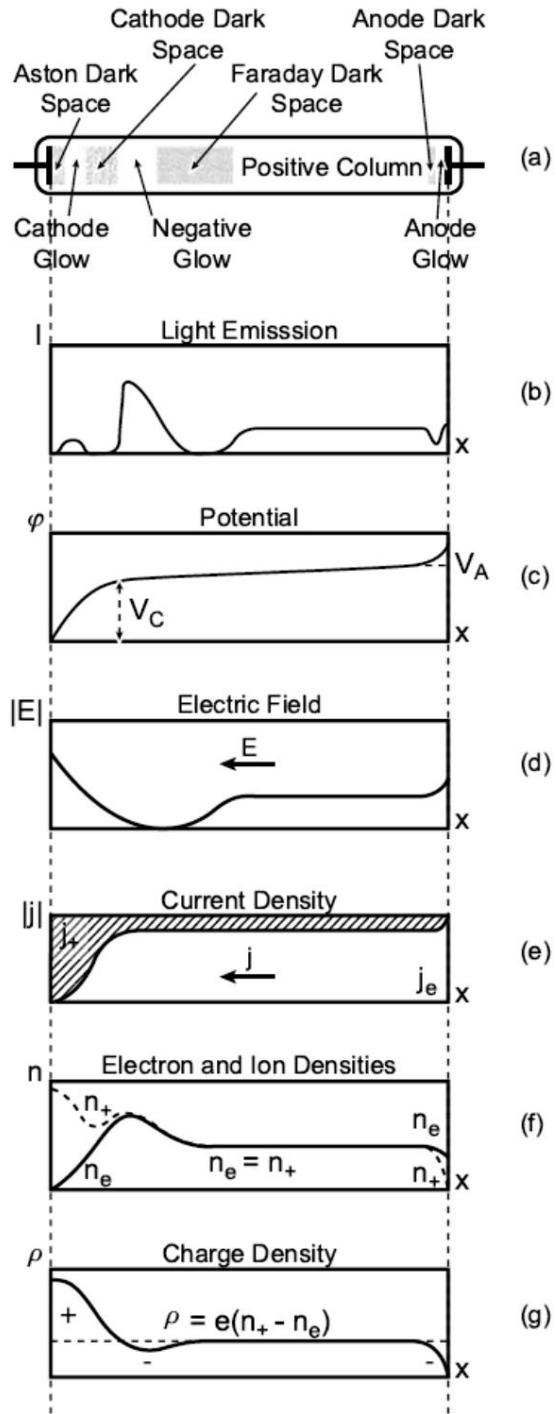


Figure 2.6. The glow discharge regions and the distribution of some key parameters between the electrodes [25, 75].

2.2.5 Hollow Cathode Discharge

Hollow cathode discharge is also used for the geometry of the plasma reactor which consists of a hollow cathode and an anode with arbitrary shape. Figure 2.7 shows a schematic of a simple geometry for hollow cathode discharge reactor. As the distance between the cathodes, D , gets smaller, their negative glow sub-regions become closer or overlap. Electrons liberated from or near one of the cathodes move towards the positive column under the effect of electric field. If these electrons have enough energy, they enter the negative glow sub-region of the cathode on the opposite side, and they feel the presence of the opposing electric field. These opposing electric fields between the cathodes make the electrons move back and forth between the cathodes like pendulums. These electrons are sometimes referred as “pendulum electrodes,” and this mechanism is called “Pendel effect” [80, 86]. Due to Pendel effect, the ionization effect of electrons is significantly increased with respect to other glow discharges. Additionally, in the hollow cathode discharge, secondary electron emission is more pronounced than the glow discharge since the electron number density in the negative glow increases the number of positive ions close to the cathode. Higher photoemission from cathodes augments the ionization as well.

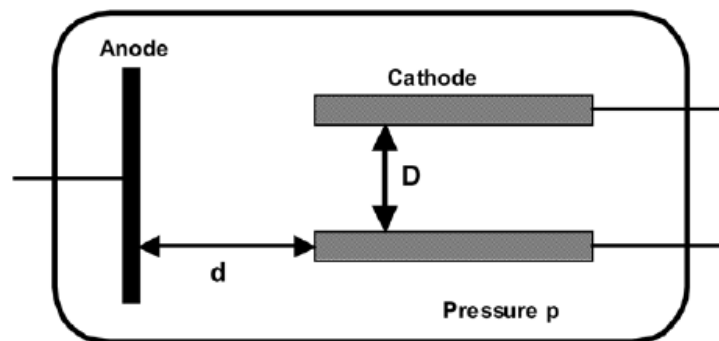


Figure 2.7. Schematic of a hollow cathode discharge [80].

When the distance between the cathodes is less than a millimeter, the hollow cathode discharge is called “microhollow cathode discharge” (MHCD). MHCD reactors follow the general electrical characteristics of glow discharges. However, the term MHCD is ambiguously used in the literature for the transitional regime CD in Figure 2.3 where voltage decreases with increasing current. MHCD reactors can be operated in any regimes with alternating, direct or pulsed excitation. This study proposes a MHCD reactor operating at self-pulsing regime for CO₂ and H₂O dissociation. Additionally, Chapter 4 shows the electrical characterization of the MHCD reactor in this regime.

2.3 PLASMA DISSOCIATION

This section summarizes gas dissociation using different plasma reactors and technologies, including microdischarge plasmas.

2.3.1 Plasma Studies and Plasma Reactor Designs

Subrahmanyam *et al.* [87] designed a novel dielectric barrier discharge (DBD) plasma reactor to oxidize the volatile organic compounds that are toxic and carcinogens and are emitted by various industrial processes. The oxidation of volatile organic compounds requires temperatures about 700-900°C, and plasma reactors can be used as catalysts for this process. With the use of catalysts, the temperature of the oxidation process can be reduced to 300-500°C, but conventional catalysts require high energy supply even at low concentrations. Subrahmanyam *et al.* [87] suggested using a DBD plasma reactor to overcome this limitation of conventional catalysts. They tested their reactor design using toluene at room temperature and pressure. During their experiments, they varied toluene concentration, applied AC voltage and frequency. Figure 2.8 shows the schematic of the reactor. A cylindrical quartz tube with inner diameter of 18.5 mm

and wall thickness of 1.6 mm was used. The tube was covered with silver which was used as an outer electrode. The inner electrode was copper, and AC voltage with peak of 12.5-22.5 kV was applied in the range of 200-450 Hz. Alternatively, inner electrode was replaced with stainless steel sintered Mn or Co metal fibers. Reactor with Co/SMF electrode showed the highest conversion, ~85% at 12.5 kV with 200 Hz. The conversion ratio could reach up to 100% as the voltage was increased to 22.5 kV or the frequency was increased to 450 Hz. Their results also showed that the toluene-to-CO₂/H₂O conversion decreased as the flow rate of toluene increased for each electrode.

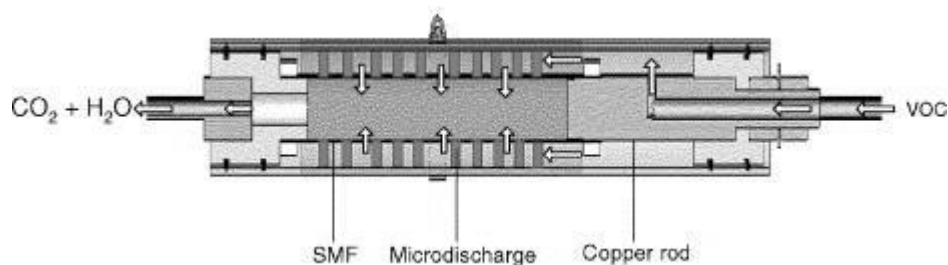


Figure 2.8. Schematic of plasma reactor design of Subrahmanyam *et al.* [87].

Cal and Schleup [88] also considered oxidation of volatile organic compounds, and used dielectric barrier discharge (DBD) plasma reactor for the process. They tested their reactors using benzene at room temperature and pressure. Two planar DBD reactors consisting aluminum electrodes of spacing of 3 mm and 5 mm were designed. As a dielectric medium, Pyrex glass was used. Aluminum electrodes had 18 cm width and 30 cm length. AC voltages and frequencies were varied from 9 to 20 kV and from 45 Hz to 15 kHz, respectively, and the residence times were varied from 5 and 32 seconds. The results of this study showed that increasing applied voltage, increasing residence time, decreasing relative humidity, and decreasing electrode spacing increased the benzene-to-

products conversion. They could achieve conversion yields higher than 99%. Conversion yield is defined as the number of moles of net produced product divided by that of fed reactant. Additionally, increasing relative humidity decreased CO formation. At an applied voltage of 9 kV, frequency of 1 kHz, gap distance of 3 mm and a residence time of 5 seconds, the benzene dissociation decreased from about 47% to 12% when the relative humidity increased from zero to 90%.

Jahanmiri *et al.* [89] investigated the dissociation of naphtha as a heavy hydrocarbon using a nanosecond pulsed dielectric barrier discharge plasma reactor at room temperature and pressure. Figure 2.9 shows the schematic of their experimental setup. The plasma reactor was made of a cylindrical Pyrex glass with an inner diameter of 15 mm and a wall thickness of 2 mm. The cylindrical glass was covered by 10-cm-long aluminum foil as the outer electrode. A copper rod with a diameter of 1.35 mm was used as an inner electrode to test different voltages and frequencies. Copper was selected due to its low electrical resistance. Moreover, they investigated effect of inner electrode material on the conversion efficiency and used copper, iron, brass, aluminum and stainless steel electrodes. Each electrode had a diameter of 6 mm. Voltages up to 7 kV with corresponding applied power from 3 to 24.7 W and frequencies up to 18 kHz were applied to the reactor with pulse duration less than 50 ns. The results of this study showed that better conversion could be obtained with increasing applied voltage or frequency. Conversion yields up to 69% were reported. The temperatures of the inner and outer electrodes at different voltages and frequencies were also reported. The temperature of the inner copper electrode was about 190°C whereas the temperature of the outer aluminum electrode was about 160°C at 7 kV and 18 kHz. Among the investigated five electrodes, the lowest temperatures were observed for steel electrode whereas inner

aluminum electrode had the second lowest temperature. The energy efficiencies of the reactor which was defined as the ratio of the total volume of produced gas to the input power listed as steel, aluminum, brass, iron and copper electrodes in the decreasing order.

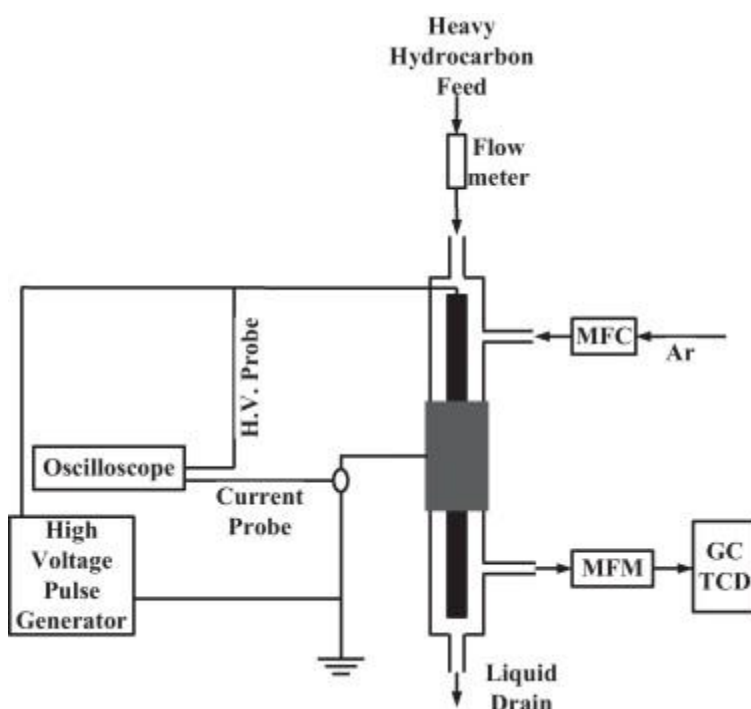


Figure 2.9. Experimental representation of Jahanmiri *et al.* [89].

Studies on conversion of methane to methanol using non-thermal dielectric barriers discharge plasmas were reviewed by Indarto [90]. Three main designs were reported in this paper as given in Figure 2.10. The parameters mentioned in this study were methane-to-oxidizer ratio, residence time, applied voltage, and use of noble gas as a carrier gas. As an oxidizer; oxygen, carbon dioxide and water vapor were considered. It was reported that as the oxygen-to-methane ratio was increased, the methanol formation increased up to oxygen-to-methanol ratio of 4:1 after which the conversion decreased

[91, 92]. Increasing the residence time decreased the methanol formation as the produced methanol was converted into other compounds, such as formic acid, methyl formate on longer residence times [93]. On the other hand, shorter residence time reduced the methane-to-methanol conversion [94]. Required voltage for methanol formation was also a function of the electrode gap, and increasing voltage increased the methanol formation. Okumoto *et al.* [95] stated that increasing the concentration of an inert gas in the plasma reactor could increase the methanol conversion when the concentration of the oxidizer was kept constant as the number of free electrons increased and the partial pressure of methane decreased. When carbon dioxide was used as an oxidizer, more complex products, such as formic acid were also observed in addition to methanol formation. They also stated that use of water vapor as the oxidizer without supplementary oxygen or carbon dioxide could limit the over-oxidation of methanol after its formation.

Mfopara *et al.* [98] studied the effects of water vapor on methane dissociation using dielectric barrier discharge (DBD) plasma reactor under atmospheric pressure and temperatures less than 150°C. The reactor was made of Pyrex glass cylinder with an outer diameter of 25 mm and a wall thickness of 3 mm. The inner and outer electrodes were stainless steel and copper, respectively. The inner electrode was at the center of glass cylinder and had a diameter of 19 mm. The outer electrode covered the glass cylinder from outside. The electrodes had a length of 10 cm. They applied a peak voltage of 10 kV at 7350 Hz, and the maximum power per flow rate was about 1500 J/L. Methane was diluted in nitrogen, and effects of water vapor on methane oxidation were investigated under 0 or 10% per volume oxygen conditions. When water vapor was introduced to the reactor, methane molecules competed with water molecules for active nitrogen

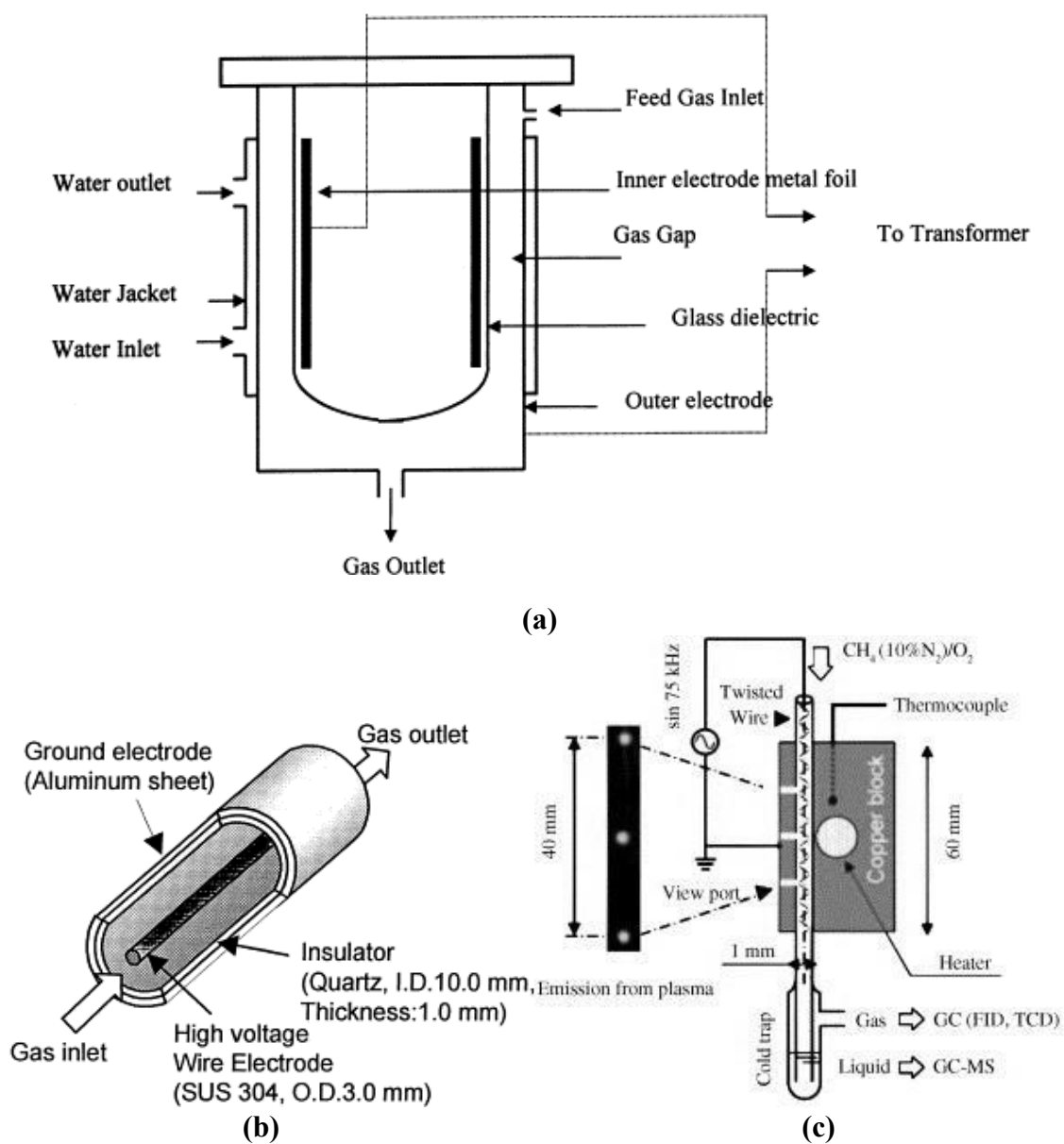


Figure 2.10. Different plasma reactor designs given in Indarto [90]; (a) Larkin *et al.* [93], (b) Okumoto and Mizuno [96], (c) Nozaki *et al.* [97].

molecules, and the conversion yield of methane decreased from about 50% to 35%. Addition of water vapor promoted the carbon monoxide and carbon dioxide formations instead of hydrogen cyanide (HCN) formation which was the case under no oxidant

conditions. In the presence of oxygen, methane conversion was increased and the process yielded towards complete oxidation, i.e., towards carbon monoxide and carbon dioxide formation.

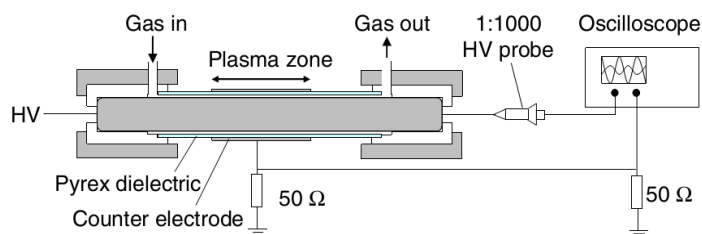


Figure 2.11. Experimental setup of Mfora *et al.* [98].

Jun and Jacobson [99] designed a dielectric barrier discharge (DBD) non-thermal plasma reactor for CO₂ dissociation. The reactor had a 1 mm by 1 mm square plasma channel with two 65-mm-long copper electrodes. Glass with 1 mm thickness was used as a dielectric barrier. CO₂-to-CO conversion was investigated with varying residence time, flow rate of CO₂ and applied voltage. The applied voltage was varied from 5.9 to 6.9 kV at 1.1 kHz, residence time was between 0.3 and 2 seconds. The CO₂ flow rate was varied from 3 to 20 cm³ for DBD reactor. The results showed that as the applied voltage and residence time increased, CO₂-to-CO conversion was increased. As the applied voltage increased from 5.9 to 6.9 kV, CO concentration at the reactor effluent increased by about 8 times at a flow rate of 10 mL/min. Additionally, as the residence time increased from 0.3 to 2 seconds at an applied voltage of 6.9 kV, the CO concentration increased more than 4 times.

Liang *et al.* [100] designed and analyzed a dielectric barrier discharge plasma reactor for H₂S dissociation at room temperature and pressure. The reactor was made of

20-cm-long poly(methyl methacrylate) (PMMA) cylinder with an outer diameter of 32 mm and a wall thickness of 2 mm. Iron was used as an outer electrode, and tungsten wire with 1.25 mm diameter was used as an inner electrode. Air was used as a carrier gas. Similar to the other studies mentioned above, H₂S conversion increased with increasing applied AC voltage and frequency. H₂S conversion yield increased from 6.8 to 7.8% when frequency was increased from 100 to 400 Hz at 10 kV. The conversion yield was defined as the concentration change in H₂S before and after the plasma reactor divided by the initial concentration. The maximum yield of 82.8% was obtained at 21 kV and 400 Hz. These values were obtained when the inlet concentration was 30 ppm, gas flow rate was 0.25 L/s and residence time was 0.8 s. Increasing residence time and specific energy density (J/L) increased the decomposition efficiency. The authors further improved their design by randomly packing the reactor with ceramic Raschig rings or glass pellets. Results showed that pellets increased the H₂S conversion yield were about 93%, 80% and 69% for ceramic Raschig rings, glass pellets and no pellets, respectively, at 21 kV. The major products observed were H₂O, SO₂ and SO₃.

Kappes *et al.* [101] designed a dielectric barrier discharge (DBD) reactor for steam reforming of methane to produce hydrogen. Figure 2.12 shows the design of DBD reactor. The 450-mL reactor was made of alumina ceramic tube with inner diameter of 46 mm and wall thickness of 5 mm. The inner electrode had metal disks with 38 mm in diameter. The outer electrode was deposited outside the alumina ceramic tube. Pulse voltage was applied to the inner electrode with a rise time of 15 V/ns, a frequency of 15 kHz and a peak voltage of 40 kV. Average of 180 W was supplied which corresponded to 3.6 kJ/L. The reactor was heated to around 400°C before the gas fed into the reactor. Methane-to-hydrogen conversion was less than 6%, and the rest of the products were

C_2H_6 , CO, C_2H_4 , C_2H_2 , C_3H_8 , CH_3OH , CO_2 , C_3H_6 , and C_4H_{10} in the decreasing order of volume fractions. The authors stated that only about 3% of the total input power corresponded to the reaction enthalpy rate, whereas about 63% of the total power was used in heating the alumina ceramic tube.

Spencer and Gallimore [102] experimentally studied CO_2 dissociation in a 1-kW RF discharge at the frequency of 13.56 MHz. The CO_2 was fed into a 15-cm diameter and 50-cm long cylindrical quartz tube. The power was varied from 0 to 1 kW, and an external magnetic field was applied from 0 to 60 A. The results showed that external magnetic field increased CO production up to 20% at 1 kW and flow rate of 100 ml/min.

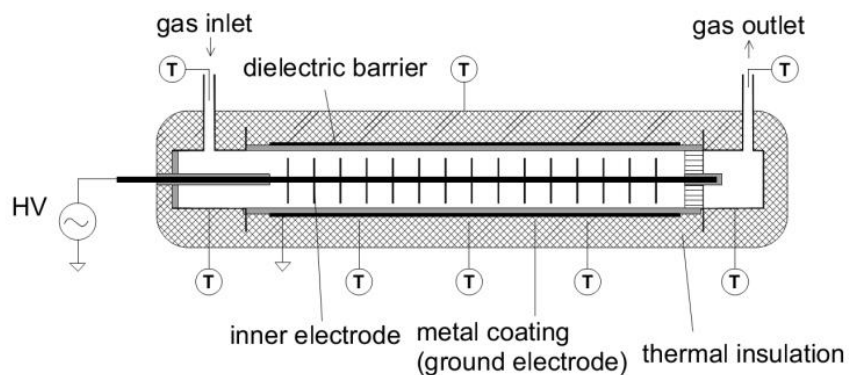


Figure 2.12. DBD reactor by Siemens, Germany [101].

The effect of external magnetic field for the other cases was found to be insignificant. This result indicated the plasma type change from capacitive to inductive plasma under higher flow rates and higher applied power. Additionally, the yield per mass basis was about 80% at 1 kW under all flow rates, whereas the energy efficiency was less than 1% at these conditions. The energy efficiency increased to about 3% when the yield was about 20%.

Zheng *et al.* [103] experimentally studied the dissociation of CO₂ and CO in a dielectric barrier discharge (DBD) plasma reactor as the applied voltage, humidity and concentration of reactant gas changed. The carrier gas was either Ar or oxygen. The reactor consisted of two quartz tubes with an outside diameters of 10 mm and 32 mm and a length of 200 mm. One stainless steel rod as an electrode was placed inside the inner quartz tube, and a stainless steel band was circled around the inner tube as shown in Figure 2.13. The voltage was varied from 0 to 9 kV at a frequency of 2.2 kHz, and the total flow rate was kept constant at 2 L/min. The results showed that at zero humidity the conversion ratio of CO₂ had a maximum value of about 9% at 4 kV for Ar carrier, and it was constant about 1.5% for oxygen system. The CO₂ conversion decreased almost linearly with increasing CO₂ concentration for both systems. For CO, as the applied voltage increased to 7.2 kV at zero humidity, the conversion ratio of CO increased to about 35% for O₂ and 8% for Ar. The convergence ratio for oxygen system was higher than Ar system since atomic oxygen reacted with CO to form CO₂. Increasing the CO concentration decreased the conversion ratio of CO similar to CO₂ case. Finally, the energy conversion efficiency was about 1% and 1.6% at 7.2 kV for CO₂ and CO, respectively. The energy conversion efficiency increased to 10% and 9.6% at 1.8 kV for CO₂ and CO, respectively.

Finally, Li *et al.* [104] summarized the conversion ratio for methane dissociation using different plasma reactors at atmospheric conditions as well as the specific energy required to convert methane into acetylene, ethane and hydrogen. Table 2.6 shows this comparison.

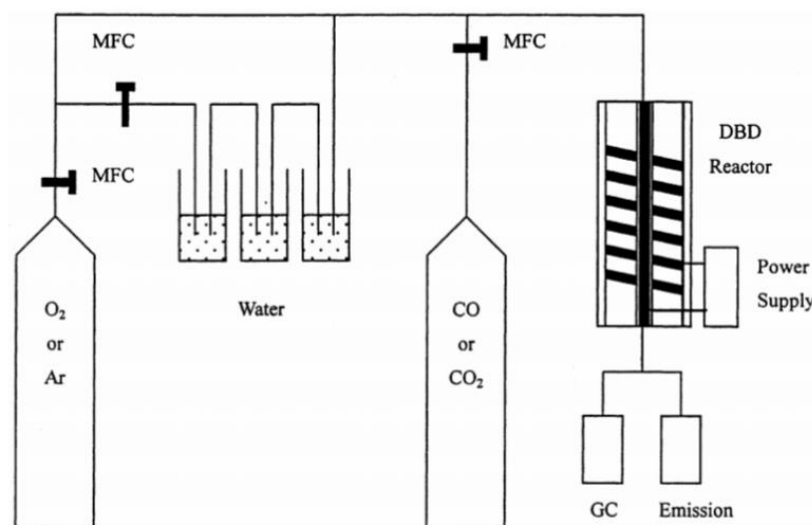


Figure 2.13. Schematic of the experimental setup for the study of Zheng *et al.* [103].

Table 2.6. Conversion and energy cost for methane reforming into C₂ hydrocarbons and H₂ using different atmospheric non-thermal plasma discharge methods [104].

	Methane Conversion (%)	Acetylene Formation (eV/mol)	Ethane Formation (eV/mol)	Hydrogen Formation (eV/mol)
Pulsed spark	18-69	14-25	35-65	10-17
Pulsed streamer	19-41	17-21	38-59	12-19
Pulsed DBD	6-13	38-57	137-227	47-75
AC DBD	5-8	116-175	446-637	151-205

2.3.2 Microdischarge Plasma Studies

This subsection summarizes the studies to show the applications of microdischarge plasma reactors in the literature, as well as MHCD reactors for gas dissociation.

Shin and Raja [105] combined a DBD plasma generator with microdischarge plasma actuator for pure helium or pure nitrogen. The microdischarge plasma actuator was used as a precursor or a catalyst to DBD reactor. Figure 2.14 shows the schematic of

their design. The hybrid reactor consisted of 635 μm -thick upper alumina, 100- μm thick middle mica and 200- μm thick lower mica dielectrics with a 50 μm -thick common nickel or aluminum cathode electrode. Four holes with diameter of 342 μm were used for the microdischarge plasma actuator. The discharge gap for DBD plasma generator was 6 mm for helium and 3 mm for nitrogen. The power requirement for microdischarge actuator was 3.2 and 6.6 W at 15 kHz for 300 and 700 Torr, respectively. The average breakdown voltage for DBD reactor was measured as 1143 V. The addition of microdischarge actuators reduced the required voltage for DBD reactor by about 50% for both helium and nitrogen. Current of 4 mA was measured at 15 kHz, 300 Torr and 500 V for helium with 6 mm gap, and peak current of 9 mA was measured at 10 kHz, 300 Torr and 2.8 kV_p for nitrogen.

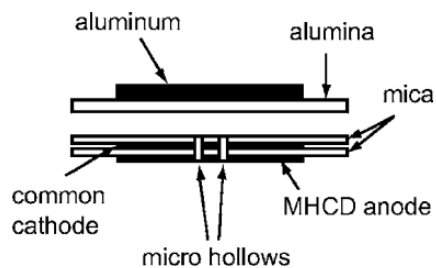


Figure 2.14. Schematic of hybrid DBD microdischarge plasma reactor by Shin and Raja [105].

Koehnur *et al.* [106] modeled one-dimensional, parallel-plate DC microdischarge plasma reactor for helium. The reactor had a gap of 250 μm , operated at 250 Torr. The applied voltage and current density varied from 140 to 190 V and from 100 to 2000 mA/cm², respectively. The current density of 2000 mA/cm² resulted with maximum gas temperature of 1500 K while 100 mA/cm² yielded to a maximum gas temperature of 340 K. The corresponding maximum electron temperatures were about 10 and 40 eV.

However, the charge density at lower current density was two orders of magnitude less than that at higher current density on the order of 10^{12} cm^{-3} and 10^{14} cm^{-3} . The authors also concluded that the microdischarges had generally nonhomogeneous charge distributions in the discharge gap, and a cathode sheath generally occurred.

A tubular microdischarge thruster was modeled for microsattellites by Sitaraman and Raja [18]. The inlet and exit diameters of the tube were $100 \text{ }\mu\text{m}$ and $300 \text{ }\mu\text{m}$, respectively, and the length of the tube was $560 \text{ }\mu\text{m}$. The electrodes were embedded in the dielectric which had a dielectric constant of 9, and the electrodes were separated by $160 \text{ }\mu\text{m}$. The width of the electrodes was $115 \text{ }\mu\text{m}$, and the distance between the flow and electrodes was $40 \text{ }\mu\text{m}$. Argon was fed to the thruster, and a peak voltage of 600 V was applied at either 10 or 20 MHz . The inlet pressure was 40 kPa , and the flow rate was 0.55 mg/s . Figure 2.15 shows the schematic of their design and the pressure distribution inside the reactor. Total of $269 \text{ }\mu\text{N}$ thrust was obtained while the gas temperature increased by only 150 K , and the maximum current density was about 600

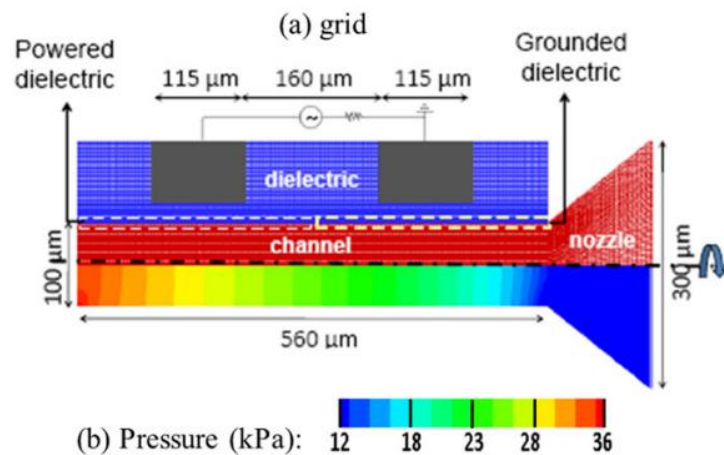


Figure 2.15. Schematic of and pressure distribution within the tubular microdischarge thruster modeled by Sitaraman and Raja [18].

mA/cm^2 at a frequency of 10 MHz. When the frequency was 20 MHz, thrust reached the value of 278 μN , and the thermal power dissipation also increased from 62 to 84 mW due to Joule heating.

Kushner [107] numerically modeled a cylindrical microdischarge device whose schematic is given in Figure 2.16. The hole for Ar gas in the center of the tube was 100 μm in radius near the anode and 150 μm in radius near the cathode. The thickness of the dielectric was 200 μm , and the electrodes were 100 μm thick. There was no flow in the tube, and in the base case 2 mA was applied at the pressure of 250 Torr. For the base case, the voltage of 181 V was observed and the maximum electron temperature was 6.1 eV with the maximum electron density of $2.2 \times 10^{14} \text{ cm}^{-3}$. Moreover, the peak electric field was estimated as $80 \text{ kV}/\text{cm}^{-1}$ and the temperature of the gas increased to 580 K. As the pressure varied, the Paschen curve was obtained with a minimum potential of 165 V at 125 Torr. Consequently, the electron density increased with increasing pressure. The temperature in the center of the tube was 200 K higher in the case of 50 Torr when compared to 500 Torr. When the current through the reactor was increased from 0.15 mA to 4 mA, the voltage increased from 138 V to 196 V and the peak gas temperature increased from 360 K to 1100 K. In the case of multistage microdischarge where two metal-dielectric-metal configurations were stacked together, the peak electron densities and gas temperatures were comparable to those of one reactor, whereas the current was split equally into two. Kushner [107] also stated that the microdischarge plasma can reach the power densities such that only pulsed macroscopic discharges can go up to. However, high power density yields to larger momentum transfer from electric field to gas, and thus, the temperature of the gas is expected to increase.

There are only a few experimental studies that illustrated the use of MHCD reactors for gas dissociation prior to this study. Qui *et al.* [108] studied hydrogen generation from ammonia at atmospheric conditions using a molybdenum electrodes separated by a 250- μm -thick mica plate. The discharge hole was 100 μm in diameter. When the inlet concentration of ammonia was 6.25% in argon, the authors were able to dissociate about 20% of the ammonia and achieved an energy efficiency of 11%. They showed that the conversion yield and energy efficiency increased linearly with the residence time. In another study, Hsu and Graves [109] used a MHCD reactor with a discharge hole of 200 μm in diameter and 460 μm in length to dissociate NH_3 and CO_2 , separately. They reported maximum conversion yields of about 30% for NH_3 at a pressure of 700 Torr and about 47% for CO_2 at a pressure of 250 Torr.

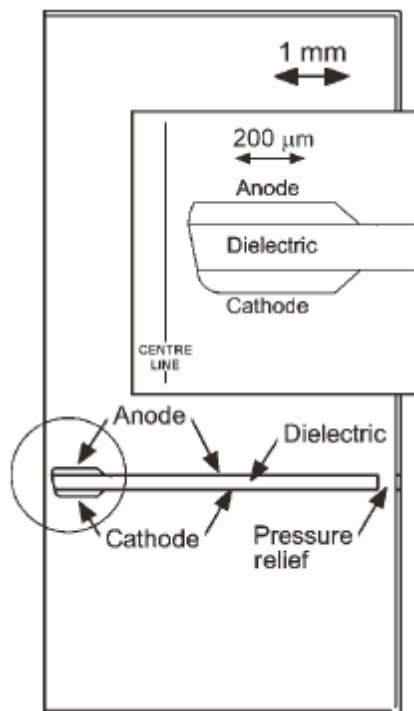


Figure 2.16. Schematic of microdischarge device modeled by Kushner [107].

The previous studies showed the operating conditions, power requirements and dissociation capabilities of plasma reactors. Although these studies showed variety in operation, design and application, they mainly focused on dielectric barrier discharge reactors and plasma generation using inert gases. To our knowledge, there is no study that investigates the syngas production in a microhollow cathode discharge plasma reactor at atmospheric pressure and about room temperature.

2.4 STATE-OF-THE-ART SYNGAS PRODUCTION METHODS FROM CO₂ AND H₂O

A number of studies reported different methods for simultaneously dissociating CO₂ and H₂O for syngas production. These methods can be categorized as electrochemical, photochemical and thermochemical production. This section summarizes these state-of-the-art different methods for syngas production and compares them in terms of their energy efficiencies, production rates, operation times and temperatures.

Delacourt *et al.* [110] studied an electrochemical cell to produce syngas from H₂O and CO₂ mixture at room temperature. They suggested a cell similar to a proton exchange membrane fuel cell with some modifications for CO₂. They used silver as cathode, platinum-iridium alloy as anode, and aqueous 0.5 M KHCO₃ solution between the cathode and Nafion membrane. CO₂ was fed to the cathode side with a flow rate of 20 mL/min, whereas deionized water was recirculated at the anode side with a flow rate of 27 mL/min. The authors stated H₂ to CO ratio of 2 at a total current density of 80 mA/cm², and at this current density, electrical-to-chemical conversion efficiency of about 35%.

Kumar *et al.* [111] studied the generation of H₂ and CO simultaneously from H₂O and CO₂ using photochemical cell in which Re(bipy-tbu)(CO)₃Cl and p-Si catalysts were

used in non-aqueous medium. The authors dissociated water up to 1.5 mL in acetonitrile of 30 mL at 1 atm CO₂. The authors showed that H₂ to CO ratio of 2 was possible when the electrolysis was performed at -1.9 V with respect to Fc/Fc⁺. These conditions achieved at a charge of about 9.8 C after 110 minutes. The authors also reported a light-to-chemical energy conversion efficiency of 4.6% when monochromatic light at 661 nm was used at an intensity of 95 mW/cm².

Chueh *et al.* [44] constructed a prototype of a solar thermochemical reactor to dissociate CO₂ and H₂O using ceria. The reactor was cylindrical with a cavity receiver of absorptivity of 94%, and the walls of the cylinder with a radius of 35 mm and a height of 102 mm was covered with monolithic and porous ceria of 325 g. Argon was used as a carrier gas, and the incident radiation was set to 1.9 kW at 1500 suns. At these conditions, the temperature of ceria increased up to 1640°C, and the maximum solar-to-chemical conversion efficiency was achieved as 0.8%. The maximum production rates of H₂ and CO were about 1.5 and 5 mL/min/g_{ceria}, respectively. Furler *et al.* [112] studied similar solar thermochemical reactor with 127 g ceria, and reported that it was possible to achieve H₂-to-CO ratios from 0.25 to 2.34 when H₂O-to-CO₂ ratios at the reactor influent varied from 0.8 to 7.7. The peak production rates of H₂ and CO were 0.32 and 0.16 mL/min/g_{ceria} at power input of 3.6 kW for reduction (30 minutes) and 0.7 kW for oxidation (15 minutes). Recently, Scheffe *et al.* [113] stated that the solar-to-chemical fuel efficiency increased by 12 times when the mass of ceria increased from 90 to 1400 g by scaling up the reactor volumetrically.

For dissociating H₂O and CO₂, Ermonoski *et al.* [114] suggested another solar thermochemical reactor that had moving packed beds carrying reactive particles such as CeO₂. The authors numerically analyzed their system and stated that solar-to-chemical

could theoretically reach 30% for operating temperatures up to 1500°C. Smestad and Steinfeld [115], Bader *et al.* [116] also reported that theoretical solar-to-chemical energy efficiencies could go up to 30% in a solar thermochemical reactor when metal oxides were used as catalysts. However, these efficiency calculations did not take into account the energy required for quenching the products.

More recently, Jin *et al.* [117] reported H₂O and CO₂ dissociation with zinc powder and analyzed the autocatalytic formation of formic acid (HCOOH). They used aqueous NaHCO₃ as CO₂ source, and the pH of the solution was adjusted by NaOH or NaCl as the pH of the solution affected the dissociation. Their results showed that the maximum formic acid yield of about 80% at temperature of 325°C, Zn of 10 mmol, NaHCO₃ of 1 mmol, reaction time of 90 minutes and initial pH of 8.6. The maximum Zn-to-HCOOH energy conversion efficiency was reported as 16.9% at the yield of 70% when Zn:NaHCO₃ ratio was 3. Assuming Zn-to-ZnO energy conversion efficiency of 30%, the overall solar-to-HCOOH energy conversion efficiency was estimated around 5%.

In this study, the MHCD plasma reactor will be evaluated and its advantages and disadvantages over these state-of-the-art methods and processes in the literature will be presented for dissociating H₂O and CO₂ based on operation and manufacturing simplicity, energy conversion efficiency and conversion yield.

Chapter 3

Materials and Methods

This chapter presents the materials and methods used in this study. Section 3.1 introduced the microhollow cathode discharge (MHCD) reactor used in this study with its materials and geometrical dimensions. Section 3.2 describes the experimental setup, specifically the equipment and controllers used in this study with their limitations as well as the measured parameters. The last part of this chapter, Section 3.3, presents the performance metrics in terms of the measured parameters. Throughout this study, these metrics were used to quantify the dissociation and syngas production of the MHCD reactor.

3.1 MICROHOLLOW CATHODE DISCHARGE REACTOR PROTOTYPE

Figure 3.1 shows the schematic of the microhollow cathode discharge (MHCD) plasma reactor. Microhollow cathode discharge plasma reactor consisted of two aluminum electrodes that were separated by mica as a dielectric layer. Mica was selected as dielectric material based on its large operation voltage as explained in detail in Appendix D. Each aluminum electrodes had a thickness of 10 μm , and a single mica layer had a thickness of 150 μm . In this study, mica layers were stacked to increase the electrode separation. The electrodes were attached on the mica plate with an offset to ease the electrical connections to the electrodes as shown in Figure 3.1. A discharge hole was featured through these three layers, and gas was fed through this hole in this study. The width and length of mica were selected such that the discharge would only occur in the discharge hole.

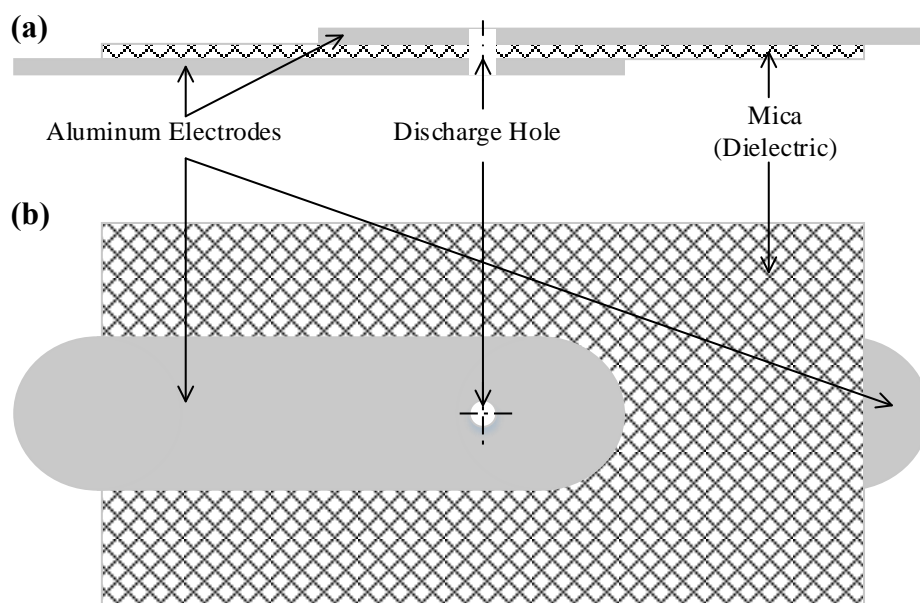
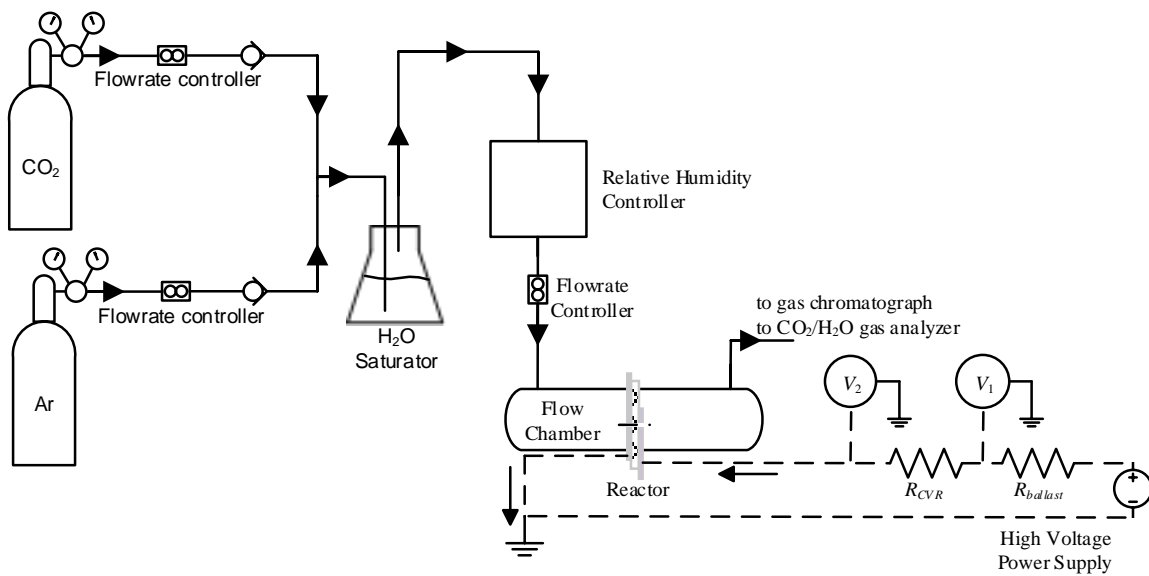


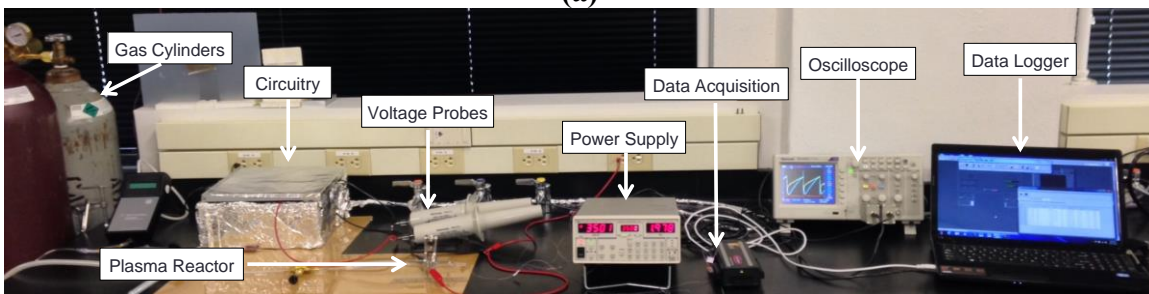
Figure 3.1. Schematic of the microdischarge reactor used in the study, (a) cross-sectional, and (b) top view.

3.2 EXPERIMENTAL SETUP

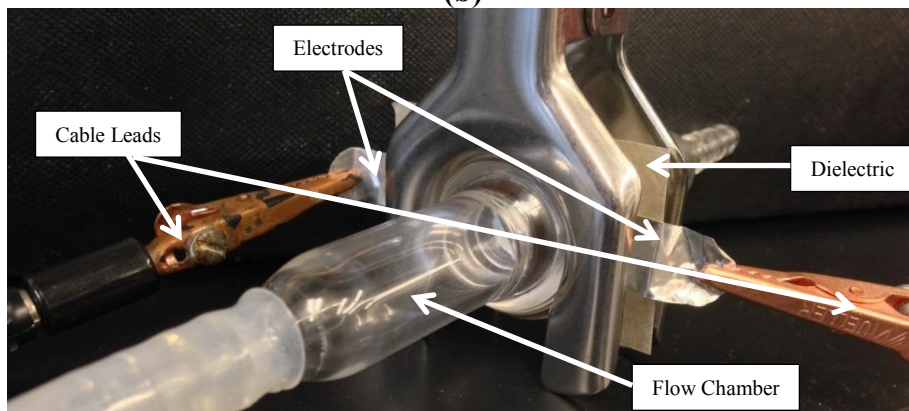
Figure 3.2 shows the schematic and the actual picture of the experimental setup. Carbon dioxide with 99.5% purity (Matheson Tri-Gas) and argon with 99.998% purity (Airgas) were fed to the H₂O-saturator through flow rate controllers. Relative humidity controller (Walz, KF-18/2B) and the CO₂/H₂O analyzer (LI-COR, LI-840A) were used to verify that the gas streams were saturated with water. Then, the H₂O-saturated gas stream was fed to the flow chamber in which the MHCD reactor was placed. The gas samples were taken at the inlet and at the exit of the flow chamber, and their compositions were analyzed in a gas chromatograph (Shimadzu GC-2014). In Appendix C, methodology for gas chromatography is given briefly as well as the calibration of the equipment and sample chromatograms used in this study. The aluminum electrodes of the MHCD reactor were connected to a high voltage power source (Stanford Research Systems, PS350). A ballast resistor with a resistance of 1 MΩ was used to limit the current flowing



(a)



(b)



(c)

Figure 3.2. (a) Schematic, (b) picture of the experimental setup (gas chromatograph, relative humidity controller and CO₂/H₂O gas analyzer not shown in the picture), and (c) close-up picture of the reactor with flow chamber.

to the MHCD reactor and to operate the reactor in the self-pulsing regime. The self-pulsing regime is characterized by a negative differential resistance. This resistance caused a decrease in voltage as current increased. At atmospheric conditions, microdischarges tend to generate arcs which prevent stable operation as glow discharge. This issue was addressed by operating the reactor at the self-pulsing regime [118].

Another resistor, R_{CVR} , was used to measure the current through the MHCD reactor. Voltages, V_1 and V_2 , were measured using two high voltage probes with 3-pF capacitances (Tektronix P6015A, 75 MHz), and these voltages were recorded using an oscilloscope (Tektronix, TDS2002C, 70 MHz).

3.3 ANALYSES

The temporal discharge current, $I(t)$, was calculated by dividing the voltage drop across the current viewing resistor with the magnitude of this resistor, R_{CVR} , as,

$$I(t) = \frac{V_1(t) - V_2(t)}{R_{CVR}} \quad (3.1)$$

The electrical power requirement of the MHCD reactor, $P(t)$, was calculated using the instantaneous voltage V_2 and current I as,

$$P(t) = I(t) V_2(t) \quad (3.2)$$

Finally, the time-averaged power was calculated as,

$$P_{avg} = \frac{\int_0^{t_{exp}} P(t) dt}{t_{exp}} \quad (3.3)$$

where t_{exp} was the duration of each experiment. The energy density, e_v , is then defined as,

$$e_v = \frac{P_{avg}}{\dot{V}_{in}} \quad (3.4)$$

where \dot{V}_{in} is the total volumetric flow rate at the reactor influent. To evaluate the degree of dissociation, H₂O-to-H₂ and CO₂-to-CO conversion yield were defined, respectively, as,

$$\epsilon_{H_2} = \frac{\dot{n}_{H_2,net}}{\dot{n}_{H_2O,in}} \quad (3.5)$$

$$\epsilon_{CO} = \frac{\dot{n}_{CO,net}}{\dot{n}_{CO_2,in}} \quad (3.6)$$

where \dot{n}_i is the molar flow rate of the specie i . Finally, the electrical-to-chemical energy conversion efficiency is defined as,

$$\eta = \frac{\dot{n}_{H_2,net} \Delta \bar{H}_{rxn,H_2O}^o + \dot{n}_{CO,net} \Delta \bar{H}_{rxn,CO_2}^o}{P_{avg}} \quad (3.7)$$

where $\Delta \bar{H}_{rxn}^o$ shows the enthalpy of the corresponding reaction at 298 K and 1 atm. The chemical reactions for H₂O and CO₂ dissociations and their corresponding standard reaction enthalpies can be written as [75, 119],



Note that saturated gases can have maximum of 3.2% water content per mole at room temperature and atmospheric pressure.

Finally, the residence time, t_{res} , was estimated based on the volume of the reactor and the volumetric flow rate as,

$$t_{res} = \frac{\pi D_{hole}^2 d}{4\dot{V}_{in}} \quad (3.10)$$

where D_{hole} is the diameter of the discharge hole, and d is the distance between the electrodes.

In Appendices, Appendix A shows the nomenclature, and Section B.2 shows the numerical code used to calculate the energy conversion efficiency and conversion yields in this study.

Additionally, optical images of the reactor were taken using a CCD camera (Nikon DS-Qi1) and an inverted microscope (Nikon Eclipse Ti-E). The images were analyzed in microscope imaging software (Nikon NIS-Elements) to check the hole size of the reactor and to determine degraded electrode area around the hole. Details of the electrode degradation for the MHCD reactor are given in Section 5.3.4.

Chapter 4

Electrical Characterization Model of MHCD Plasma Reactor

This chapter reports the electrical characterization and an equivalent circuit of a microhollow cathode discharge (MHCD) reactor in the self-pulsing regime. A MHCD reactor was prototyped for air plasma generation, and its current-voltage characteristics were measured experimentally in the self-pulsing regime for applied voltages from 2000 to 3000 V. The reactor was modeled as a capacitor in parallel with a variable resistor. A stray capacitance was also introduced to the circuit model to represent the capacitance of the circuit elements in the experimental setup. The values of the resistor and capacitors were recovered from experimental data, and the equivalent circuit model was able to accurately represent the peak and average power consumption as well as the self-pulsing frequency within the experimental uncertainty. Although the results shown in this chapter was for atmospheric air pressures, the equivalent circuit model of the MHCD reactor could be generalized for other gases at different pressures.

4.1 INTRODUCTION

Voltage and current characteristics of MHCD reactors determine not only the regime that the reactor operates but also the optimum operating voltage and current for the maximum energy efficiency of the reactor. There are four main plasma regimes based on the current; abnormal glow at low current, self-pulsing, normal glow and abnormal glow at high current in the order of ascending current [31, 32]. In the abnormal glow regimes, current increases with voltage, whereas in the normal glow regime the increase in current is independent of voltage. Self-pulsing regime is an unsteady regime between abnormal and normal glow regimes. In the self-pulsing regime, current and voltage

oscillate with time, and current increases with decreasing voltage such that the reactor has negative differential impedance in this region. Additionally, the plasma is confined in the discharge hole in abnormal glow regime at low currents, while the plasma expands outside of the discharge hole on the cathode side in the normal glow regime [31, 32]. In the self-pulsing regime the plasma expands outside of the discharge hole and then retracts back in the hole, and this behavior results in a pulsing effect at a particular frequency and oscillating discharge voltage and current [33].

Previous modeling studies of these reactors operating in the self-pulsing regime did not successfully capture the current and voltage characteristics. This paper addresses these issues, provides experimentally measured current-voltage data over the range of applied DC voltages from 2000 to 3000 V, and proposes a simpler equivalent circuit model for the MHCD reactor operating in the self-pulsing regime. This model is expected to be applicable for wide ranges of gases and pressures. In this study, we specifically present the application of this model for air plasmas at atmospheric pressure.

4.2 CURRENT STATE OF KNOWLEDGE

Only a few studies reported the equivalent circuit of MHCD reactors operating in the self-pulsing regime, most of which focused on the operation under low pressure environments. Hsu and Graves [120] proposed a model composed of a variable resistor in series with an inductor which were in parallel with a capacitor as shown in Figure 4.1a. In their experiments, they used NH_3 in a MHCD reactor with 500- μm thick mica and 100- μm thick molybdenum electrodes and a 200- μm diameter through hole. The reactor was operated at 100 Torr (13.3 kPa). They modeled the variable resistor as a function of the current and fit a second order polynomial to experimental data relating the observed resistance to reactor current. As shown in Figure 4.2b, although the model successfully

captured the negative differential resistance and the temporal variations in current and voltage, the waveform of the simulated current differed significantly from the experimentally measured one.

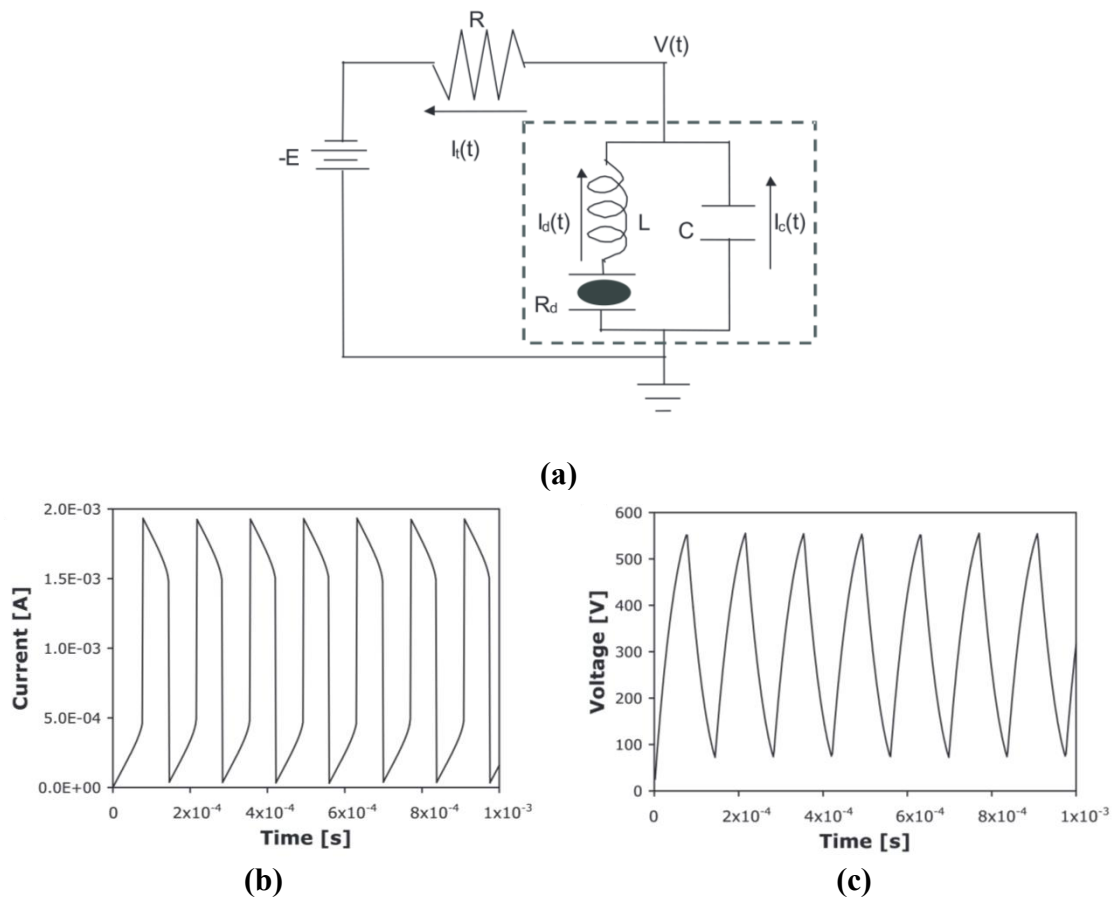


Figure 4.1. (a) The equivalent circuit proposed by Hsu and Graves [120], and (b) corresponding current and (c) voltage characteristics.

In another study, Aubert *et al.* [121] modeled the self-pulsing behavior of a MHCD reactor using argon for the operating pressures from 40 to 200 Torr (5.3 to 26.6 kPa) through a 200- μm hole. Figure 4.2a shows their proposed equivalent circuit that was modeled as two parallel, constant resistors, a capacitor in parallel and a voltage-

controlled switch in series with one of the resistors. The switch was operated based on the breakdown voltage obtained from the Paschen curve. Figure 4.2b shows the simulated voltage and current results as a function of time. Although the authors indicated that their model agreed well with the experimental data, this was neither quantified nor demonstrated by experimental voltage or current data. Additionally, when the applied voltage was increased from 1 to 2 kV, their results showed an increase in the current and frequency of the discharges, and the maximum and minimum discharge voltages were not altered as expected due to constant capacitance.

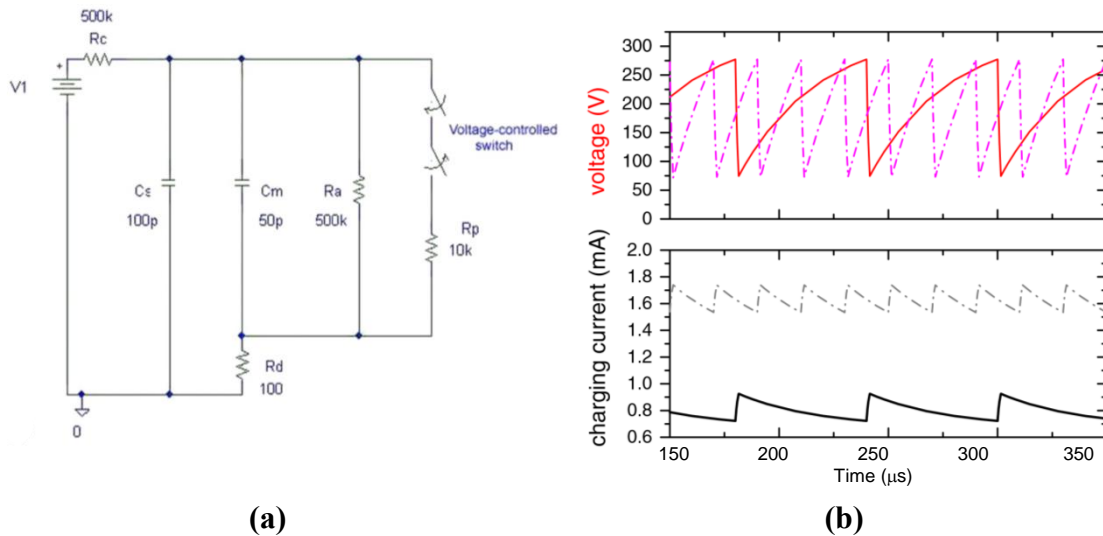


Figure 4.2. (a) The equivalent circuit model by Aubert *et al.* [121], and (b) simulated voltage and current results at applied voltages of 1 kV (solid lines) and 2 kV (dashed lines).

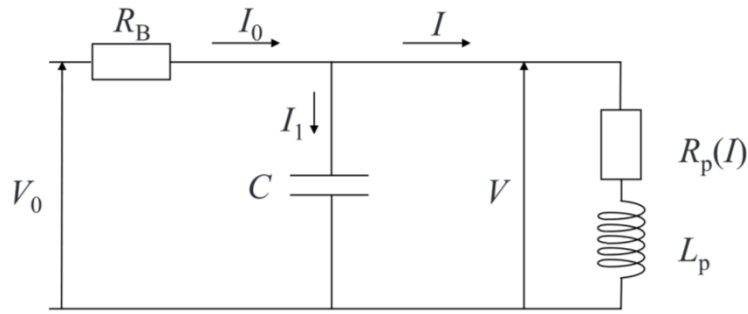
Figure 4.3a shows the equivalent circuit model proposed by Chabert *et al.* [122] who improved upon the model proposed previously by Hsu and Graves [120] modeling the variable resistance of the reactor as,

$$R_d(I_d) = -A_2 \tanh\left(\frac{I_d - I_{limit}}{p}\right) + A_1 \quad (4.1)$$

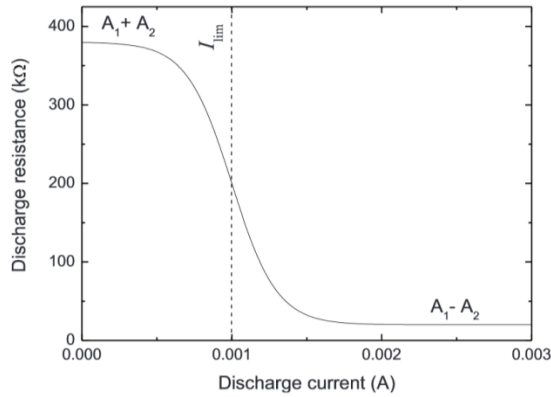
where A_1 , A_2 , p and I_{limit} were constants determined empirically based on experimental data by Aubert *et al.* [121] and Hsu and Graves [120]. Figure 4.3b shows this resistance of the reactor as a function of the discharge current. In this circuit model of Chabert *et al.* [122], the inductor, L_d , was introduced to represent the electron inertia which was defined as the ratio of reactor resistance to the electron-neutron collision frequency in the plasma. The authors indicated that introducing L_d enabled them to model the rise time and frequency of discharges. Nevertheless, eliminating L_d did not affect their simulation results, such as, waveforms or magnitudes of voltage, current or frequency of the discharges. Figure 4.3c shows the results of this model in terms of the voltage across the reactor and the current through the resistance and inductance of the reactor. Their results showed that although this model predicted the waveform of discharge current versus discharge voltage curve of MHCD reactor, the model failed to model the magnitude of peak voltages as mentioned by Lazzaroni and Chabert [123, 124].

Moreover, Lazzaroni and Chabert [123, 124] tried to address the discrepancy between experimental and modeled peak voltages in the equivalent circuit model by Chabert *et al.* [122] by introducing another parameter to their previously fitted R_d equation. The authors added A_3/I_d in Equation (4.1) where A_3 is another constant [123, 124]. The authors also introduced another capacitor in parallel with C_d to model the stray capacitance of the circuit elements and cables [124], and they argued that the stray inductance of the circuit was negligible [122]. Figure 4.4 shows the comparison of experimental and simulated voltage and current. Based on these results, although their model satisfactorily predicted the experimental voltage as a function of time, it predicted

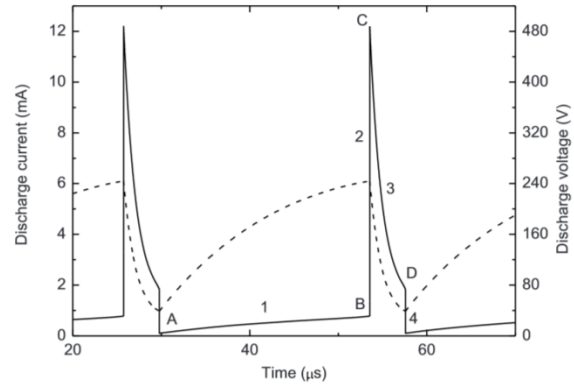
twice of the experimentally obtained peak current in the self-pulsing regime. Additionally, the effects of the experimental conditions on the constants of Equation (4.1) were not discussed.



(a)



(b)



(c)

Figure 4.3. (a) Proposed equivalent circuit by Chabert *et al.* [122], (b) the modeled resistance as a function of discharge current, and (c) the simulated voltage and current characteristics of the proposed circuit.

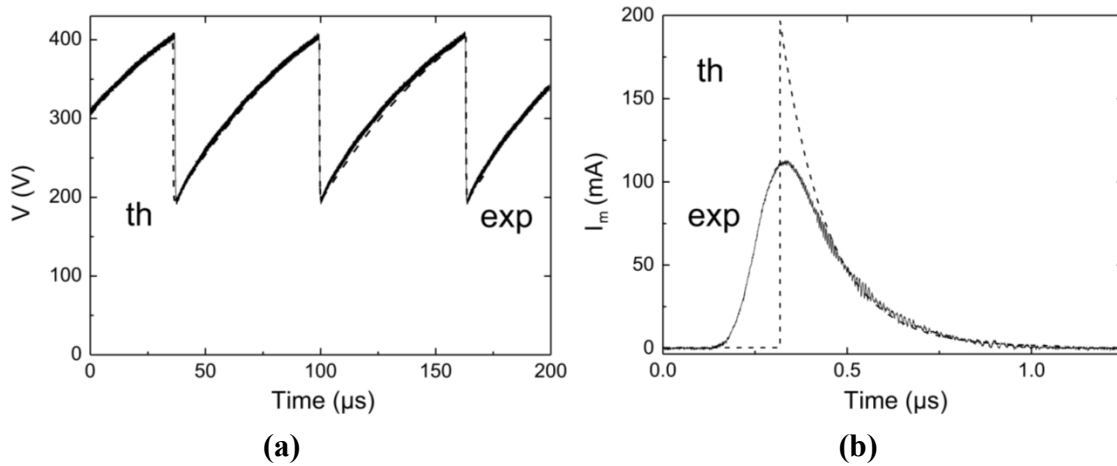


Figure 4.4. Comparison of experimental and simulated results by Lazzaroni and Chabert [123], (a) voltage, and (b) current as functions of time.

In another study, Du *et al.* [125] modeled the equivalent circuit of a MHCD reactor with electrodes of different thicknesses using argon at atmospheric pressure. Figure 4.5a shows their proposed equivalent circuit which consisted of a constant resistor of 14.5Ω with a switch in series and a capacitor in parallel. As shown in Figure 4.5b, the authors justified their model for one charge-discharge cycle only. Thus, their results did not reflect the pulses and the frequency of the self-pulsing regime.

Thus, none of the models reported in the previous studies successfully captured the current-voltage characteristics of MHCD reactors in the self-pulsing regime with good accuracy. This chapter addresses this gap in the literature by proposing a simple equivalent circuit model derived from experimentally measured current and voltage data over the range of applied DC voltages from 2000 to 3000 V for air plasma at atmospheric pressure.

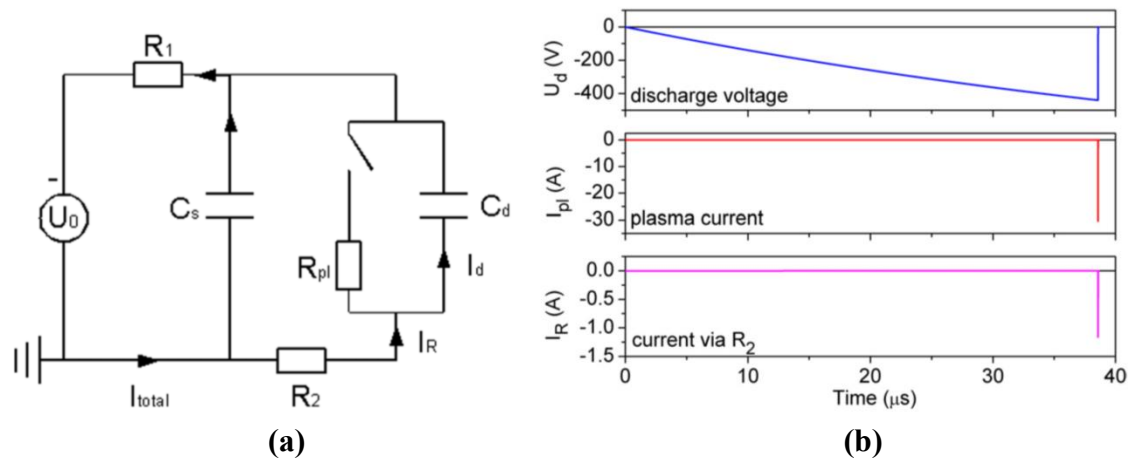


Figure 4.5. (a) The equivalent circuit proposed by Du *et al.* [125], and (b) corresponding simulation results.

4.3 EXPERIMENTAL PARAMETERS

Figure 3.1 shows the schematic of the microhollow cathode discharge (MHCD) reactor used in this study. The aluminum electrodes were separated by mica layer with a thickness of 150 μm , and the diameter of the through hole was about 400 μm . The applied voltage was varied from 2 to 3 kV with 0.25 kV increments. This range of applied voltage was selected based on the breakdown voltage of air at atmospheric pressure from Paschen curve [25, 75, 126]. Voltage and current values at each applied voltage were obtained as explained in Sections 3.2 and 3.3. This part of the study was performed in atmospheric stagnant air. Therefore, the gas tanks, the H₂O saturator, the humidity, temperature and flow rate controllers shown in Figure 3.2 were not used in this part. Additionally, the gas chromatography was not used in this part since the aim was to electrically characterize the MHCD reactor.

4.4 RESULTS

4.4.1 Experimental Characterization of the Reactor

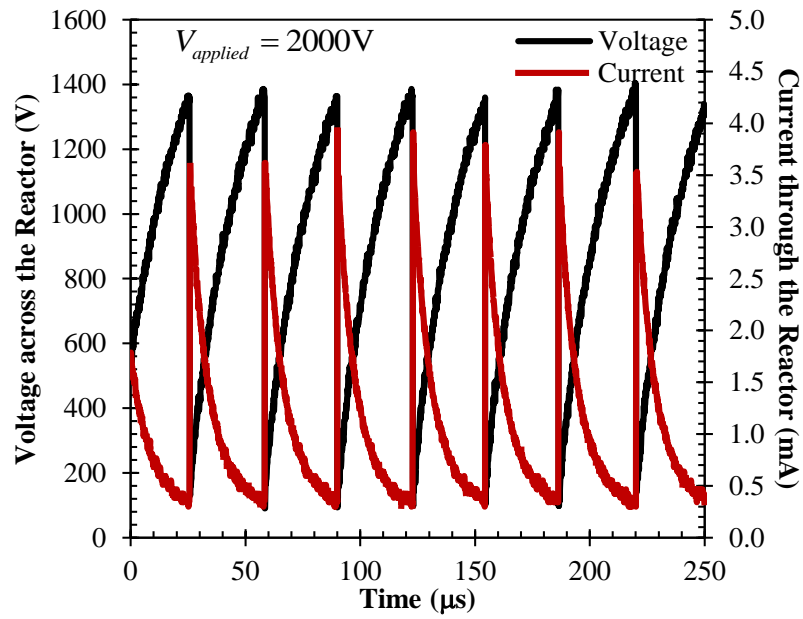
First, the current-voltage behavior of the MHCD reactor was characterized. Figure 4.6a shows the experimentally measured current and voltage of the reactor for air at atmospheric pressure at an applied DC voltage of 2000 V. The figure shows that the reactor voltage increased to about 1400 V right before the discharge and quickly dropped to 90 V as the current increased from about 0.3 to 3.9 mA. The duration of one charge-discharge cycle was about 32.7 μs which corresponds to a self-pulsing frequency of 30.6 kHz. This was consistent with the frequency range of MHCDs in self-pulsing regime reported in the literature [120]. Figure 4.6a illustrates that between consecutive discharges, reactor voltage increased and current exponentially decayed with time, indicating a capacitive behavior of the reactor. When the voltage difference between the electrodes reached the breakdown voltage of the gas, discharge occurred and electrons were liberated from the cathode ultimately reaching the anode. Thus, at the beginning of discharge, current instantly rose while voltage rapidly decreased below the breakdown threshold. Due to a smaller voltage across the electrodes, the electrons could not accelerate enough to ionize the gas within the reactor. Thus, the electron density in the reactor decreased causing a decay in current and buildup of charges at the electrodes. The accumulated charges at the cathode increased the voltage across the electrodes and the cycle continued. This charge-discharge period determined the “self-pulsing frequency” of the reactor. Additionally, Figure 4.6a shows that the current and voltage did not decrease to zero indicating plasma was not completely neutralized after the discharge and charges were always present in the reactor while the reactor was being charged. This corroborates

the observation that the recorded breakdown voltages for the MHCD were lower than that of what is predicted from the Paschen curve.

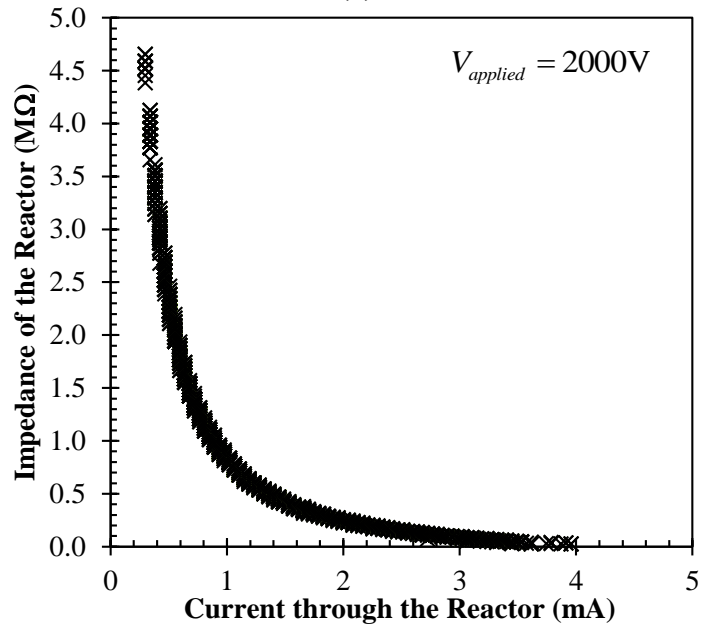
Moreover, Figure 4.6b shows the magnitude of the impedance of the MHCD reactor as a function of the reactor current. The figure shows that the impedance of the reactor decayed exponentially and reached its minimum at the instant of discharge when the current was at its maximum.

Furthermore, Figure 4.7a shows the experimentally measured peak, time-averaged and minimum currents as functions of the applied voltage from 2000 to 3000 V. The peak values are useful for determining the required power rating of high voltage power supply, whereas the average values are useful for calculating the energy efficiency of the reactor. Moreover, the minimum current signifies the charge density in the reactor just before the discharge. The figure indicates that as the applied voltage increased, the peak, average, and minimum currents increased linearly. At higher applied voltages, larger electron densities were expected due to more energetic collisions. Larger electron density yielded higher peak currents during discharge. As the rate of charges supplied to the reactor was higher at higher applied voltages, it required less time to reach the breakdown voltage. Due to faster charging of the cathode, the current did not have enough time to reach lower values as it did at lower applied voltages, resulting in larger number of charges in the reactor before the discharge. Therefore, the minimum current increased with increasing applied voltage.

Additionally, Figure 4.7b shows the peak and average voltages as functions of the applied voltage. The peak voltages signify the breakdown voltage of the gas in the reactor. As mentioned above, larger number of charges was left in the reactor before the



(a)

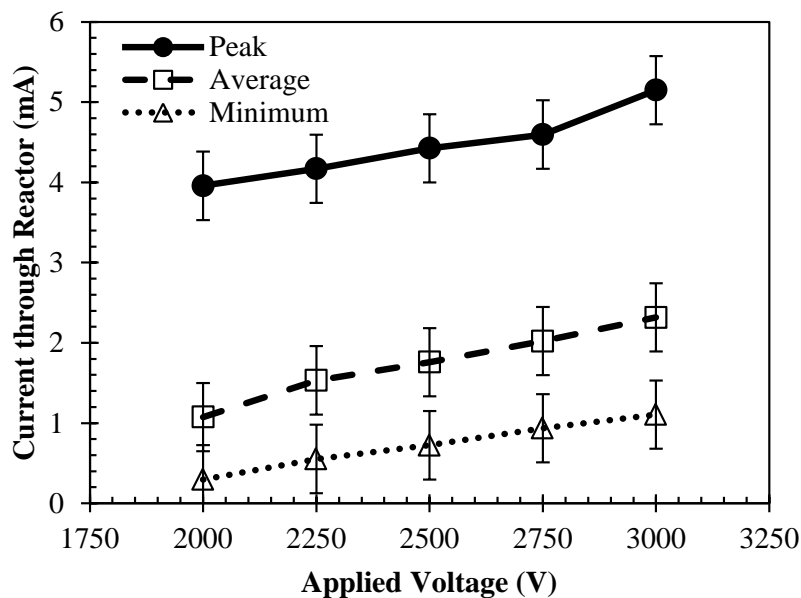


(b)

Figure 4.6. Voltage and current characteristics of the MHCD plasma reactor used in the experiments of this study at an applied voltage of 2000 V, (a) voltage and current as a function of time, (b) impedance of the reactor as a function of current.

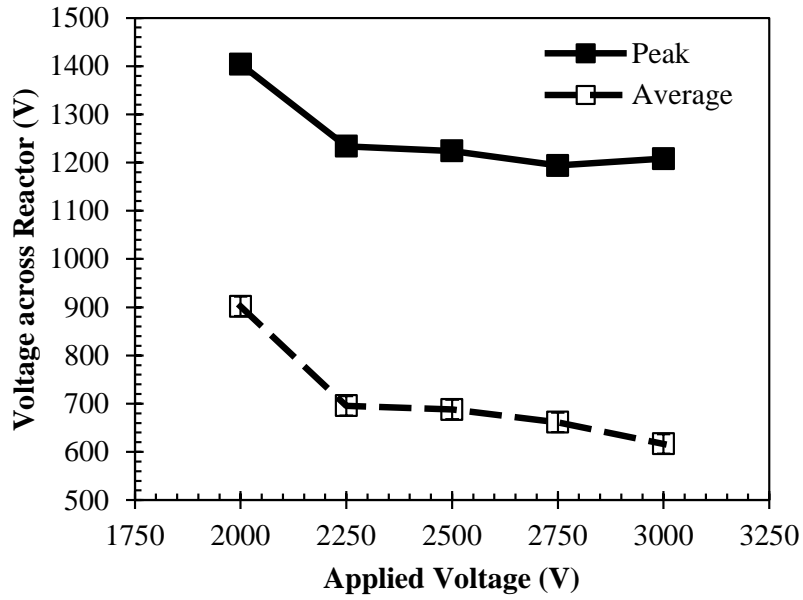
discharge when the applied voltage was increased. These charges reduced the voltage required for breakdown because breakdown requires certain number of charges in the reactor. Thus, these charges resulted in lower breakdown voltages than those predicted from Paschen curve, which assumes no charges and uniform electric field in the reactor. Furthermore, Figure 4.7a and b show an inverse relation between the reactor current and voltage, indicative of negative impedance.

Based on the experimentally measured current and voltage data, Figure 4.7c shows the time-averaged power and self-pulsing frequency as functions of applied voltage. The figure illustrates that both the average power and the frequency increased linearly from 0.7 to 1.5 W and from 30 to 78 kHz, respectively, as the applied voltage increased from 2000 to 3000 V. As the applied voltage was increased, greater charge density was expected to yield larger power dissipation due to non-ionizing and inelastic

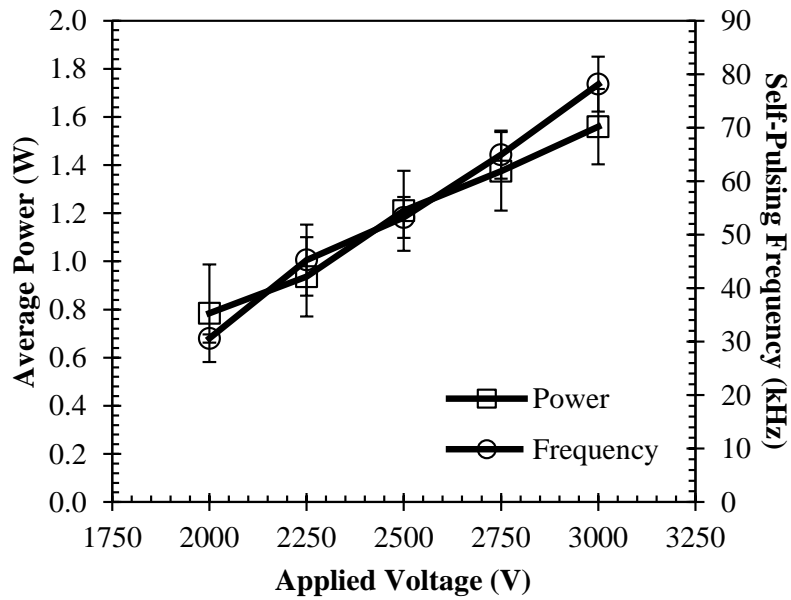


(a)

Figure 4.7 continued on the next page.



(b)



(c)

Figure 4.7. (a) Peak, time-averaged and minimum current, (b) peak and time-averaged voltage (c) time-averaged power and self-pulsing frequency as functions of applied voltage.

collisions. Therefore, average power consumption was increased with increasing applied voltage. Moreover, as mentioned above, less time was required to reach the breakdown voltage of the gas with increasing applied voltage. Thus, self-pulsing frequency increased 2.6 times when the applied voltage increased from 2000 to 3000 V as shown in Figure 4.7c.

4.4.2 Equivalent Circuit Model

Based on the measurements and observations in the previous section, an equivalent circuit was modeled as shown in Figure 4.8 to address the limitations of the previously published models [120-122, 124]. The experimental data presented in the previous section indicated negative differential impedance with a capacitive effect due to temporal current and voltage characteristics during charge-discharge cycles. To reflect these characteristics, the MHCD reactor was modeled as a negative differential resistor, R_d , in parallel with a capacitor, C_d . For simplicity, the capacitance of the reactor, C_d , was assumed to be constant and the characteristics of the negative variable impedance was attributed to a negative differential resistance, R_d . This approach overcame the issues associated with using a voltage-controlled switch as suggested by Aubert *et al.* [121] and Du *et al.* [125] The switch yielded infinite resistance and zero current through the reactor when the switch was off, whereas the experimental data indicated shown in Figure 4.6a indicated that current never decreased to zero. In addition, another capacitor, C_{stray} , was introduced to represent the equivalent stray capacitance of the experimental setup. Finally, the inductance of the reactor represents the inertia of the charges [122]. In this study, using an inductance from 1 nH to 10 mH in series with the rest of the reactor model changed the magnitudes current and voltage less than 2% for all cases in this study. Thus, the inductor was not used in this model for simplicity.

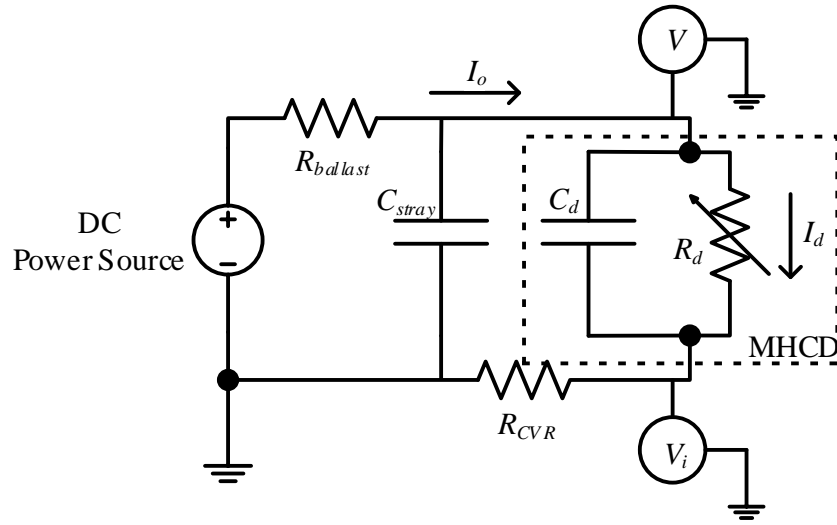


Figure 4.8. Equivalent circuit of the experimental setup.

Assuming constant capacitances and negligible inductance, the impedance shown in Figure 4.6b was modeled as a negative differential resistance, R_d , and was modeled with a double exponential decay function as,

$$R_d(I_d) = a \cdot \exp(b \cdot I_d) + c \cdot \exp(d \cdot I_d) \quad (4.2)$$

where a , b , c and d were empirical parameters obtained through regression analysis. This equation, modeled the variable impedance with a goodness-of-fit R^2 , values greater than 0.998 for all data. However, the asymptotic behavior of Equation (4.2) yielded some numerical singularities in the simulations. Thus, the resistance of the reactor was limited between R_{min} and R_{max} to eliminate the numerical singularities in the model. By limiting the resistance, non-zero minimum current and voltage values were also satisfied as experimentally observed. The next section discusses how these parameters were assigned and attributed to the experimental observations.

4.4.3 Analysis

This section shows how the magnitudes of the circuit elements in the model were calculated using experimental data, namely V and V_i in Figure 4.8. From Kirchoff's Law, the relation between voltage and current through the MHCD reactor was written for the circuit shown in Figure 4.8 as,

$$\frac{dV_d}{dt} = \frac{V_{applied} - V_d}{R_{ballast} (C_d + C_{stray})} - \frac{I_d}{C_d + C_{stray}} \quad (4.3)$$

where V_d is the voltage across the reactor, i.e., the difference of V and V_i . Assuming that the current only passes through R_d at the instant of discharges, the relation between the voltage across the reactor and the applied voltage could be written as,

$$V_d = V_{applied} \left(1 - \exp\left(-\frac{t}{\tau_d}\right) \right) \quad (4.4)$$

where

$$\tau_d = R_{ballast} (C_d + C_{stray}) \quad (4.5)$$

and the time constant, τ_d , can be obtained from the experimental data. Thus, the capacitance of the reactor, C_d , which is assumed to be constant, can be calculated from the time constant. Additionally, the temporal discharge current, I_d , is calculated by dividing the voltage drop across the current viewing resistor, V_i , with the magnitude of this resistor, R_{CVR} , as,

$$I_d = \frac{V_i}{R_{CVR}} \quad (4.6)$$

The magnitude of the impedance of the reactor, Z_d , is calculated at each time interval as the ratio of discharge voltage to the discharge current as,

$$|Z_d| = \frac{V_d}{I_d} = \frac{R_d X_C}{\sqrt{R_d^2 + X_C^2}} \quad (4.7)$$

where X_C is the resistance equivalent of the capacitor as,

$$X_C = \frac{1}{2\pi f C_d} \quad (4.8)$$

where f is the frequency. Since the capacitance of the reactor is assumed to be constant, X_C is also constant for each applied voltage value. Thus, using Equation (4.7), the resistance of the reactor is calculated as a function of time.

4.4.4 Modeling Parameters and Simulation Results

Simulations using the equivalent circuit model were performed using the AC/DC module of COMSOL Multiphysics[®] version 4.3. The voltage drop across and current flow through all circuit elements in Figure 4.8 were simulated as functions of time with a time resolution of 0.1 μ s. A sensitivity analysis was performed to ensure that the simulation results were independent of time resolution and convergence criterion at the applied voltage of 2500 V. When both the time resolution and the convergence criterion were decreased by an order of magnitude the simulation results did not vary by more than 3%.

The simulation results showed that the capacitance of the reactor was the major parameter controlling the self-pulsing frequency. As the reactor capacitance was increased, longer times were required to charge the reactor, and thus, the self-pulsing frequency decreased. For each applied voltage, the magnitude of the capacitance of the

reactor was varied to match the experimentally obtained frequency. Table shows the magnitudes of the capacitance of the reactor at each applied voltage. As the applied DC voltage was increased from 2000 to 3000 V, the reactor capacitance decreased by 34% to reflect the increase in the self-pulsing frequency in Figure 4.7c. For all cases, the magnitude of the capacitance of the MHCD reactor was found to be on the order of pF.

Using the capacitance value and the measured impedance, resistance of the reactor, R_d , was determined at each time interval. Then, parameters of Equation (4.2) were obtained through regression analysis and this equation was used in the simulations. Table shows the parameters for Equation (4.2) as well as the upper and lower limits of the resistance. The results showed that the reactor resistance remained at its upper limit, except during the discharge. The upper limit of the reactor resistance was determined by the remaining charges in the reactor before the discharge. As larger number of charges was present in the reactor at larger applied voltages, the maximum resistance was smaller. When the discharge occurred, the reactor resistance decreased to its minimum value. The minimum resistance was the resistance of the plasma which is a function of the collision frequency, the electron energy and density in the plasma [127, 128]. The maximum and minimum resistances were varied to match the peak and minimum voltages, respectively for each applied voltage. For all cases, the magnitude of the maximum resistance was on the order of M Ω .

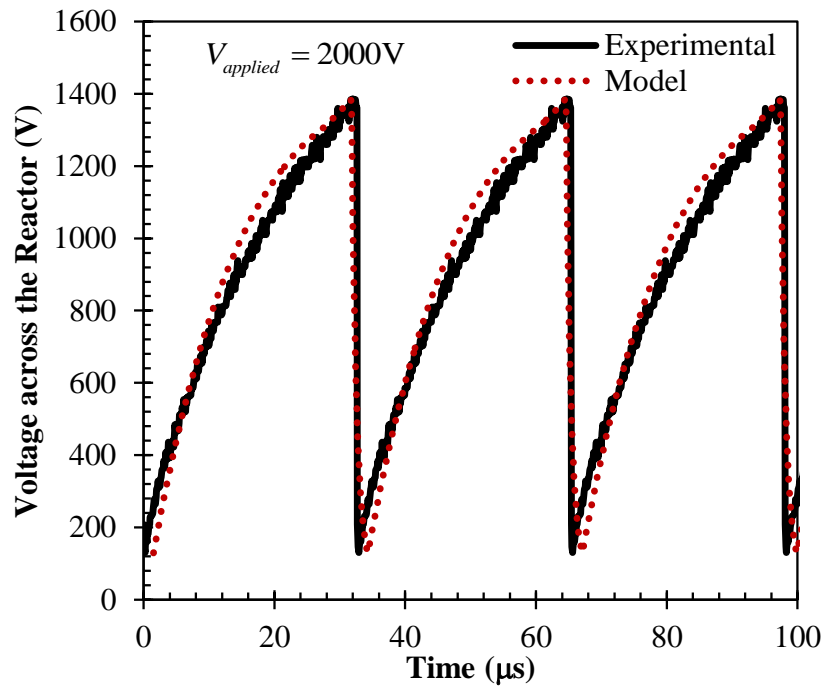
Using the negative differential resistance, R_d , with the capacitance, C_d , the temporal current-voltage waveforms of the self-pulsing behavior of the reactor were successfully simulated. Due to the existence of the experimental circuit around the reactor, it was not possible to match the peak currents without a stray capacitance that also changed with applied voltage. Table also shows the values of stray capacitance of

the model. Similar to the reactor capacitance, the stray capacitance decreased with increasing applied voltage. Although, these results captured both quantitatively and qualitatively the experimental observations of the current-voltage characteristics of the reactor, the values of the reactor capacitance and resistance reported in this study were larger than the ones reported in the literature [120, 123]. This difference was mainly attributed to the higher pressure used in this study.

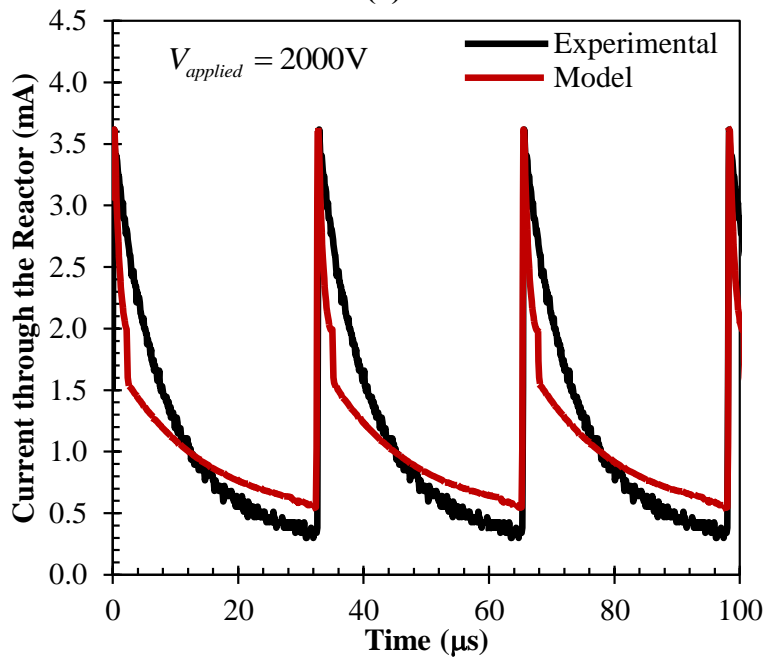
Table 4.1. Coefficients used in Equation (4.2), and parameters used in the equivalent circuit model.

$V_{applied}$ (V)	C_d (pF)	a (M Ω)	b (A ⁻¹)	c (M Ω)	d (A ⁻¹)	R_{min} (k Ω)	R_{max} (M Ω)	C_{stray} (pF)
2000	15.0	14.1	-5270	2.39	-1163	45.9	3.15	2.29
2250	13.6	9.09	-4170	2.54	-1242	48.6	1.68	2.50
2500	12.2	6.44	-2680	1.43	-821.6	45.6	1.11	1.93
2750	11.2	6.66	-2687	1.72	-837.5	39.6	0.94	1.40
3000	9.84	9.14	-2960	2.13	-872.1	55.6	0.79	1.50

Figure 4.9 compares the temporal voltage and current characteristics obtained from experiments and simulations at 2000 V. Similar results were obtained for all other applied voltages, and the results were not repeated here for brevity. The maximum and minimum voltages from simulation agreed with the experimental ones within 2.5% for all cases, giving goodness-of-fit R^2 value of 0.93. Similarly, the peak current agreed with the experimental one within 1.0%. However, the model overestimated the value of the minimum current by about 0.35 mA. The model for current data resulted with R^2 value of 0.86.



(a)



(b)

Figure 4.9. Comparison of experimental data and modeling results for (a) voltage across and (b) current through the reactor as functions of time.

Finally, Figure 4.10 compares the peak and average power as functions of applied voltage for experimental data and results of the simulations. The figure shows that the peak and average power obtained from simulation results agreed with the experimental results within the experimental uncertainty. The maximum discrepancy between the experimental and simulation results was 3.7% and 8.5% for the peak and average power, respectively.

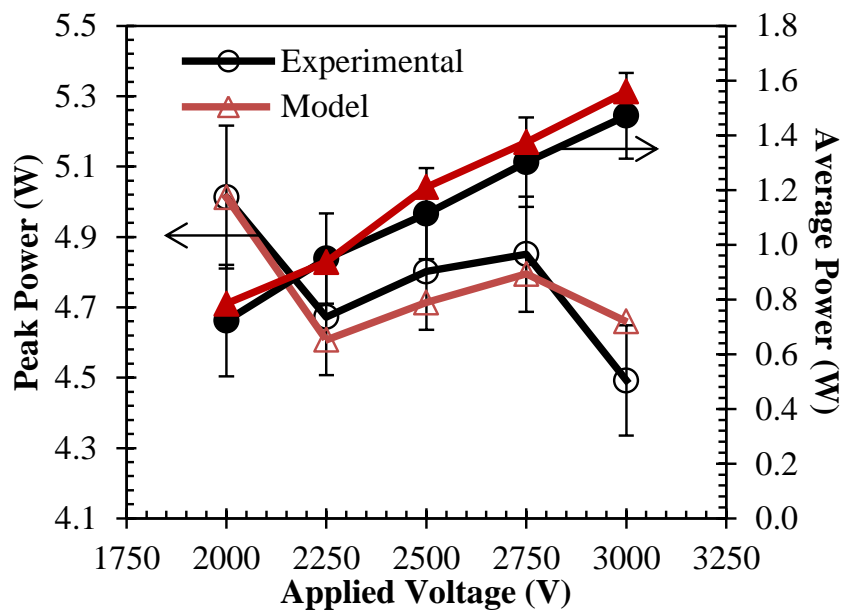


Figure 4.10. Comparison of experimental data and modeling results for peak and average power required for the reactor as functions of applied voltage.

4.5 CHAPTER SUMMARY

This chapter presented the electrical characterization and equivalent circuit modeling of a MHCD reactor operating in self-pulsing mode. A reactor was prototyped and was operated for generating atmospheric air plasmas at different applied DC voltages while measuring the voltage across and current through the reactor. The reactor was

modeled as a negative differential resistor in parallel with a capacitor. The introduced equivalent circuit model was in better agreement with the experimental results than the other models reported in the literature in terms of representing both the temporal waveforms and magnitudes of voltage and current. Given the physics of discharges and the nature of MHCD reactors, the equivalent circuit model would be valid for different gases, reactor dimensions and pressures provided that the model parameters are adjusted based on these conditions.

Chapter 5

Dissociation of Carbon Dioxide using MHCD Plasma Reactor

This chapter reports an experimental study on dissociating carbon dioxide using a microhollow cathode discharge (MHCD) plasma reactor operated at 1 atm. The MHCD plasma reactors can be a promising technology for dissociating gases, including CO₂, as they do not require catalysts, operate at equilibrium temperatures that are lower than those in conventional thermochemical processes, and can be inexpensively built and operated. In this study, a MHCD plasma reactor was designed and prototyped for CO₂ dissociation. The prototype consisted of a mica plate as a dielectric layer that was in between two aluminum electrodes with a through hole of 400 μm in diameter. Carbon dioxide balanced with the carrier gas argon was fed through the hole, and parametric experiments were conducted to investigate the effects of applied voltage (from 2.5 to 4.5 kV), flow rate (from 10 to 800 mL/min), and CO₂ mole fraction in influent (from 9.95% to 99.5%) on the composition of the products, electrical-to-chemical energy conversion efficiency, and CO₂-to-CO conversion yield.

5.1 INTRODUCTION

The literature on MHCD plasma reactors focused on plasma generation using noble gases [125, 129, 130]. There are only a few experimental studies that illustrated the use of MHCD reactors for gas dissociation prior to this study. Qui *et al.* [108] studied hydrogen generation from ammonia at atmospheric conditions using a molybdenum electrodes separated by a 250-μm-thick mica plate. The discharge hole was 100 μm in diameter. When the inlet concentration of ammonia was 6.25% in argon, the authors were able to dissociate about 20% of the ammonia and achieved an energy efficiency of 11%

when the residence time was 5 μs . They showed that the conversion yield and energy efficiency increased linearly with the residence time. In another study, Hsu and Graves [109] used a MHCD reactor with a discharge hole of 200 μm in diameter and 460 μm in length to dissociate NH_3 and CO_2 , separately. They reported a maximum conversion yield of about 30% for NH_3 at a pressure of 700 Torr (93.3 kPa) and residence time of 9 μs , and about 47% for CO_2 at a pressure of 250 Torr (33.3 kPa) and a residence time of about 8 μs . However, the authors did not report the energy conversion efficiencies. In these studies as well as in the applications such as surface treatment, thin-film deposition, low pressures have been used to eliminate unstable plasma generation at about 1 atm [28]. To overcome these instabilities and increase the overall conversion efficiency by eliminating the need for low pressures, MHCD reactors can be operated in the self-pulsing regime based on their voltage and current characteristics.

To the best of our knowledge, there is no prior study that experimentally investigates the effects of voltage, flow rate and mole fractions in influent on CO_2 dissociation in a MHCD plasma reactor in the self-pulsing regime at 1 atm. This study aims to address this gap in the literature and reports the optimum operating conditions of MHCD plasma reactor for CO_2 dissociation for maximizing electrical-to-chemical energy conversion efficiency and CO_2 -to-CO conversion yield as the applied DC voltage, inlet flow rate, and CO_2 mole fraction in influent are varied.

5.2 EXPERIMENTAL PARAMETERS

Sections 3.2 and 3.3 present the prototype MHCD plasma reactor and the experimental setup used in this part of the study. A mica plate with a thickness of 150 μm as a dielectric material separated the hollow aluminum electrodes. The discharge hole was featured as about 400 μm in diameter.

Carbon dioxide (99.5% purity, Matheson Tri-Gas) and argon as the carrier gas (99.998% purity, Airgas) were fed to the flow chamber through flow rate controllers. The H₂O saturator, the humidity and temperature controller shown in Figure 3.2 were not used in this part of the study. The gases were sampled at the reactor effluent and analyzed in gas chromatograph.

Based on the atmospheric pressure (1 atm) and the size of the discharge hole used in this study, the breakdown voltage for pure CO₂ was estimated as 2.1 kV using Townsend breakdown mechanism. Based on this estimated breakdown voltage value and the voltage limit of the power supply, the applied DC voltage to the reactor was varied from 2.5 kV to 4.5 kV. In addition, based on the limit of the flow rate controllers, the flow rate of the gas fed to the reactor was varied from 10 to 800 mL/min. Each parameter combination was independently repeated at least 4 times. The error bars in figures reported in the Results and Discussion section below reflect the standard deviation of the data obtained from these replicates.

5.3 RESULTS AND DISCUSSION

The self-pulsing regime was observed through voltage and current measurements for all parameter combinations in this study. Figure 5.1 shows the voltage and current characteristics of the reactor at the applied DC voltage of 4.5 kV and the CO₂ flow rate of 100 mL/min. The voltage and current characteristics of the reactor show two distinct regimes of charging and discharging. In the charging regime, the charges accumulate at the cathode, raising the voltage difference between the electrodes. During this time the current through the reactor exponentially decays as the plasma is not fed with high energy electrons from the cathode. When the voltage difference reaches the breakdown threshold of the gas, discharge occurs and the electrons are liberated from the cathode further

ionizing the gas phase which causes a sharp increase in current and a sharp decrease in voltage. As the voltage decreases below the breakdown threshold, the electrons do not have enough energy to ionize the gas. Thus, the electron density in the reactor decreases and high currents cannot be sustained, such that charging regime takes place again. This charging-discharging characteristic of the MHCD reactor resembles a capacitive behavior. Chapter 4 reported the characterization and modeling of the current-voltage behavior of the MHCD plasma reactor in detail in the self-pulsing regime as a function of applied DC voltage. The MHCD reactor was modeled as a capacitor parallel with a negative differential resistor.

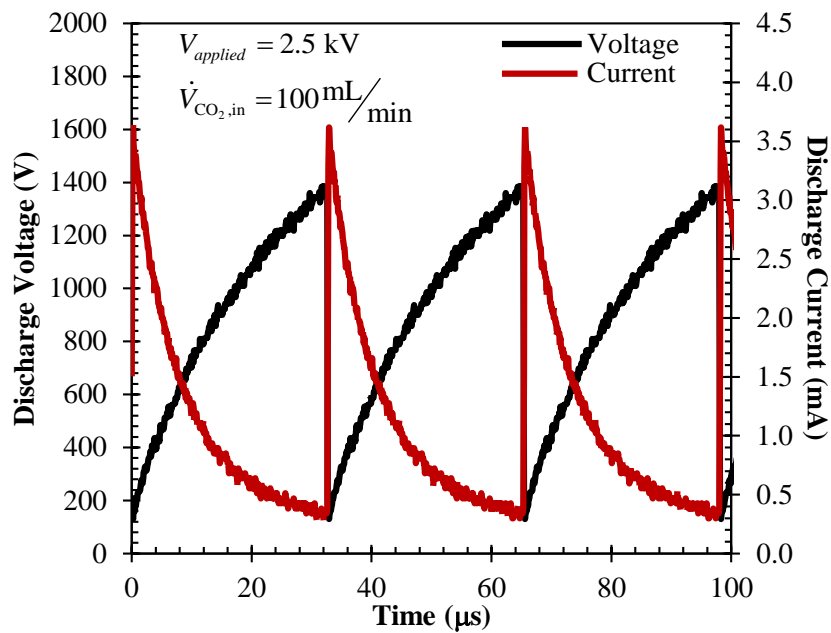


Figure 5.1. Voltage and current of the MHCD plasma reactor as a function of time in the self-pulsing regime.

5.3.1 Effects of Applied Voltage

Prior to experimental investigation, electric field distribution in the reactor before the first discharge was simulated, and the results are given in Appendix D. The simulation results suggested increasing the applied voltage would increase the discharge gas volume based on the electric field distribution. This section complements the simulation results with experiments with the redistribution of charges and electric field in the reactor. First, we investigated the effects of applied DC voltage on the performance of the MHCD reactor in dissociating CO₂. For this purpose, experiments were conducted at varying voltages from 2.5 kV to 4.5 kV while providing the reactor with CO₂ at a molar concentration of 99.5% at a constant flow rate of 100 mL/min. Figure 5.2 shows the concentrations of CO₂, CO and O₂ in the reactor effluent as functions of applied voltage. The results showed that CO₂ concentration in the reactor effluent decreased linearly from 99.4% to 98.3% as the applied voltage increased from 2.5 to 4.5 kV. In addition, CO and O₂ concentrations increased linearly from 0.37% to 1.28% and from 0.10% to 0.42%, respectively, in the same applied voltage range. These observations can be attributed to the electron density and the electron energy distribution of the generated plasmas. First, at large applied voltages the electric fields in the reactor were larger yielding higher electron energies and more energetic collisions [131-133]. More energetic collisions yielded larger electron densities in the reactor per unit time, and combined effects of these phenomena resulted in the observed increases in reaction products in the reactor effluent. Although the concentration of produced CO was stoichiometric, i.e., carbon species were conserved, the concentration of molecular oxygen was found to be lower than the stoichiometric concentrations as some O₂ was converted into ozone in all cases.

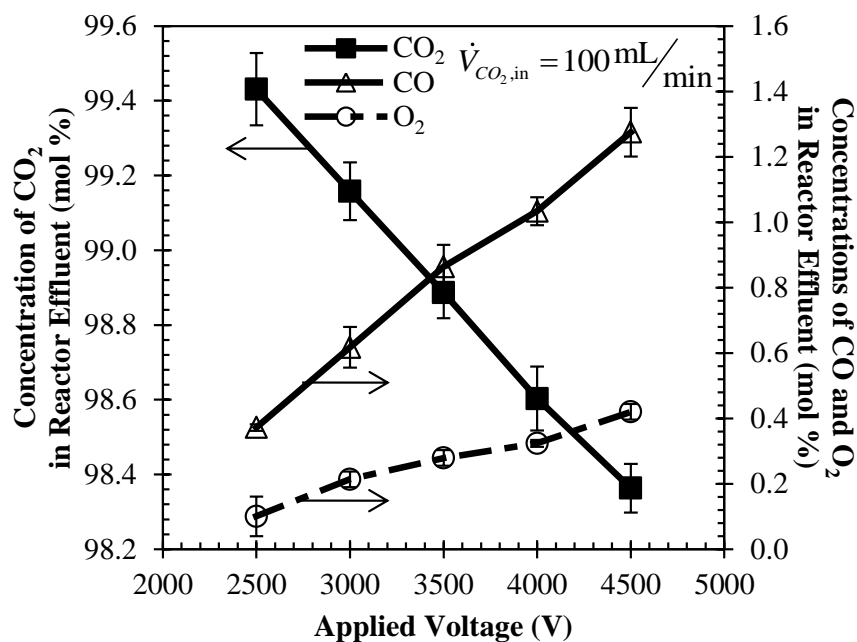


Figure 5.2. Concentrations of CO₂, O₂ and CO in the reactor effluent as a function of applied voltage at a flow rate of 100 mL/min.

Moreover, Figure 5.3 shows the energy density and the self-pulsing frequency in the MHCD reactor as a function of applied voltage when the inlet flow rate was 100 mL/min. The energy density refers to the ratio of the average power consumed by the reactor to the volumetric flow rate of CO₂ in reactor influent. The figure shows that energy density in the reactor increased from 0.5 to 1.5 J/cm³ as applied voltage increased from 2.5 to 4.5 kV. Similarly, the self-pulsing frequency increased from 12 to 47 kHz for the same voltage range. The results for energy density also suggested higher electron density and energies with increasing applied voltage. Additionally, changes in frequency can be attributed to the electron density in the reactor. As the applied voltage increases electrons accelerate more and become more energetic. More energetic electrons increase the ionization rate through collisions, and give rise to larger electron densities in the reactor making the gas phase more conductive. Finally, the rate of charge transfer across

the plasma increases requiring less time for the discharge to occur, thus, increasing the self-pulsing frequency.

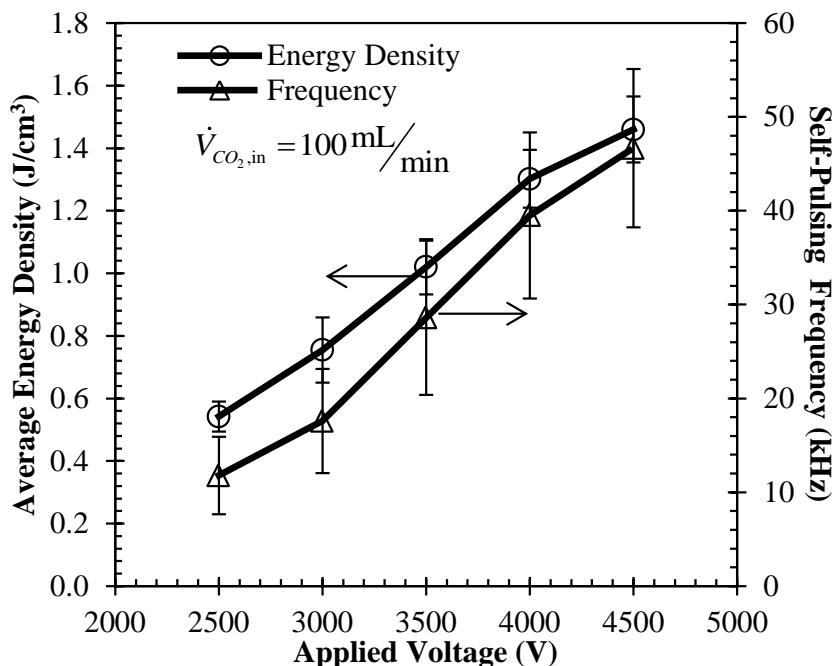


Figure 5.3. Average energy density and self-pulsing frequency as a function of applied voltage at a flow rate of 100 mL/min.

In addition, Figure 5.4 shows the electrical-to-chemical energy conversion efficiency and CO₂-to-CO conversion yield as a function of applied voltage when the inlet volumetric flow rate was 100 mL/min. The figure shows that the electrical-to-chemical energy conversion efficiency increased from 8% to about 10% from 2.5 to 3 kV, and it stayed fairly constant at higher applied voltages. Although the simulation results shown in Appendix D assuming uniform electric field in the discharge hole overestimated the conversion yield, they were able to capture the increasing trend of yield with applied voltage. Additionally, the conversion yield increased by about 2.4 times

over the applied voltage range. This indicates that a significantly larger increase in CO production rate compensated for the majority of increase in power consumption resulting in a fairly stable energy conversion efficiency of about 10%. The energy lost to inelastic collisions that did not dissociate the gas and to the heating of the gas. These mechanisms decreased the energy conversion efficiency.

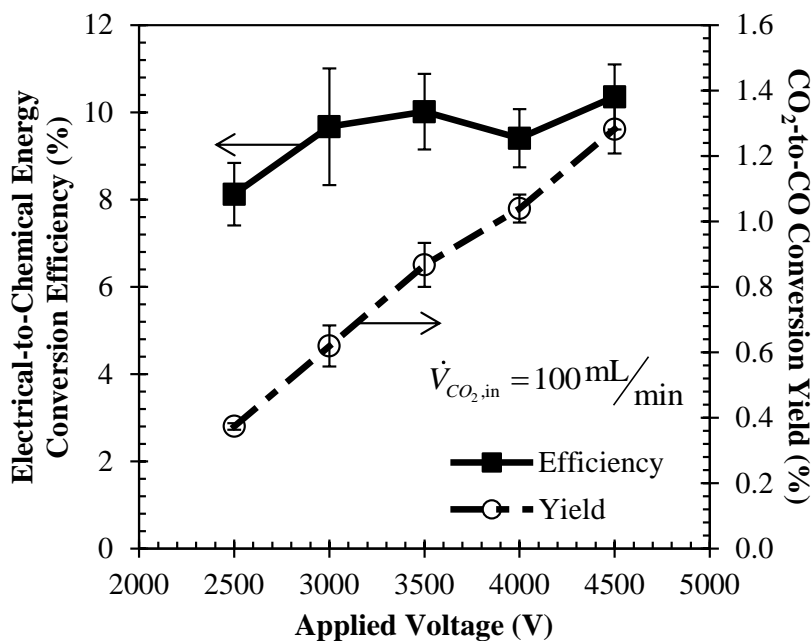


Figure 5.4. Electrical-to-chemical energy conversion efficiency and CO₂-to-CO conversion yield as a function of applied voltage at a flow rate of 100 mL/min.

5.3.2 Effects of Flow Rate

Secondly, we investigated the effects of gas flow rate on the performance of the MHCD reactor in dissociating CO₂. For this, flow rate of the gas was varied from 10 to 800 mL/min at 25°C and 1 atm containing CO₂ at a molar concentration of 99.5% while the reactor was operated at 4.5 kV. Figure 5.5 shows the concentrations of CO₂, CO and O₂ in the reactor effluent as functions of the inlet flow rate. It indicates that as the flow

rate increased from 10 to 800 mL/min, CO₂ concentration in the effluent increased from 86.3% to 99.4%, whereas the concentrations of CO and O₂ decreased linearly on a logarithmic scale from 9.9% to 0.38% and from 3.48% to 0.09%, respectively. This decrease in dissociation rate of CO₂ was attributed to the decrease in CO₂ residence time in the reactor with increasing flow rate. The residence time of CO₂ in the reactor was estimated as the ratio of the discharge hole volume to the volumetric flow rate. Residence times in this study were about six orders of magnitude larger than the timescales associated with CO₂ dissociation, which can be estimated on the order of picoseconds based on the collision frequencies [75]. Thus, the flow rate is not expected to significantly affect the collision frequencies at a given charge density. However, note that the residence times were comparable to the times between consecutive discharges. Thus, at higher flow rates, the charges, especially the heavy charges (i.e., protons and negative ions), are expected to be forced out of the reactor when the voltage difference between the electrodes was low after each discharge as shown in Figure 5.1. Since ionization is mainly followed by dissociation, less dissociation is expected to occur at lower charge densities. Thus, in our experiments less dissociation was observed at higher flow rates as shown in Figure 5.5.

Figure 5.6 shows the average energy density by the reactor as the inlet flow rate was varied from 10 to 800 mL/min at an applied voltage of 4.5 kV. It indicates that the energy density decreased linearly with the flow rate on a logarithmic scale from 15.2 to 0.2 J/cm³ in the specified flow rate range. Figure 5.6 also shows that the self-pulsing frequency decreased logarithmically by about 35% from 50 to 33 kHz in the same flow rate range. At larger flow rates, lower charge densities were expected as mentioned above. Higher charge densities would yield more energy dissipation due to inelastic

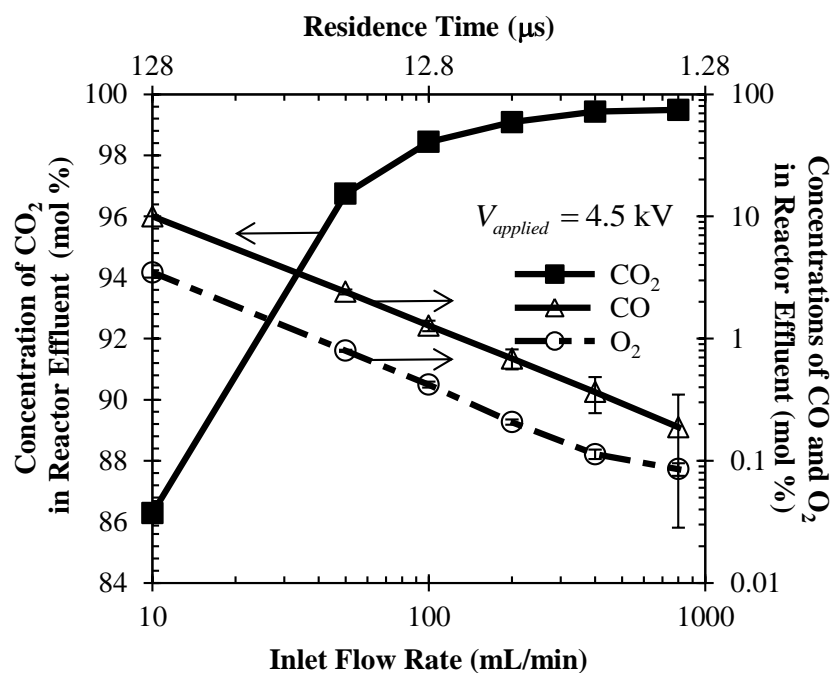


Figure 5.5. Concentrations of CO₂, O₂ and CO in the reactor effluent as a function of inlet flow rate at an applied voltage of 4.5 kV.

collisions such as recombination, ion-ion collision, etc. Thus, the decrease in energy density at larger flow rate can be attributed to the lower charge density in the reactor. Similarly, as mentioned above, the self-pulsing frequency is related to the charge density. For that reason, the frequency decreased due to lower electron density as flow rate increases. Additionally, as mentioned above, the observed frequencies and the residence times were on the same order of magnitude. This result suggests that the plasma was expected to be more neutral after the discharges at higher flow rates.

Figure 5.7 shows the electrical-to-chemical energy conversion efficiency and CO₂-to-CO conversion yield as functions of the inlet flow rate of CO₂. The figure indicated that energy conversion efficiency logarithmically increased by about 28% from 8.2% to 10.5% as the inlet flow rate increased from 10 to 800 mL/min. On the other

hand, the CO₂-to-CO conversion yield decreased linearly on a logarithmic scale from 10.5% to 0.38% for the same flow rate range. Using the obtained trend for conversion yield, the yield could be expected to reach as high as 87% at an inlet flow rate of 1 mL/min which corresponds to a residence time of 1.28 ms. The increase in energy conversion efficiency showed that the number of moles of generated CO increased with increasing flow rate despite the concentration of CO in the reactor effluent was lower. The power consumption did not affect the energy conversion efficiency, as the power consumption stayed fairly constant with flow rate.

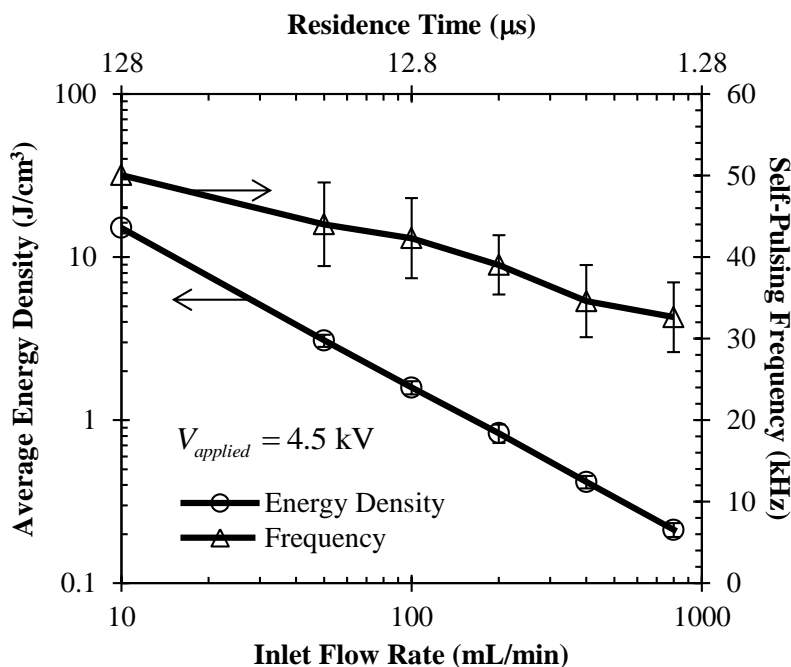


Figure 5.6. Average energy density and frequency of self-pulsing discharges as a function of inlet flow rate at an applied voltage of 4.5 kV.

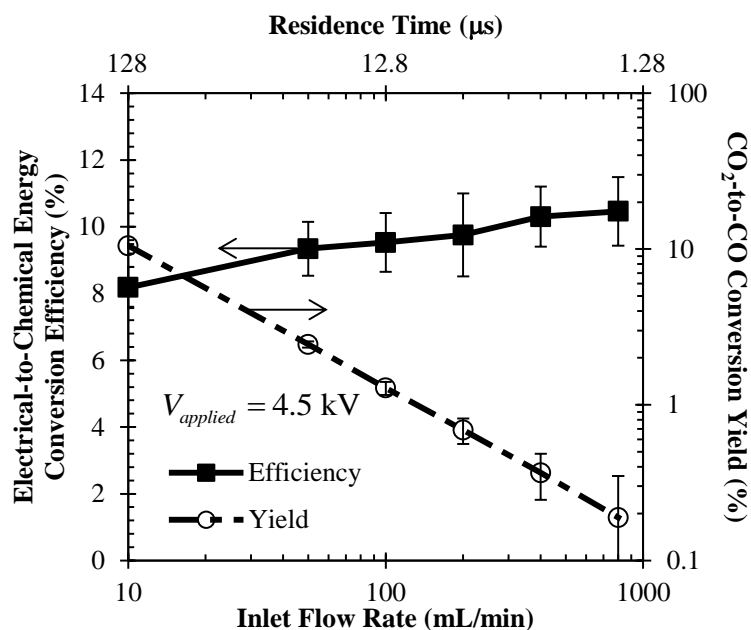


Figure 5.7. Power efficiency and CO₂-to-CO conversion yield as a function of inlet flow rate at an applied voltage of 4.5 kV.

5.3.3 Effects of Concentration

Lastly, we investigated the effects of CO₂ mole fraction in the influent on the performance of the MHCD reactor for dissociating CO₂. Experiments were conducted providing a varying mole fraction of CO₂ in argon from 9.95% to 89.6% at a total flow rate of 100 mL/min and an applied voltage of 4.5 kV. Figure 5.8 shows the concentrations of CO₂, CO and O₂ in the reactor effluent as functions of CO₂ mole fraction in influent gas mixture. The figure indicates that the effluent concentration of CO₂ increased fairly linearly with increasing influent concentration, whereas those of CO and O₂ increased and approached to about 1.7% and 0.5%, respectively, for 89.6% CO₂. Decreasing the CO₂ mole fraction in influent by 9 times decreased the CO and O₂ concentrations by only 2.6 and 2.2 times, respectively. Thus, dilution of CO₂ with argon suggested a significant improvement of the CO₂ dissociation using a carrier gas. As

Paschen curves suggested, the breakdown voltage of argon was smaller than that of CO₂, and argon would yield larger secondary electron emission from cathode due to its higher ionization energy [25, 75]. Therefore, diluting CO₂ with argon would result with higher electron density in the reactor than pure CO₂. The liberated electrons would yield more collisions; thus, increasing the dissociation of CO₂ through collisions.

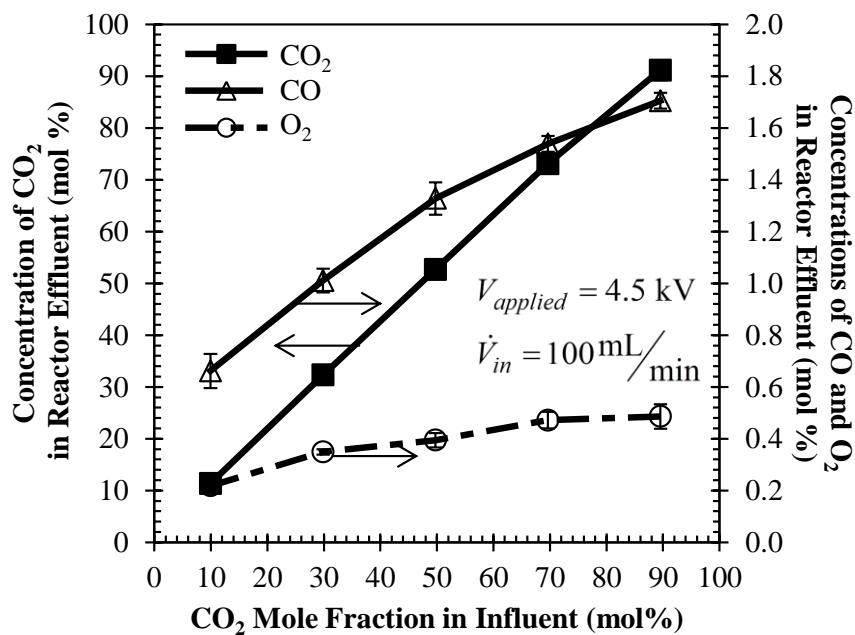


Figure 5.8. Concentrations of CO₂, O₂ and CO in the reactor effluent as a function of inlet CO₂ concentration at a total inlet flow rate of 100 mL/min and an applied voltage of 4.5 kV.

Moreover, Figure 5.9 shows the average energy density and self-pulsing frequency as functions of CO₂ mole fraction in influent. The average energy density decreased from 9.7 to 1.6 J/cm³ as CO₂ mole fraction in influent increased from 9.95% to 89.6%. The observed energy density approached to about 1.5 J/cm³ which was consistent with the energy density of 99.5 mol% CO₂ shown in Figure 5.6 and Figure 5.9. Also, the

figure indicates that the self-pulsing frequency decreased from 72 to 35 kHz for as the CO₂ mole fraction increased. These observations further corroborated that presence of argon increased the electron density and energies in the reactor, leading to increase in energy density and frequency.

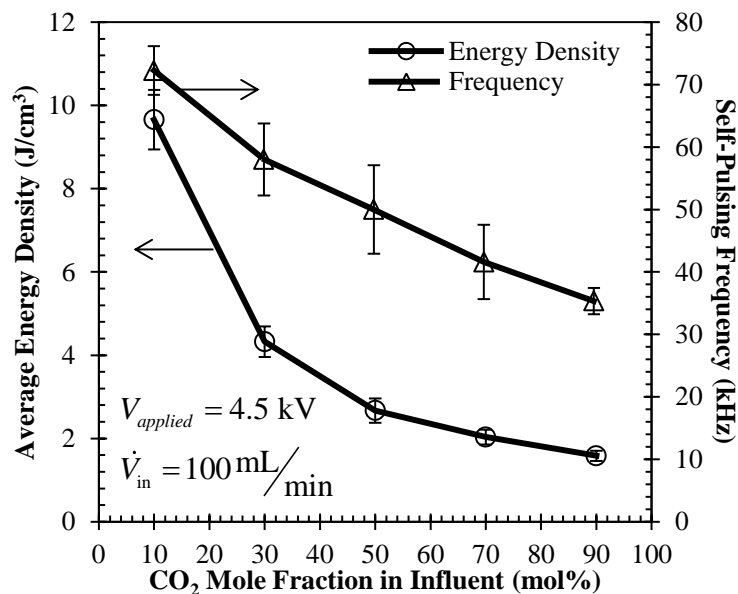


Figure 5.9. Average energy density and self-pulsing frequency as a function of inlet CO₂ concentration at a total inlet flow rate of 100 mL/min and an applied voltage of 4.5 kV.

Finally, Figure 5.10 shows the electrical-to-chemical energy conversion efficiency and the CO₂-to-CO conversion yield as functions of CO₂ mole fraction in influent. It shows that the energy conversion efficiency displayed a fairly linear increase from 6.8% to 13.7% as CO₂ mole fraction increased from 9.95% to 89.6%. However, the conversion yield decreased from 5.6% to 1.8% for the same range. These results suggested that the increase in yield did not compensate for the larger power consumption due to the presence of the carrier gas, which in return the energy conversion efficiency decreased.

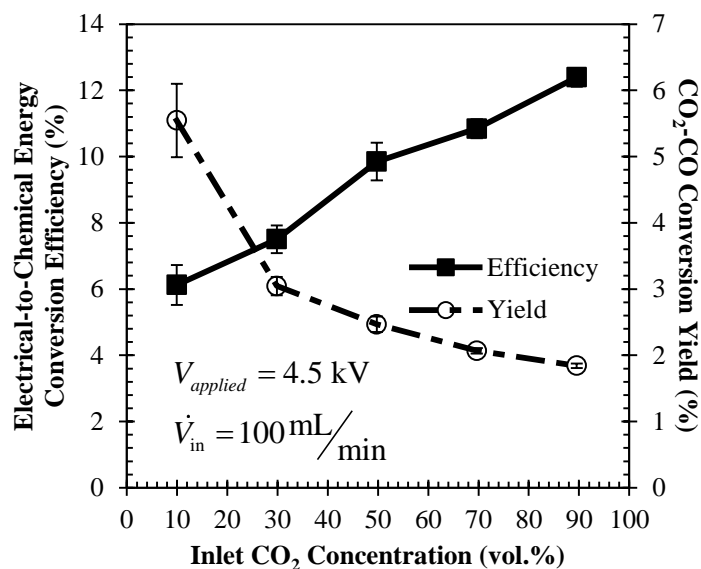


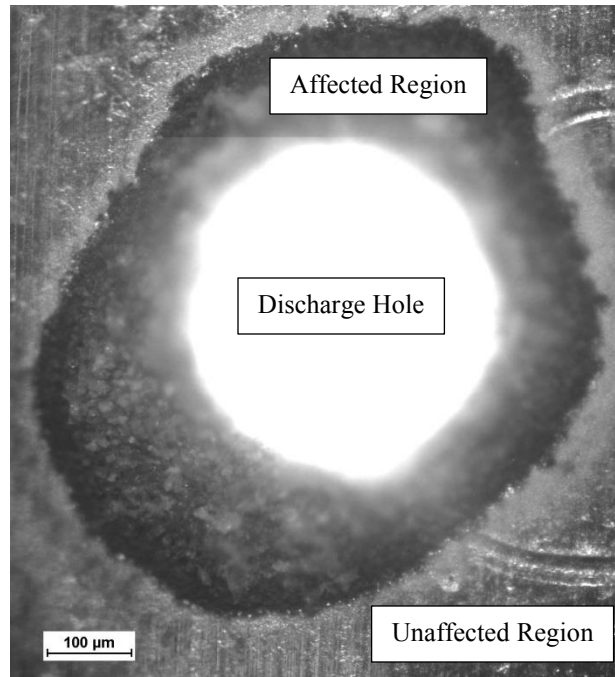
Figure 5.10. Electrical-to-chemical energy conversion efficiency and CO₂-to-CO conversion yield as a function of inlet CO₂ concentration at a total inlet flow rate of 100 mL/min and an applied voltage of 4.5 kV.

5.3.4 Assessment of Electrode Degradation

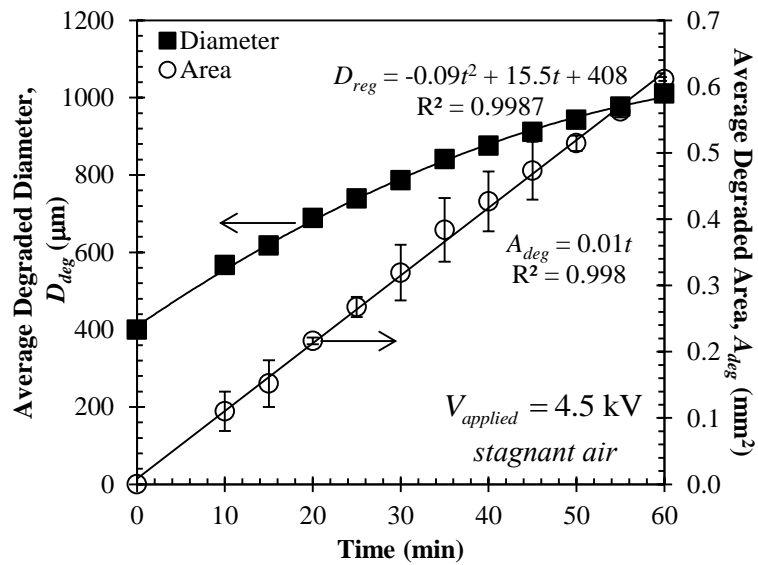
Moreover, during the operation of the reactor, degradation of the electrodes was observed, especially on the anode side of the reactor from which the electrodes were discharged. As the reactor was operated in self-pulsing regime, the plasma expanded over the electrode around the hole from which charges were discharged in less than 10 ns. As the plasma expanded over the electrode, electrode degraded due to heating caused by ion sputtering on the electrode surface. Therefore, as the charge density and ion energies increased, higher electrode degradation was expected. In order to quantify the electrode degradation, the reactor was operated at an applied voltage of 4.5 kV in stagnant air at atmospheric pressure. An optical image of the reactor was taken at every 5 minutes using a CCD camera (Nikon DS-Qi1) and an inverted microscope (Nikon Eclipse Ti-E). The images were analyzed in microscope imaging software (Nikon NIS-Elements) to

determine the degraded electrode area. Figure 5.11a shows the microscope image of the reactor, illustrating the affected electrode region around the discharge hole after 25 minutes of operation at an applied voltage of 4.5 kV. Additionally, Figure 5.11b shows the affected electrode diameter, which was measured from the center of the discharge hole, and degraded electrode area around the hole as a function of time. The figure shows that the diameter of the affected region increased quadratically with time. Additionally, affected area on electrode linearly increased with time at a rate of about 0.01 mm²/min. This rate is expected to be the maximum degradation rate of this study as at lower applied voltages or with gas flow the current was also lower and degradation rate would be lower. Moreover, in dissociation studies, each reactor was not used more than about 30 minutes, and each experimental case were repeated with three different reactors. The error bars shown in figures also reflect deviation due to electrode degradation.

Additionally, an endurance test was performed on the reactor under the same conditions as the degradation test. The reactor was successfully operated in the self-pulsing regime for about 27 hours after which the current suddenly decreased by about two orders of magnitude. This decrease in current signified a change in the operating regime of the reactor which no longer was in the self-pulsing regime. As mentioned above, lower degradation rates were expected at lower voltages or with gas flow which would yield to longer operation times of the reactor.



(a)



(b)

Figure 5.11. (a) Microscope image of the reactor after 25 minutes of operation showing the affected electrode region around the discharge hole, and (b) degraded electrode diameter and area as a function of time for MHCD reactor operated in stagnant air at an applied voltage of 4.5 kV.

5.3.5 Implications on the Operation of MHCD Reactor for CO₂ Dissociation

In this study, the maximum electrical-to-chemical energy conversion efficiency was found to be 13.7% when mole fraction of CO₂ was 89.6% in argon at an applied voltage of 4.5 kV and a total inlet flow rate of 100 mL/min. The trends in the results suggested that larger applied voltages and smaller residence times increased the energy conversion efficiency of the reactor. Moreover, it was observed that introducing small amounts of argon at low concentrations also increased the energy conversion efficiency.

On the other hand, higher conversion yields were achieved at larger applied voltages, longer residence times and higher concentrations of argon. The maximum CO₂-to-CO conversion yield was 10.5% at a flow rate of 10 mL/min, applied voltage of 4.5 kV and a CO₂ concentration of 99.5%. Extrapolation of the trends indicated that yields as large as 87% could be achieved if the flow rate was reduced to 1 mL/min which corresponds to a residence time of 1.28 ms.

The results indicated that it was not possible to maximize the energy conversion efficiency and the conversion yield at the same time as these were competing objectives with each other. Although counter intuitive, this result can be explained by noting that increasing yield requires high electron density and energy in the plasma which result in large energy density in the reactor. Large energy density corresponds to large power consumption, and thus, decreases the overall energy conversion efficiency of the reactor.

Finally, we compared the observed performance of the MHCD reactor to other competing technologies for converting and utilizing CO₂. When compared with electrochemical reactors, both systems featured similar CO₂ dissociation rates on the order of 10 cm³/min [134]. However, CO₂ needs to be dissolved in electrolyte in electrochemical systems and saturating electrolyte requires a few hours [134].

Additionally, solubility of gas in electrolyte poses another limitation for the electrochemical reactors. Moreover, although 100% yields were possible with electrochemical reduction, it was reported that the efficiency of the device quickly deteriorated and operation ceased after 5 hours when Cu electrodes were used [135]. As an alternative way for dissociating CO₂, photocatalytic reactors showed lower energy conversion efficiencies than MHCD reactors. Deguchi *et al.* [136] used a photocatalytic reactor with AlGa_{0.3}N/GaN and Cu electrodes in 3.0M KCl solution and showed an energy conversion efficiency of 0.13%. CO₂ was also considered as a feedstock for producing solar fuels in solar thermochemical reactors [137]. These systems featured very high temperatures in excess of 1500°C, during operation and yielded only solar to fuel conversion efficiencies of 0.7% to 0.8% [137]. Considering the use of 20% efficient photovoltaics in conjunction with the MHCD, solar to fuel conversion efficiencies of 2.7% are possible based on the results reported in this study. Thus, the MHCD plasma reactor featured numerous advantages over other methods and processes for dissociating CO₂ based on its simplicity, relatively large energy conversion efficiency and conversion yield.

5.4 CHAPTER SUMMARY

This chapter experimentally demonstrated the dissociation of carbon dioxide using a microhollow cathode discharge (MHCD) plasma reactor in the self-pulsing regime at 1 atm for the first time. Moreover, the chapter reported the CO₂ dissociation performance of the MHCD reactor as a function of key operational parameters. These included the applied voltage, the gas flow rate, and the concentration of CO₂ in the influent gas mixture. The performance of the reactor was evaluated based on the effluent composition, power consumption, electrical-to-chemical energy conversion efficiency

and CO₂-to-CO conversion yield. The results showed that increasing applied voltage increased both conversion efficiency and yield, whereas efficiency and yield were competing as flow rate and CO₂ concentration in the influent were varied. The maximum energy conversion efficiency and yield achieved experimentally in this study were 13.7% and 10.5%, respectively.

Chapter 6

Dissociation of Water-Saturated Carbon Dioxide using MHCD Plasma Reactor

This chapter presents an experimental study that reports production of hydrogen and synthesis gas (syngas) from water vapor-saturated argon and carbon dioxide in a microhollow cathode discharge (MHCD) plasma reactor at atmospheric pressure. The MHCD reactor was fed with H₂O-saturated Ar or CO₂ at flow rates of 10, 50 and 100 mL/min and an applied voltage of 4.5 kV_{DC}. The current through and voltage across the reactor were measured for each experimental case, and gas compositions at the reactor effluent were analyzed in a gas chromatograph.

6.1 INTRODUCTION

Syngas is mainly produced through CO₂ reforming of CH₄ [10, 36, 138, 139]. Although this process utilizes CO₂ and reduces its negative effect on the global warming, it dissociates CH₄ which already has a high heating value as a fuel. This reforming process also requires metal catalysts which are expensive, and these catalysts decompose or deactivate as a result of carbon deposition on their surfaces [10, 36, 138, 139]. An alternative path to produce syngas is through the use of plasma [8-10]. Plasma processes do not require catalysts and effectively couples the energy input to the molecules for dissociation when compared to conventional processes [6, 25-27]. Additionally, the non-thermal plasma reactors can operate at about room temperatures, so that these reactors do not need to withstand high temperatures. Therefore, the use of non-thermal plasma reactors would reduce the material and manufacturing cost of the reactor. One of the non-thermal plasma reactors that can be used to dissociate gases is microhollow cathode

discharge (MHCD) reactor which consists of two hollow metal electrodes that are separated by a dielectric material [33, 140]. This reactor can be operated with direct (DC), alternating (AC) and pulsed excitation. However, in order to generate stable non-thermal plasma, the reactor needs to be operated in its self-pulsing regime at which current and voltage of the discharges inherently oscillate [31-33]. In this regime, voltage decreases with increasing current as the regime is characterized with a negative differential impedance [31-33]. This chapter focused on MHCD plasma reactors operated in self-pulsing regime to dissociate humidified argon and carbon dioxide.

This chapter reports the hydrogen and syngas generation through dissociation of H₂O-saturated Ar and CO₂ in a MHCD plasma reactor at atmospheric pressure. A prototype MHCD reactor was used to dissociate saturated gases as the inlet volumetric flow rate varied. Voltage and current characteristics of the reactor were reported and used to calculate the power consumption of the reactor for all the experimental cases. The results are presented in terms of gas compositions at the reactor effluent, conversion yield and electrical-to-chemical energy conversion efficiency.

6.2 EXPERIMENTAL PARAMETERS

The reactor and experimental setup used in this part of the study were given in Sections 3.2 and 3.3. The aluminum electrodes were separated by a mica plate with a thickness of 150 μm as a dielectric material. The discharge hole was about 400 μm in diameter. Figure 3.2 shows the experimental setup used in this part. Carbon dioxide with 99.5% purity (Matheson Tri-Gas) and argon with 99.998% purity (Airgas) were fed to the H₂O-saturator through flow rate controllers. Relative humidity controller (Walz, KF-18/2B) and the CO₂/H₂O analyzer (LI-COR, LI-840A) were used to verify that the gas streams were saturated with water. Then, the H₂O-saturated gas stream was fed to the

flow chamber in which the MHCD reactor was placed. The gas samples were taken at the exit of the flow chamber, and their compositions were analyzed in a gas chromatograph (Shimadzu GC-2014).

Based on the atmospheric pressure and the size of the thickness of dielectric material used in this study, the breakdown electric field for pure CO₂, Ar and H₂O were estimated as 2.1, 1.0 and 1.6 kV, respectively, using the Townsend breakdown mechanism. As mentioned before, the gas needs to be subjected to a voltage that is greater than the breakdown voltage to breakdown the gas and generate microdischarges. Based on the estimated breakdown voltage values and the upper voltage limit of the power supply, DC voltage was chosen as 4.5 kV, and based on the flow rate controllers the flow rate of the fed gas was chosen as 10, 50 and 100 mL/min in this part of the study. Each parameter combination was run 6 times as independent experiments, and the error bars shown in this chapter reflect the standard deviation of these independent experiments.

6.3 RESULTS AND DISCUSSION

6.3.1 Voltage and Current Characteristics of Dissociation Process

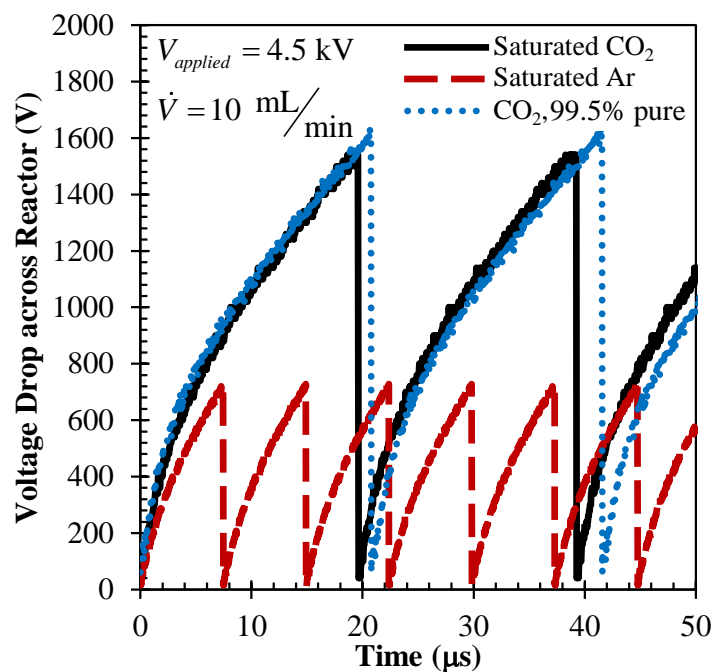
This section shows the results of and discussion on the current and voltage characteristics of the reactor as H₂O-saturated Ar and CO₂ provided to the MHCD reactor at different flow rates. These characteristics were compared with those of 99.5%-pure CO₂. The current and voltage characteristics guide towards selecting the power supply and enhancing the conversion yield and efficiency. Figure 6.1 shows the experimentally measured voltage across and current through the MHCD reactor as functions of time at a flow rate of 10 mL/min. Results with other flow rates showed similar behavior, and they

were not repeated here for brevity. This figure clearly illustrates that there are distinct operating regimes of charging and discharging. Figure 6.1a shows that voltage increased in charging regime as electrons were accumulated at the cathode, and decreased sharply when the voltage reached the breakdown voltage of the gas indicating the discharge. As the voltage decreased below the threshold value due to discharge, the electron density in the reactor was not high enough to sustain the discharge and the charging regime started again. This charging-discharging scheme is referred as the self-pulsing regime of MHCD reactor. The maximum voltages in Figure 6.1a were equal to the breakdown voltages of corresponding gases. As shown in Figure 6.1a, breakdown voltage of H₂O is greater than Ar, but lower than CO₂. Accordingly, when Ar and CO₂ were saturated with H₂O, the breakdown voltages of Ar and CO₂ got closer to that of H₂O based on the gas concentrations. However, the observed breakdown voltages were slightly lower than those estimated from Paschen curves which assume uniform electric field and no charge between the electrodes initially. The experimental results showed that the minimum voltage for each gas was non-zero indicating that a number of charges were present in the reactor after the discharge. These charges yielded lower breakdown values than those estimated from Paschen curve as discussed in Chapter 4. As a result, the maximum voltages were measured about 1640 V for 99.5%-pure CO₂, 1540 V for saturated CO₂ and 730 V for saturated Ar.

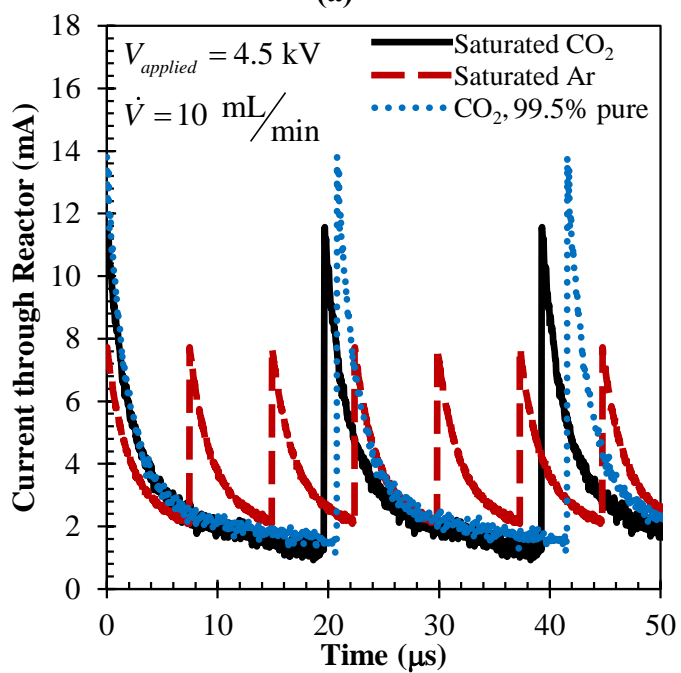
As Figure 6.1b shows, the current through the reactor exponentially decayed with time after the discharge and abruptly increased when discharge occurred. The results showed that the maximum currents were about 11.6 and 7.8 mA for saturated CO₂ and Ar, respectively, at a flow rate of 10 mL/min. The maximum currents were attributed to the maximum number of charges accumulated at the cathode. These charges were

abruptly discharged when the voltage reached breakdown threshold resulting in a peak in current. Therefore, gases with higher breakdown voltages featured higher peak currents. Moreover, saturated Ar showed the highest minimum current of about 1.9 mA, whereas saturated CO₂ showed the lowest minimum current of about 1.1 mA. The minimum currents could be associated with the number of charges in the reactor just before the discharge. In high pressure plasma systems, charges are mainly lost due to binary and three-body collisions for electronegative gases [75]. Ar as a noble gas is not electronegative; thus, charge loss through collisions in Ar should be less than that in CO₂. Therefore, cases with Ar had higher charge density in the reactor which should also have favored the secondary electron emission from the cathode [84]. Additionally, Ar has higher ionization energy which also favors the secondary electron emission. Overall, cases with saturated Ar were expected to have higher ion and electron densities which yielded higher currents in the charging regime. Furthermore, as the water vapor content in saturated CO₂ was about 3.2%, the current for the case with saturated CO₂ did not significantly deviate from the case with 99.5%-pure CO₂.

Moreover, Figure 6.1 illustrates the self-pulsing frequencies of the reactor presenting charging-discharging period. As mentioned above, breakdown voltages indicated the number of charges required to be accumulated at cathode for discharge. Therefore, saturated CO₂ having higher breakdown voltage than saturated Ar required longer time to accumulate required number of charges for its discharge. So, saturated CO₂ showed smaller self-pulsing frequency than saturated Ar which featured higher frequency than 99.5%-pure CO₂.



(a)



(b)

Figure 6.1. (a) Voltage drop across and (b) current through the reactor as functions of time for H_2O -saturated CO_2 , H_2O -saturated Ar and 99.5%-pure CO_2 at a flow rate of 10 mL/min and an applied voltage of 4.5 kV.

Figure 6.2 shows the average voltage versus average current for (i) H₂O-saturated CO₂, (ii) H₂O-saturated Ar and (iii) 99.5%-pure CO₂ at volumetric flow rates of 10, 50 and 100 mL/min and an applied voltage of 4.5 kV. This figure illustrates that average voltage decreased almost linearly with increasing average current confirming that the reactor had negative differential impedance and was operated in the self-pulsing regime. Figure 6.2 also shows that voltage of cases with saturated Ar was lower by about 1.4 times than that of saturated CO₂, whereas current of cases with saturated Ar was about 22% higher than that of saturated CO₂ at all flow rates. Lower voltage for cases with saturated Ar was mainly due to lower breakdown voltage of Ar with respect to CO₂ and H₂O. Moreover, higher current for cases with saturated Ar can be related to higher charge density in the reactor as discussed above. Additionally, as mentioned above, saturated CO₂ required less number of charges for discharges with respect to 99.5%-pure CO₂ due to presence of H₂O which has lower ionization energy than CO₂. Therefore, as shown in Figure 6.1, saturated CO₂ showed smaller maximum and minimum currents than 99.5%-pure CO₂. Therefore, average current of saturated CO₂ was lower than that of 99.5%-pure CO₂. Based on the negative differential impedance of the self-pulsing regime of MHCD reactor, average voltage of saturated CO₂ was higher than that of 99.5%-pure CO₂.

Figure 6.2 also illustrates that the average voltage and current were weak functions of the volumetric flow rate. For all gases, increasing the flow rate from 10 to 100 mL/min decreased the average current by about 4% and increased the average voltage by 12%. Higher flow rates would yield lower charge density in the reactor as more charges were carried out the reactor at higher flow rates, especially after the discharge when the electric field was weak between the electrodes. Therefore, lower charge density resulted in lower current and higher voltage in the self-pulsing regime.

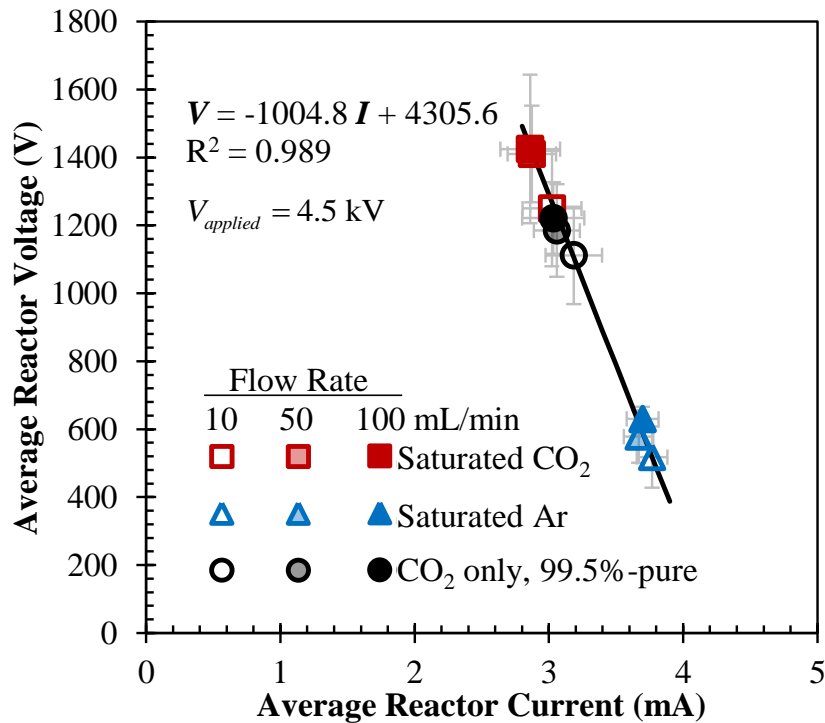


Figure 6.2. Time-averaged discharge voltage versus time-averaged discharge current of the experimental cases at flow rates of 10, 50 and 100 mL/min and an applied voltage of 4.5 kV.

6.3.2 H₂ and CO Generation from Saturated Ar and CO₂

To analyze the performance of proposed MHCD reactor for hydrogen production, H₂O-saturated argon was fed to the reactor. Figure 6.3a shows the concentration of gases, namely H₂O, H₂ and O₂, at the reactor effluent at the inlet flow rates of 10, 50 and 100 mL/min. Based on these results, as the inlet flow rate increased from 10 to 100 mL/min, the concentration of H₂ decreased from 0.9% to 0.2%. Correspondingly, H₂O concentration increased from 2.2 to 2.9% for the same flow rate range. Note that stoichiometric balance was met for hydrogen atoms, but not the oxygen atoms since some of oxygen from H₂O was converted to ozone rather than O₂. As previously mentioned,

higher charge density was expected in the reactor at smaller flow rates as less charges were forced out of the reactor [141]. Thus, the reaction rates increased with increasing charge density, and higher concentration of H₂ was achieved at the reactor effluent with decreasing flow rate.

In another set of experiments, H₂O-saturated CO₂ was fed to analyze H₂ and CO production in the proposed MHCD reactor. Figure 6.3b shows the concentration of gases in the reactor effluent after the dissociation process as the flow rate was varied. The results showed that concentrations of H₂ and CO in the reactor effluent were 0.2% and 13.4%, respectively, at the flow rate of 10 mL/min. As the flow rate increased to 100 mL/min, the concentrations of H₂ and CO in effluent decreased to 0.02% and 2.02%, respectively. Thus, increasing the flow rate decreased the dissociation of H₂O and CO₂ as in the case with saturated Ar.

When H₂ production from saturated CO₂ and Ar was compared, it was observed that H₂ production from saturated Ar was about 6 times higher than that from saturated CO₂ at the flow rate of 10 mL/min. Although the ionization energy of Ar is larger than CO₂, electron density in the case with saturated Ar should be higher than that of saturated CO₂, as Ar was expected to have higher secondary electron emission due to higher ionization energy, and less charge losses due to recombination as mentioned above. Overall, higher electron density enhanced gas dissociation in the reactor, and higher H₂ concentrations were observed for saturated Ar than saturated CO₂.

Based on the concentrations at the reactor influent and effluent, H₂ and CO conversion yields were calculated for saturated Ar and saturated CO₂. Figure 6.4a shows the conversion yield values at the inlet flow rates of 10, 50 and 100 mL/min. The results

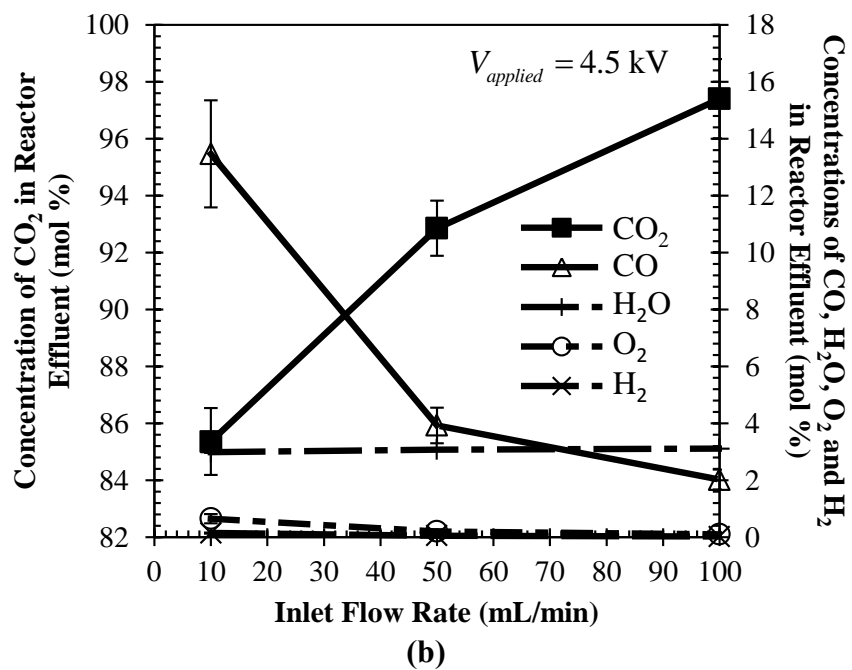
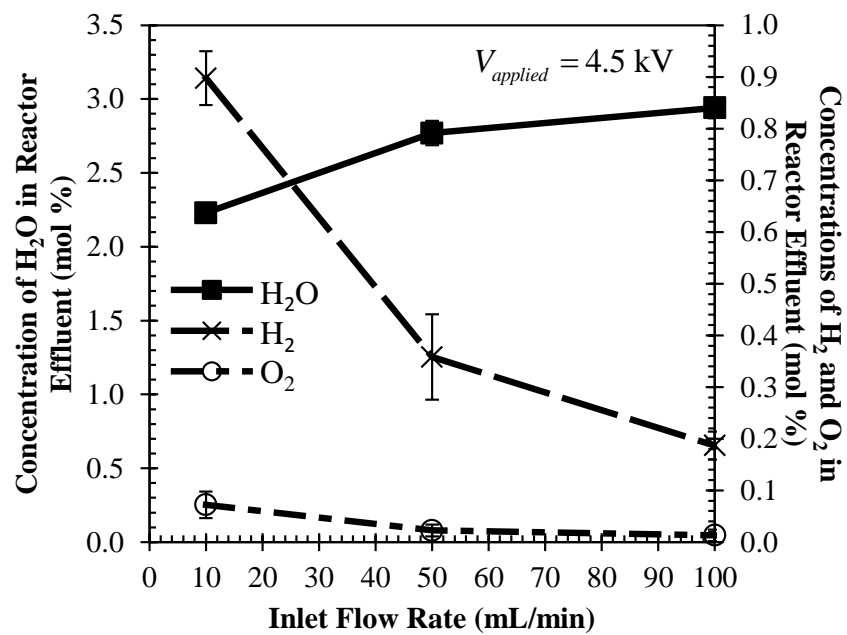
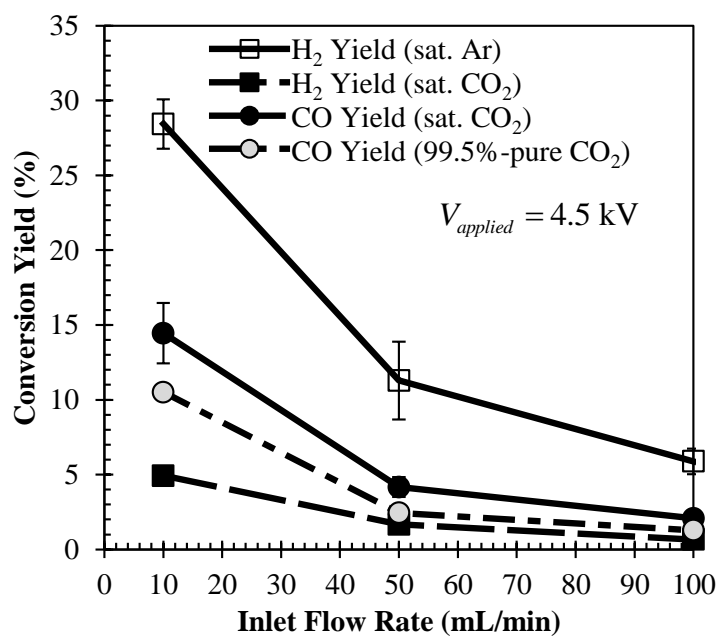


Figure 6.3. Concentrations of gases in the reactor effluent as functions of inlet flow rate for (a) H₂O-saturated Ar, and (b) H₂O-saturated CO₂.

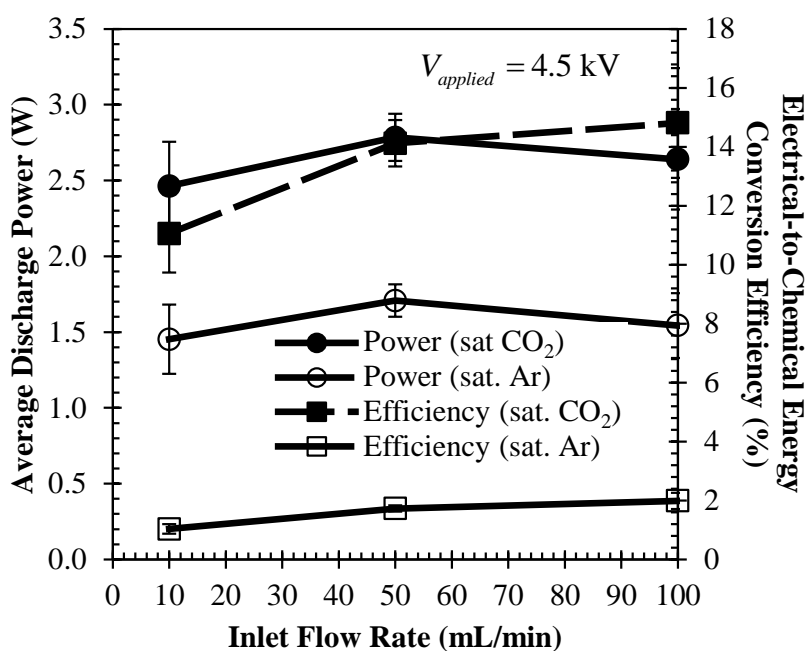
showed that at 10 mL/min, H₂ yields were 28.4% for saturated Ar and 4.9% for saturated CO₂. At the same flow rate, CO yields were about 14.5% for saturated CO₂ and 10.5% for 99.5%-pure CO₂. So, the presence of H₂O in CO₂ increased the CO yield by about 38% at the flow rate of 10 mL/min. This result suggested that electrons due to ionization of H₂O, which has lower ionization energy than CO₂, contributed to CO₂ dissociation rather than H₂O dissociation. This should be related to high concentration of CO₂ with respect to H₂O in the reactor, so that the probability of electrons, which were liberated due to ionization of H₂O and collided with CO₂ molecules, was higher than that with H₂O molecules at a given flow rate.

As the flow rate increased from 10 to 100 mL/min, H₂ yield decreased from 28.4% to 5.9% for saturated Ar and from 4.9% to 0.7% for saturated CO₂ cases as shown in Figure 6.4a. Lower conversion yields at higher flow rates were attributed to lower charge densities as mentioned above. Additionally, using Ar as carrier gas improved H₂O-to-H₂ yield about 6 times at 10 mL/min and 8 times at 100 mL/min when compared to CO₂. As a result, diluting the gas with an inert gas enhanced the dissociation and resulted in higher conversion yield.

Finally, Figure 6.4b shows time-averaged power requirement of the reactor and electrical-to-chemical energy conversion efficiency of the same cases. Average power requirements were independent of flow rate and about 1.6 and 2.8 W for saturated Ar and CO₂, respectively. Power requirement of each case was related to the required number of charges for its discharge. This requirement also included the power dissipation due to binary and three-body collisions which decreased the charge density in the reactor. As saturated Ar required fewer charges than saturated CO₂, as shown in Figure 6.1, power



(a)



(b)

Figure 6.4. (a) Conversion yield, (b) average discharge power and energy conversion efficiency as functions of inlet flow rate.

requirement for saturated Ar was lower. Moreover, Figure 6.4b shows that the energy conversion efficiency was 2.0% for saturated Ar at the flow rate of 100 mL/min. Low efficiency for saturated Ar suggested that the power input was lost to ionize Ar rather than to dissociate H₂O which was expected due to low concentration of H₂O in saturated Ar. Moreover, saturating CO₂ with H₂O increased the conversion efficiency from 9.5% to 14.8% at 100 mL/min. Higher energy conversion efficiency with the presence of H₂O was attributed to higher CO₂-to-CO conversion yield as discussed above. Additionally, energy conversion efficiency decreased with decreasing flow rate, showing that the molar flow rates of H₂ and CO decreased, although their concentrations were higher at the reactor effluent.

The results presented here demonstrated that it was possible to convert electrical energy to chemical energy using non-thermal plasma in a MHCD reactor. The hydrogen production yield of the reactor was promising such that about 28.4% of H₂O was converted to H₂ in saturated Ar at a flow rate of 10 mL/min. At the same flow rate, when the reactor was fed with saturated CO₂, H₂O-to-H₂ conversion yield was about 4.9% whereas CO₂-to-CO conversion yield was about 14.5%. These results showed simultaneous H₂/CO production ratio of 0.013 in molar basis from saturated CO₂. Higher H₂/CO ratios could be obtained by increasing the residence time of gases in the reactor and increasing the concentration of H₂O at the reactor influent. Alternatively, if H₂O and CO₂ were dissociated in separate reactors at appropriate flow rates, any H₂/CO ratio could be achieved with MHCD reactors. Moreover, due to compactness of the proposed MHCD reactor, it is also possible to scale up the system with multiple reactors in series to increase H₂ and CO production rate. Therefore, the proposed MHCD reactor shows a promising alternative for H₂ and CO generation.

6.4 CHAPTER SUMMARY

This study presented the hydrogen and carbon dioxide production by dissociating H₂O-saturated argon and carbon dioxide in a microhollow cathode discharge reactor (MHCD). Prototype of MHCD reactor consisted of three layers; one layer of mica as dielectric and single layers of electrode on each side of the dielectric with a through hole across these three layers. Argon or carbon dioxide was saturated with water and fed to the MHCD reactor through the humidity and temperature controller at three different flow rates at atmospheric pressure. A direct-current high voltage of 4.5 kV was applied to one of the electrodes and the other electrode was grounded. High voltage probes were used to measure voltage drop across the reactor and across a current viewing resistor to obtain discharge current. Voltage and current characteristics of each experimental case were compared. Additionally, gas compositions at the exit of the reactor were analyzed for each case in a gas chromatograph, and conversion yields, power requirement of the reactor and electrical-to-chemical energy conversion efficiencies were calculated. Based on the obtained results, the maximum hydrogen yield was about 28.4% from saturated argon whereas it was about 4.9% from saturated carbon dioxide at a flow rate of 10 mL/min. Additionally, introducing water vapor in carbon dioxide increased the CO yield from 10.5% to 14.5% at 10 mL/min. Moreover, the maximum energy conversion efficiencies of about 14.8% and 2.0% were obtained for saturated carbon dioxide and argon, respectively. The efficiency for argon was lower as some of the energy input was lost to ionizing and heating argon which enhanced the conversion yield. Overall, in this chapter, hydrogen and carbon dioxide generation from saturated gases was demonstrated using microhollow cathode discharge plasma reactor.

Chapter 7

Effects of Design Parameters on Dissociation using MHCD Plasma Reactors

This chapter reports experimental results on dissociation of carbon dioxide in a microhollow cathode discharge reactor at atmospheric conditions. Microhollow cathode discharge reactor consists of two hollow metal electrodes that are separated by a dielectric material. This part of the study focused on the effects of the thickness of the dielectric material and the size of the hole in the reactor on dissociation of carbon dioxide. The dielectric thickness was chosen as 150, 300 and 450 μm , whereas the discharge hole diameter was selected as 200, 400 and 515 μm . The results of each experimental case in this study were presented in terms of the concentration of gases at the exit of the reactor, power requirement, carbon dioxide-to-carbon monoxide conversion yield, and electrical-to-chemical energy conversion efficiency.

7.1 INTRODUCTION

This chapter focuses on CO_2 dissociation using non-thermal plasma generated by a prototype MHCD reactor. CO_2 is a greenhouse gas, widely accepted to contribute towards global temperature rise. Thus, there is an urgent need to reduce the CO_2 emissions from the use of fossil fuels and/or utilize CO_2 as a carbon source for the manufacture of fuels and chemicals. Conventionally CO_2 utilization requires high temperatures and catalysts and often the generated carbon black particles clog the conventional reactors [71, 138, 139, 142]. Alternatively, non-thermal plasma by means of MHCD reactors does not require high temperatures or catalysts, and these reactors have low cost, low power requirement and could work with different gas compositions [6, 25-27].

This study investigated the effects of dielectric thickness and hole size on CO₂ dissociation in a prototype MHCD plasma reactor at ambient pressure. Prior to this study, the effect of electrode separation was investigated mainly on the voltage requirement of plasma reactors, and the results were generalized as Paschen curves [25, 82, 83]. These curves along with their restrictions were discussed in more detail in the next section. Additionally, Lennon *et al.* [143] showed that increasing dielectric thickness decreased the capacitance of the reactor so that the frequencies of the discharges increased at a given average current through the reactor. The studies in the literature showed that the hole size did not affect the voltage requirement of MHCD reactors for plasma generation [31, 144]; however, decreasing the hole size increased the electron density in the reactor [145]. Although these studies investigated the effects of geometric parameters on voltage requirement and electron density, they did not investigate the effects on the applications, such as on gas dissociation.

To our knowledge, there is no study that has experimentally investigated the performance of a prototype MHCD plasma reactor for dissociating CO₂ at atmospheric pressure as the dielectric thickness and hole size were varied. The dissociation performance of the reactor was quantified in terms of gas concentrations in the reactor effluent, electrical-to-chemical energy conversion efficiency and CO₂-to-CO conversion yield.

7.2 EXPERIMENTAL PARAMETERS

Sections 3.2 and 3.3 present the prototype MHCD plasma reactor and the experimental setup used in this part of the study. A mica plate as a dielectric material separated the hollow aluminum electrodes. The discharge hole was featured through these three layers. In this chapter, thickness of the dielectric layer and size of the discharge hole

were varied to investigate their effects on dissociation of CO₂. The thickness of the dielectric layer, d , was chosen as 150, 300 and 450 μm , whereas the diameter of the discharge hole, D_{hole} , was chosen as 200, 400 and 515 μm .

Based on the atmospheric pressure (1 atm) and the size of the discharge hole used in this study, the breakdown voltage for pure CO₂ was solved iteratively as explained in detail in Section 2.2.3 using Townsend breakdown mechanism. Figure 7.1 shows the Paschen curve for CO₂ and the estimated breakdown voltages that correspond to the electrode separations used in this part of the study. The breakdown voltages were estimated as 2.1, 3.3 and 4.3 kV for the electrode separations of 150, 300 and 450 μm , respectively.

Carbon dioxide (99.5% purity, Matheson Tri-Gas) and argon as the carrier gas (99.998% purity, Airgas) were fed to the flow chamber through flow rate controllers. The H₂O saturator, the humidity and temperature controller shown in Figure 3.2 were not used in this part of the study. Flow rate in this study was chosen between 10 and 800 mL/min based on the limits of the flow rate controller. The gases were sampled at the reactor effluent and analyzed in gas chromatograph. Based on these values, the applied voltage was selected as 4.5 kV due to upper limit of the power supply used in the study.

Each parameter combination was independently repeated at least 4 times. The error bars in figures reported in the Results and Discussion section below reflect the standard deviation of the data obtained from these independent experiments.

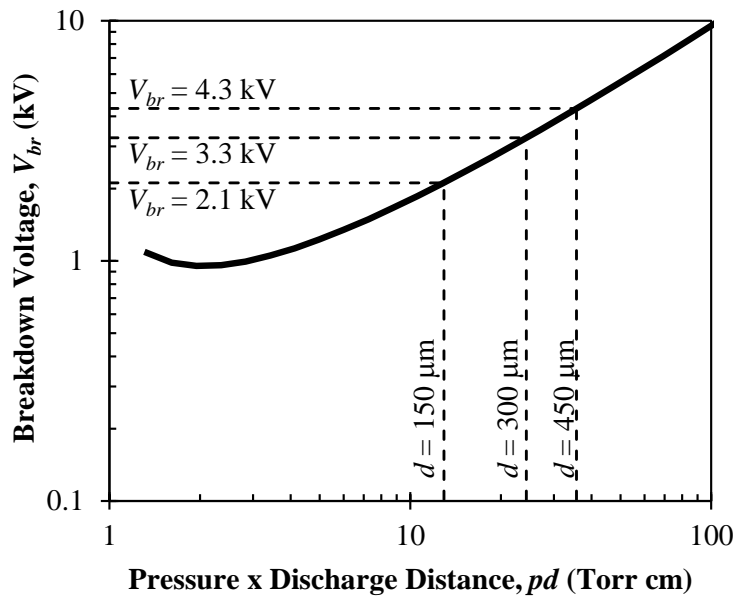


Figure 7.1. Breakdown voltage for CO₂ as a function of pressure times the discharge distance, and the breakdown voltages that correspond to the discharge distances used in this study.

7.3 RESULTS AND DISCUSSION

Prior to experiments to investigate the effects of geometrical parameters of the reactor, electric field distribution in the reactor was simulated before the first discharge, and the results are given in Appendix D. The simulations ignored the redistribution of the electric field and charges in the reactor due to discharges, and also the flow of the gas. The simulation results estimated that the dissociated gas volume decreased slightly as dielectric thickness increased from 150 to 450 μm . Thus, the yield would decrease slightly based on the electric field distribution in a stagnant CO₂ under uniform electric field. In addition, the simulation results suggested increasing the hole size would not change the maximum electric field in the gas, but the gas subjected to electric fields greater than breakdown electric field would be lower. Therefore, the conversion yield

would decrease. This section further investigates the effects of dielectric thickness and hole size through experiments with the redistribution of charges and electric field in the reactor.

7.3.1 Effects of Dielectric Thickness on Dissociation

Firstly, a series of experiments were conducted to investigate the effects of dielectric thickness on the performance of the MHCD reactor in dissociating CO₂. At an applied voltage of 4.5 kV and a discharge hole diameter of 400 μm, the flow rate was varied between 10 and 800 mL/min. Note that at a given reactor geometry, the residence time is inversely related to flow rate per Equation (3.10).

Figure 7.2 shows the gas concentrations of CO₂, CO and O₂ in the reactor effluent as functions of residence time for three different dielectric thicknesses. The results showed that increasing dielectric thickness decreased the concentrations of CO and O₂ for all residence times. At a residence time of 6 μs, CO and O₂ concentrations in the reactor effluent decreased by about 11% and 38%, respectively, as the dielectric thickness increased 3 times from 150 to 450 μm. Additionally, CO and O₂ concentrations decreased by 19% and 81%, respectively, by doubling the dielectric thickness at a residence time of 25.6 μs. Therefore, at longer residence times, the effect of dielectric thickness was more pronounced. Larger dielectric thickness at a given applied voltage reduced the electric field in the reactor as distance between the electrodes was greater. For this reason, lower electron energies, thus less ionization and dissociation, were expected at larger dielectric thicknesses due to lower electric field.

Moreover, Figure 7.2 shows the effect of residence time on the concentration of gases at the reactor effluent. In this figure, note that residence time was a function of both the flow rate and the dielectric thickness. The results showed that with increasing

residence time, concentration of CO₂ decreased exponentially, whereas concentrations of CO and O₂ increased linearly on a logarithmic scale. For a given reactor volume, the number of collisions in the reactor increased with residence time per unit mole of the fed gas. Therefore, higher the electron density was expected which would yield greater CO₂ dissociation as it was observed as in Figure 7.2. As the residence time increased 40 times, CO concentrations at the reactor effluent increased about 27.4, 20.4 and 15.6 times for dielectric thickness of 150, 300 and 450 μm, respectively. As the residence time decreased for all the dielectric thicknesses, the slopes of CO and O₂ concentrations were flattened. This must be due to very low concentrations of these species. Additionally, the stoichiometric balance on oxygen suggested that some of the oxygen content in the reactor influent converted to ozone, whereas the stoichiometric concentration for carbon was satisfied for all cases.

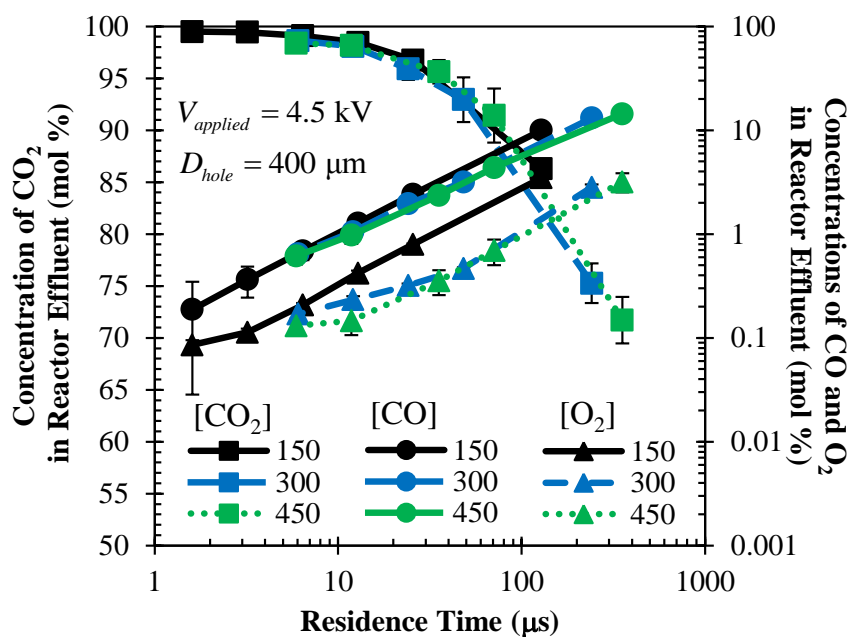


Figure 7.2. Concentrations of CO₂, CO and O₂ in the reactor effluent as functions of residence time for three different dielectric thicknesses. The legend shows the dielectric thickness in μm.

Figure 7.3 shows the energy density and self-pulsing frequency of the microdischarge reactor at different dielectric thicknesses as functions of residence time. The energy density presented here corresponds to the total energy consumed by the reactor over the duration of experiments per volumetric flow rate of CO₂ in the reactor influent. The energy density increased linearly with residence time on a logarithmic scale for each dielectric thickness. Energy density increased 71 times for 150 μm as the residence time increased 80 times from 1.6 to 128 μs. Additionally, the increase rate of energy density with residence time was about 2.6 times greater for the dielectric thickness of 150 μm than 450 μm. The increase in energy density with residence time could be related to the increase in electron density. As the electron density increased in the reactor, more inelastic collisions occur and more energy was dissipated through collisions, which, in return, increased the energy density.

Additionally, self-pulsing frequency increased almost exponentially with residence time. The relative increase was 28% for 150 μm and 72% for 450 μm as the residence time increased from 6 to 25.6 μs. As mentioned above, longer residence times yield higher electron densities. So, less time would be required to reach the electron density required for discharge to occur, and thus, self-pulsing frequency increased with residence time. For the same reason, electron density decreased with increasing dielectric thickness which yielded lower frequencies. For instance, at a residence time of 12.5 μs, the self-pulsing frequency decreased from 42.3 to 20.6 kHz as the dielectric thickness increased from 150 to 450 μm.

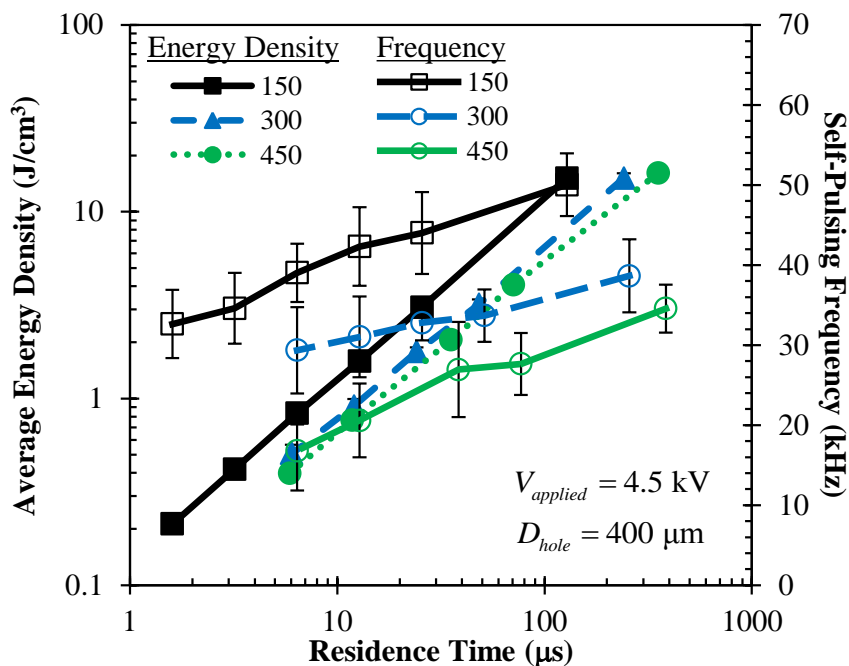


Figure 7.3. Energy density and self-pulsing frequency of the microdischarge plasma reactor as functions of residence time for three different dielectric thicknesses. The legend shows the dielectric thickness in μm .

Figure 7.4 shows the electrical-to-chemical energy conversion efficiency and CO_2 -to- CO conversion yield at different dielectric thicknesses as functions of residence time. The energy efficiency values mainly show how much of the electrical power consumption was used for generating CO at each experimental case. The results showed that at a given residence time, the energy conversion efficiency increased with dielectric thickness. This result could be attributed to lower energy density and higher CO concentration at larger dielectric thicknesses. At a residence time of $6 \mu\text{s}$, the energy conversion efficiency increased from 9.8% to 18.5% when the dielectric thickness increased from 150 to 450 μm . Additionally, the energy conversion efficiency decreased with increasing residence time as more energy was lost due to inelastic collisions at longer residence times as mentioned above. For instance, increasing the residence time 60

times from 5.9 to 354 μs , the energy efficiency decreased from 18.5% to 12.6% for the dielectric thickness of 450 μm .

The CO_2 -to-CO conversion yield showed a similar trend as CO concentration as the inlet concentration of CO_2 was constant in these cases. The CO_2 -to-CO conversion yield increased linearly with the residence time on a logarithmic scale for all dielectric thicknesses, and the maximum CO_2 -to-CO conversion yield was about 17.3% for the dielectric thickness of 450 μm and a residence time of 354 μs within the investigated range of parameters.

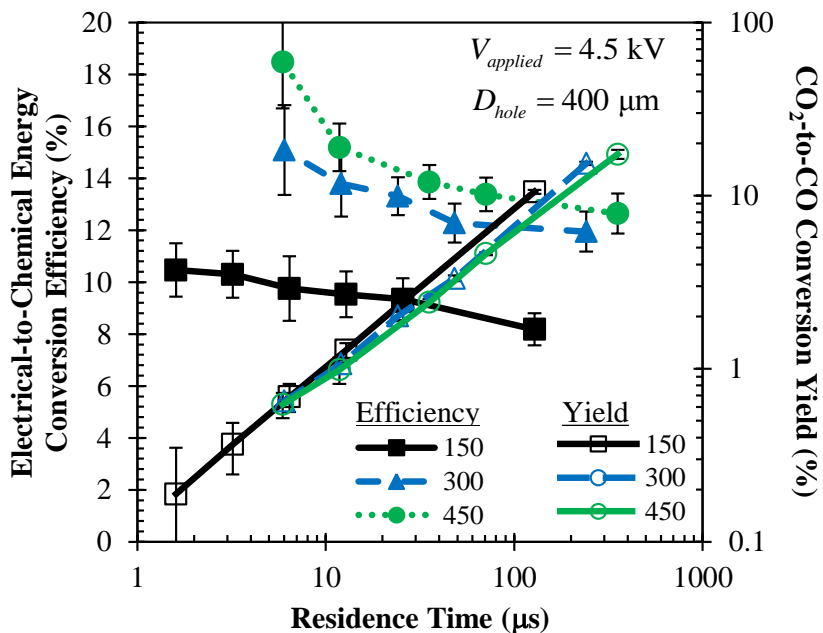


Figure 7.4. Energy conversion efficiency and CO_2 -to-CO conversion yield of the microdischarge reactor as functions of residence time for three different dielectric thicknesses. The legend shows the dielectric thickness in μm .

7.3.2 Effects of Discharge Hole Diameter on Dissociation

Secondly, the effect of hole size on CO₂ dissociation was analyzed using three different hole diameters, 200, 400 and 515 μm, at a constant applied voltage of 4.5 kV and a constant dielectric thickness of 150 μm. Figure 7.5 shows concentrations of CO₂, CO and O₂ at the reactor effluent as functions of residence time at the specified hole diameters. The effect of residence time was discussed in the previous section and not repeated here for brevity. The figure shows that concentrations of CO and O₂ decreased with increasing hole size. For instance, at the residence time of 6 μs, CO concentrations at the reactor effluent were 2.6%, 0.7% and 0.4% for hole diameters of 200, 400 and 515 μm, respectively. Similar results were obtained at other residence times as shown in Figure 7.5. The decrease in CO₂ dissociation with increasing hole size could be attributed to the electric field distribution in the discharge hole. In smaller hole sizes, the magnitude of the electric field near the electrodes would be higher due to pendulum effect which was expected to result in more energetic electrons and more probability for ionization and dissociation to occur in the plasma through collisions [80, 86].

Figure 7.6 shows the required average energy density consumed to dissociate CO₂ and self-pulsing frequency as functions of residence time at the specified hole sizes. The energy density increased with decreasing hole size at a given residence time and constant applied voltage. Energy density decreased about 3.7 times as the hole diameter increased from 200 to 400 μm and about 1.8 times from 400 to 515 μm. This decrease could be attributed to the decrease in the electron densities and energies in the reactor at a given instant as explained above. Lower electron densities and energies resulted in fewer and less energetic collisions, and thus, energy lost through inelastic collisions would be lower.

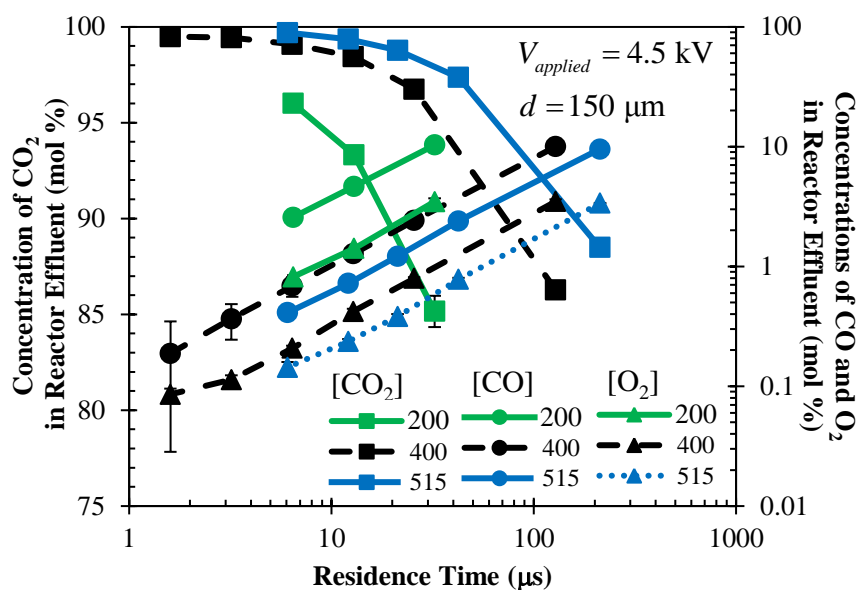


Figure 7.5. Concentrations of CO₂, O₂ and CO in the reactor effluent as functions of residence time for three different hole diameters. The legend shows the hole diameter in μm.

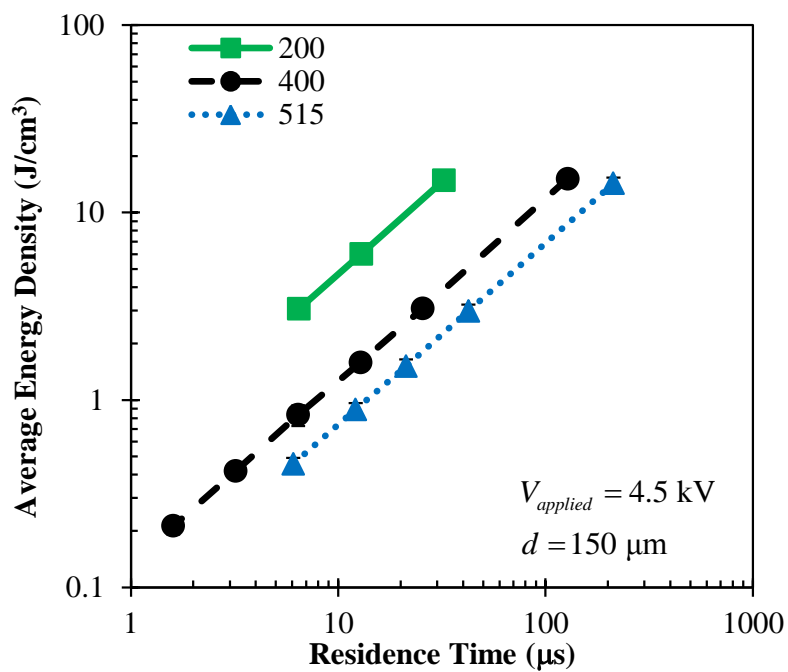
Additionally, Figure 7.6 shows the self-pulsing frequency at the specified hole sizes. As mentioned above, larger hole sizes yielded lower electron densities. For this reason, at larger hole sizes, more time was required to reach the required number of charges for discharge at a given applied voltage. Thus, self-pulsing frequency decreased with increasing hole size. For instance, as the hole diameter increased from 200 to 515 μm, the frequency increased by about 22% and 28% at residence times of 6 and 13 μs, respectively.

Figure 7.7 shows the electrical-to-chemical energy conversion efficiency and CO₂-to-CO conversion yield as functions of residence time at the specified hole diameters. Energy conversion efficiency increased with decreasing residence time or with

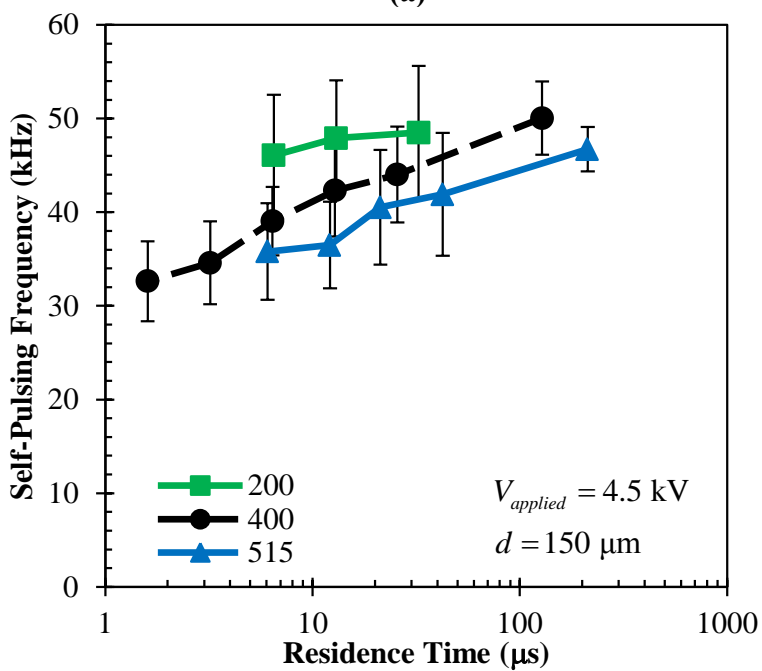
increasing hole size. The highest observed energy conversion efficiency was about 10.6% for the hole size of 515 μm at a residence time of 6 μs which was equal to the energy conversion efficiency for the hole size of 400 μm and a residence time of 1.6 μs . The results suggested that larger power consumption could not be compensated by higher CO production due to higher charge density, so lower efficiency was obtained at smaller hole sizes at a given residence time and dielectric thickness.

As in the previous section, the CO_2 -to-CO conversion yield reflected the CO concentration at different hole sizes as the CO_2 concentration at the reactor influent was the same for all cases. The conversion yield increased linearly with the increasing residence time on a logarithmic scale for all dielectric thicknesses, and decreased with increasing hole diameter. The conversion yield decreased about 3.8 and 1.7 times as the hole size increased from 200 to 400 μm and from 400 to 515 μm , respectively. The obtained trends showed that it could be possible to reach about 90% conversion yield for the hole diameter of 200 μm at a residence time of 350 μs .

The simulation results given in Appendix D, Section D.2.2 overestimated the conversion yield as the dielectric thickness and hole diameter varied as the model assumed uniform electric field in the reactor and did not consider the redistribution of charges and electric field. However, the simulation results showed similar trend as in the experimental results, especially the significance of hole size being higher than that of dielectric layer in terms of improving conversion yield.

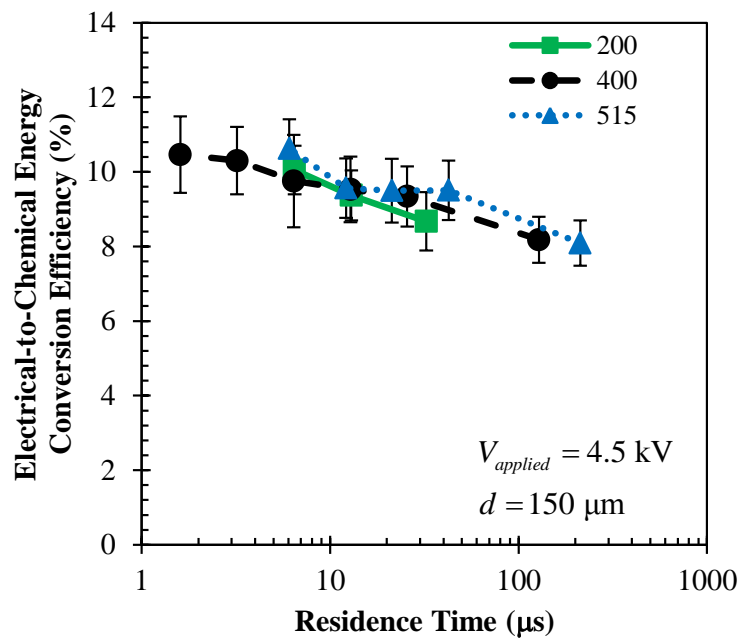


(a)

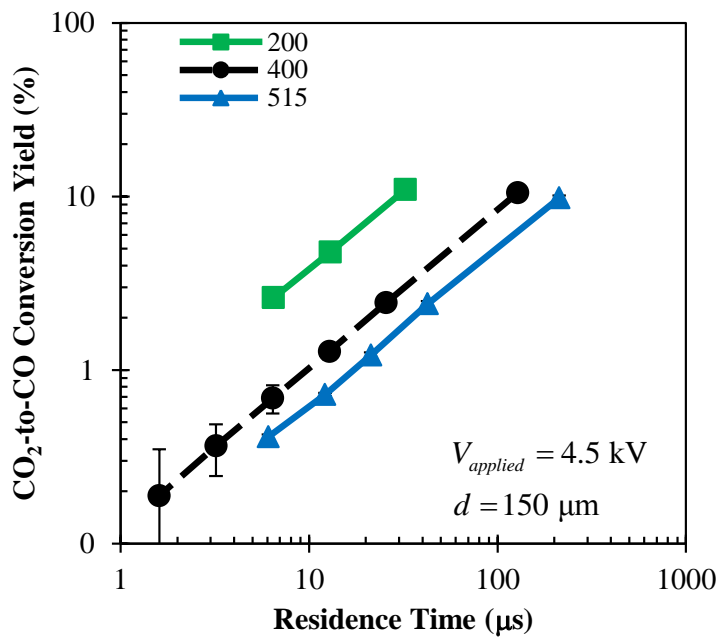


(b)

Figure 7.6. (a) Energy density, and (b) self-pulsing frequency of the microdischarge plasma reactor as functions of residence time for three different hole diameters. The legend shows the hole diameter in μm.



(a)



(b)

Figure 7.7. (a) Electrical-to-chemical energy conversion efficiency, and (b) CO_2 -to-CO conversion yield as functions of residence time for three different hole diameters. The legend shows the hole diameter in μm .

7.4 CHAPTER SUMMARY

An experimental study was presented for CO₂ dissociation using a prototype MHCD plasma reactor. The MHCD reactor consisted of two hollow electrodes that were separated by a dielectric material. The objective of this study was to investigate the effects of the dielectric thickness and the hole size on the performance of the MHCD reactor in terms of CO₂ dissociation. CO₂ was fed to the reactor at different flow rates and DC voltage was applied to the reactor. The performance of the reactor was quantified in terms of concentration of gases at the reactor effluent, electrical-to-chemical energy conversion efficiency and CO₂-to-CO conversion yield. The results showed that conversion yield decreased, but efficiency increased with increasing dielectric thickness and hole diameter for all residence times. The maximum energy conversion efficiency obtained was 18.5% for the dielectric thickness of 450 μm and a residence time of 6 μs. Based on the obtained trends, the conversion yield could reach about 90% for hole diameter of 200 μm at a residence time of 350 μs.

To conclude this chapter, the energy conversion efficiency and conversion yield were found to be competing as dielectric thickness and hole diameter were varied. Depending on the application, higher conversion yield could be obtained by using thin dielectric material and small discharge hole at a given residence time. Additionally, longer residence times and larger voltage could be applied for higher yields. The opposite should be considered to increase the energy conversion efficiency. Overall, this chapter successfully demonstrated the potential of CO₂ dissociation using a MHCD plasma reactor under atmospheric pressure. For the investigated range of parameters, the energy conversion efficiency values were low, although CO₂-to-CO conversion yield values were promising.

Chapter 8

Summary, Conclusions and Recommendations

8.1 SUMMARY

This study focused on the dissociation of H₂O and CO₂ in a microhollow cathode discharge reactor (MHCD) for hydrogen and syngas generation. A MHCD reactor was prototyped which consisted of three layers; one layer of mica as dielectric and single layers of electrode on each side of the dielectric with a through hole across these three layers.

The first part of the study, Chapter 4, presented the electrical characterization and equivalent circuit modeling of a MHCD reactor operating in self-pulsing regime. The prototyped reactor was operated for atmospheric air plasmas at different applied DC voltages while measuring the voltage across and current through the reactor using high voltage probes. The experimental current and voltage characteristics showed that the reactor had a capacitive behavior, and showed two distinct regimes as charging and discharging regimes. In the equivalent circuit model, the capacitance behavior was attributed to a constant capacitance and the self-pulsing behavior was related to a variable, negative differential resistor in parallel with the capacitor. The results also showed that the maximum voltage corresponded to the breakdown threshold of the gas, and it decreased with increasing applied voltage. Additionally, increasing applied voltage increased the peak, average and minimum current as well as the power consumption and self-pulsing frequency of the reactor. The parameters of the proposed model were adjusted to reflect the changes in the magnitudes of current and voltage as a function of applied voltage. The introduced equivalent circuit model was in better agreement with the experimental results than the other models reported in the literature in terms of predicting

both the temporal waveforms and magnitudes of voltage and current. Given the physics of discharges and the nature of MHCD reactors, the equivalent circuit model would be valid for different gases, reactor dimensions and pressures provided that the model parameters are adjusted based on the conditions.

Chapter 5 experimentally demonstrated carbon dioxide dissociation using microhollow cathode discharge plasma reactor in the self-pulsing regime at atmospheric pressure, and investigated the CO₂ dissociation performance of a microhollow cathode discharge plasma reactor as functions of applied voltage (from 2.5 to 4.5 kV), gas flow rate (from 10 to 800 mL/min) and CO₂ mole fraction in the influent gas mixture (from 9.95% to 99.5%). The performance of the reactor was evaluated based on the gas composition at the reactor effluent, power consumption, electrical-to-chemical energy conversion efficiency and CO₂-to-CO conversion yield. The results reported in this chapter can be summarized as follows:

- Within the investigated parameters range, the results suggested using higher applied voltage or smaller flow rates or to dilute CO₂ with high concentration of carrier inert gas to increase the dissociation rate of CO₂.
- Time-averaged power requirement of the reactor increased with applied voltage, inlet flow rate or inlet CO₂ concentration. The average power requirement was less than 3 W for all the analyzed cases.
- The self-pulsing frequency was found to be directly related to the average discharge current, the dissociation rate and the CO₂-to-CO conversion yield. For all the analyzed parameters, frequency varied between 12 and 72 kHz as it increased with increasing applied voltage or with decreasing the flow rate or inlet concentration.

- Within the analysis of this study, the maximum electrical-to-chemical energy conversion efficiency was found to be 21% for 99.5% pure CO₂ at an applied voltage of 4.5 kV, inlet flow rate of 800 mL/min. Additionally, the results showed the maximum CO₂-to-CO conversion yield of 99.5% pure CO₂ as 10.5%, which was achieved at an applied voltage of 4.5 kV and an inlet flow rate of 800 mL/min. Higher conversion yields can be obtained with higher residence times.
- Diluting CO₂ with an inert gas or a gas with lower breakdown voltage increased the dissociation rate and the conversion yield at a penalty in energy conversion efficiency. For instance, if N₂ which is the major component in air exists in the influent gas, it would increase the yield as the breakdown voltage of N₂ is lower than that of CO₂, but presence of N₂ would also yield NO_x generation.

In Chapter 6, argon and carbon dioxide was saturated with water and fed to the MHCD reactor through the humidity and temperature controller at three different flow rates at atmospheric pressure. A direct-current high voltage of 4.5 kV was applied to one of the electrodes and the other electrode was grounded. High voltage probes were used to measure voltage drop across the reactor and across a current viewing resistor to obtain discharge current. The performance metrics used in this chapter were the same as in Chapter 5. Voltage and current characteristics of each experimental case were also compared. Based on the obtained results, the following conclusions can be made:

- Average current, which was a strong function of the gas but weak function of flow rate, signified the charge density in the reactor. Additionally, the

maximum voltage of each case showed the corresponding breakdown value.

- Within the parameter ranges used in this study, the maximum hydrogen yield was about 28.4% from saturated argon whereas it was about 4.9% from saturated carbon dioxide at a flow rate of 10 mL/min. This suggested that an inert gas with high ionization energy was favorable as a carrier gas for hydrogen production in MHCD plasma reactors.
- The decrease in yield with increasing flow rate was mainly due to lower charge density in the reactor.
- Introducing water vapor in carbon dioxide increased the CO yield from 10.5% to 14.5% at 10 mL/min. This result showed that a gas could be subjected to higher degree of dissociation when it is fed with low concentration of a gas that has lower ionization energy than the gas itself.
- The maximum energy conversion efficiencies of about 14.8% and 2.0% were obtained for saturated carbon dioxide and argon, respectively. The efficiency for argon was lower as some of the energy input was lost to ionizing and heating argon which enhanced the conversion yield.

In Chapter 7, another experimental study was presented to investigate the effects of the dielectric thickness (from 150 to 450 μm) and the hole size (from 200 to 515 μm) on the performance of the MHCD reactor in terms of CO_2 dissociation. CO_2 was fed to the reactor at different residence times and DC voltage was applied. The performance of the reactor was quantified in terms of the same performance metrics as in the previous chapters. Based on the obtained results the following conclusions can be drawn:

- CO₂ dissociation rate decreased with increasing dielectric thickness for all residence times. For instance, at a residence time of 6 μs, CO concentration in the reactor effluent decreased by about 11% as the dielectric thickness increased from 150 to 450 μm.
- Increasing the dielectric thickness decreased the energy conversion efficiency, but decreased the conversion yield. The maximum energy conversion efficiency was obtained as 18.5% for the dielectric thickness of 450 μm and a residence time of 6 μs. Additionally, based on the obtained trends, the conversion yield could reach to 87% for the dielectric thickness of 150 μm at a residence time of 1.28 ms.
- CO₂ dissociation rate decreased with increasing hole diameter regardless of the residence time. For instance, at the residence time of 6 μs, the CO concentration at the reactor effluent were 2.6% and 0.4% for hole diameters of 200 and 515 μm, respectively.
- Increasing the discharge hole diameter increased the energy conversion efficiency, but decreased the conversion yield. Based on the obtained trends, the energy efficiency could reach about 13% for the hole diameter of 515 μm at a residence time of 1 μs. Similarly, the conversion yield could reach about 90% for hole diameter of 200 μm at a residence time of 350 μs.
- Experimentally obtained energy density and self-pulsing frequency were used to show that the electron energy and density increased with residence time and dielectric thickness, but decreased with hole diameter.

8.2 CONCLUSIONS

The major conclusions of this study can be listed as follows:

- Residence time significantly affected the conversion yields.
 - CO₂-to-CO conversion yield could reach 97% at the residence time of 1.2 ms for 99.5% pure CO₂ in a reactor with a dielectric thickness of 150 μm and a hole diameter of 400 μm operating at an applied voltage of 4.5 kV.
 - Maximum H₂O-to-H₂ conversion yield of 28.4% observed for saturated argon at the residence time of 128 μs in a reactor with a dielectric thickness of 150 μm and a hole diameter of 400 μm operating at an applied voltage of 4.5 kV.
 - Residence times did not affect energy efficiency significantly.
- When the power consumption of the reactor per flow rate increased,
 - The conversion yields increased linearly.
 - The electrical-to-chemical energy conversion efficiency decreased logarithmically.
 - The maximum electrical-to-chemical energy conversion efficiency was achieved as 18.5% for 99.5% pure CO₂ at a residence time of 6 μs in a reactor with a dielectric thickness of 450 μm and a hole diameter of 400 μm operating at an applied voltage of 4.5 kV.
- Energy efficiency and conversion yield were competing objectives. Increasing yield required high electron density and energies which were attributed to the energy density in the reactor. Increasing energy density required larger power consumption which reduced energy efficiency.

- It was observed that higher conversion yield was obtained at,
 - higher applied voltages
 - longer residence times or smaller flow rates
 - higher concentrations of inert carrier gas
 - thinner dielectric material
 - smaller discharge hole

When the MHCD reactor and its performance for dissociation were compared with the other state-of-the-art technologies proposed in the literature, the following conclusions can be drawn:

- Electrochemical reactors show dissociation rates on the order of 10 cm³/min [110, 134] which are similar to the MHCD reactor. However, the electrochemical reactors are prone to changes in composition of electrolyte, and they are very sensitive to the purity of electrodes which typically degrade after couple of operational hours. The MHCD reactor was successfully tested up to 27 hours in the self-pulsing regime. Additionally, in electrochemical reactors, the electrolytes need to be saturated with the gas before the operation which requires couple of hours of set-up time before the operation.
- A photocatalytic reactor with AlGa_{0.3}N/GaN and Cu electrodes in 3.0M KCl solution showed an energy conversion efficiency of 0.13% which was close to plants' photosynthetic efficiency [136]. The efficiencies reported in this study were much higher than these photocatalytic reactors.
- Solar thermochemical reactors required temperatures higher than 1500°C for operation and featured solar-to-chemical energy conversion

efficiencies less than 1% [44]. The operating temperatures of MHCD reactor was much lower than the operating temperatures of solar thermochemical reactors, and the efficiencies were greater even if solar conversion efficiency of 20% was considered. Additionally, due to high temperatures in solar thermochemical reactors, the products need to be quenched whereas the products of MHCD reactor do not need quenching.

- A dielectric barrier discharge (DBD) reactor with alternating-current excitation showed conversion yield of 18% at an energy density of 23 J/cm^3 [146] compared to 17% of MHCD reported in this study. Although the yields were comparable, the AC excitation of DBD reactor would add more complexity to the operation of the reactor and extra cost for the overall system. Additionally, DBD reactor was operated at 19.5 kV_{AC} and showed an energy conversion efficiency of 35%. Even though this study showed lower efficiencies, the applied voltages were lower, and it was observed that higher applied voltages yielded to higher efficiencies.

Therefore, when compared with other available technologies in the literature, the MHCD reactor featured many advantages for dissociating gases and producing syngas. The opposite should be considered to increase the energy conversion efficiency. Overall, this experimental study successfully demonstrated the potential of H_2O and CO_2 dissociation for syngas and hydrogen production using a MHCD plasma reactor under atmospheric pressure. For the investigated range of parameters, the results showed that the MHCD reactors can be used to effectively couple electric energy into chemical bonds and dissociate gases, especially when compared to other state-of-the-art technologies given in the literature.

8.3 RECOMMENDATIONS FOR FUTURE RESEARCH

Based on the obtained results in this study, the following recommendations can be made for future research to improve the performance of the reactor and to better understand the physical phenomena behind the operation of the reactor.

- Chapter 4 shows the electrical characterization of the reactor as a function of applied DC voltage and proposes an equivalent circuit model for stagnant air. The results in the other chapters showed that the flow rate of the gas affected the self-pulsing frequency which was on the same order of magnitude as the residence time of the gas in the discharge hole. To further investigate the relation between the flow rate and the self-pulsing frequency, the equivalent circuit model in this study should be expanded to incorporate the gas flow and relate the model parameters to the flow rate or residence time. This model can help understanding the physical effect of flow rate on gas dissociation. The results of this study can provide necessary and sufficient data to expand the proposed circuit model for CO₂ at different applied voltages, flow rates, concentrations at the reactor effluent and reactor dimensions.
- To increase the conversion yield or the syngas production rate of the reactor, higher voltages should be applied. At a given reactor geometry, flow rate and concentration, the transition from self-pulsing regime to normal regime would occur. Therefore, there is an upper limit of the applied DC voltage at a given reactor geometry and operating pressure. If the reactor would be operated at that limit, the conversion yield limits could be experimentally quantified. The drawback of applying higher voltages would be higher gas temperatures. To overcome overheating the gas issues, alternating or pulsed excitation can also be

used at an appropriate frequency for continuous and stable operation of the reactor.

- To further increase the conversion yield or the syngas production rate of the reactor, reactors with smaller discharge hole diameters should be manufactured. As mentioned in Chapter 7, smaller hole size would be expected to yield to higher electron density near cathode due to the nature of pendulum effect of the hollow cathode. Additionally, more uniform charge distribution would be predicted in the discharge hole based on the expected electric field distribution in the hole. However, with smaller hole sizes, higher pressure drops would occur across the reactor and should be taken into account during the experiments and analyses.
- One of the ways to increase the energy conversion efficiency is operating the reactor at lower pressures. Based on the breakdown voltages predicted by Paschen curve, the voltage requirement would be lower at lower voltages which would decrease the power consumption. Additionally, the energy loss mechanisms such as gas heating can be assessed to increase the efficiency by minimizing these losses for each mechanism.
- To enhance the H_2/CO ratio in syngas, the influent gas can be pre-heated. Therefore, the partial pressure of water vapor in carbon dioxide would be higher in the influent gas. Alternatively, H_2O and CO_2 can be dissociated in two different reactors in parallel to enhance H_2/CO ratio. This ratio can be adjusted as necessary by optimizing the operating parameters of these reactors independently. Additionally, hydrolyzer can be used in addition to the plasma reactor to supplement the H_2 content in syngas if required.

- The presence of nitrogen in the influent stream can be analyzed experimentally, as N_2 is the major component of air, and N_2 and NO_x would exist if air is used as an oxidizer. Therefore, it would be beneficial to use N_2 as the carrier gas for saturated CO_2 and investigate the performance difference of the MHCD reactor for syngas production. Additionally, difference in NO_x concentration between the influent and effluent gas would also be analyzed.
- Although the effect of electrode degradation was inherently included in the results of this study, it should be studied independently. An online gas chromatograph and mass spectroscope can be used to identify the product yield and conversion efficiencies as a function of time. Ultimately, the degradation of electrodes should be eliminated for better performance of the reactor as well as for longer operation times. Although electrodes with enhanced durability, such as nickel or platinum based electrodes would show lower degradation, they would also increase the cost of the reactor. Alternatively, operating the reactor with pulsed or alternating excitation would also decrease the degradation rate of electrodes. For instance, square wave excitation with frequency lower than self-pulsing frequency would increase the lifetime of the reactor by changing the polarity of the electrodes without affecting the discharge formation.
- The identification of species, their number densities and temperatures as well as number density and temperature of electrons can be estimated using spectroscopy. If fast spectroscopy is used, it would be possible to distinguish discharging and charging regimes of the self-pulsing regime in terms of number density of species and their temperatures. Additional to temporal variation, depending on the spatial resolution of the spectroscope, the local dissociation rates could be investigated,

and therefore, effects of each parameter analyzed in this study would be further discussed and justified. One example of this analysis can be the size of sheath regions as the operational parameters vary. As a result of these analyses, more recommendations can be made to enhance the dissociation, efficiency and syngas production.

- Stacked reactors in series or parallel can be established to enhance the production of hydrogen and syngas. The parallel reactors would enhance the production rate whereas the reactors in series would enhance the yield.
- The renewable energy can be incorporated to this reactor for hydrogen and syngas production. Based on the availability of the renewable energy, demand and supply relation can be established for economical and life-cycle analyses to assess the viability of this proposed method. Using these analyses, it would be also possible to show the feasibility of scaling up the system.

Appendices

Appendix A Nomenclature

A	area [m^2]
C	capacitance [F]
d	distance between electrodes [m]
D	diameter [m]
e	energy density [J m^{-3}]
E	electric field [V m^{-1}]
f	frequency [Hz]
\bar{H}	enthalpy [kJ kmol^{-1}]
I	current [A]
L	length [m]
\dot{n}	molar flow rate [mol s^{-1}]
p	pressure [Pa]
P	power [W]
R	resistance [Ω]
t	time [s]
V	voltage [V]
\dot{V}	volumetric flow rate [mL min^{-1}]
X	equivalent resistance [Ω]
Z	impedance [Ω]

Greek Symbols

α	Townsend coefficient [m^{-1}]
----------	--

ε	conversion yield
η	electrical-to-chemical energy conversion efficiency
τ	time constant

Subscripts

<i>avg</i>	average
<i>br</i>	breakdown
<i>C</i>	capacitor
<i>cvr</i>	current viewing resistor
<i>d</i>	discharge
<i>deg</i>	degraded
<i>exp</i>	experimental
<i>in</i>	reactor influent/inlet
<i>res</i>	residence
<i>rxn</i>	reaction
<i>v</i>	volumetric

Appendix B

Numerical Codes Used in the Study

B.1 PASCHEN CURVE CALCULATION

This code was used to calculate the breakdown voltage and electric field for gases, and to plot the Paschen curves which show breakdown voltage as a function of pressure times the distance between the electrodes. This script was written in MATLAB.

```
1  % Purpose: Calculate Paschen curves for plasma generation via Townsend breakdown
2      mechanism
3  % by Onur Taylan, December 2012
4  % Ref: A. Fridman and L. A. Kennedy, Plasma Physics and Engineering, CRC, 2004.
5  % Limitation: Townsend breakdown is valid for  $pd < 4000$  Torr cm
6
7  clear all
8
9  i = 0; % setting the loop
10 for d = logspace(-3,1) % solving for a range of electrode gap
11     i = i + 1;
12     A = 5; % [cm-1 Torr-1] 15 for Air, 20 for CO2. It is approximated by
13          $1/(p*\text{mean\_free\_path})$  [AME60637 Notes].
14     B = 130; % [V cm-1 Torr-1] 365 for Air, 466 for CO2. It is approximated by
15          $A/E_{\text{ionization}}$  [AME60637 Notes].
16     p = 760; % [Torr]
17
```

```

18 gamma(i) = fsolve(@(x) (1/(exp((p*A*exp(B*p/(p*B/((log(A)-
19 log(log(1/x+1)))+log(p*d)))))*d)-1)-x),0.01,optimset('Display','off')); %
20 iteratively solving for the parameter, gamma
21
22 C(i) = log(A) - log(log(1/gamma(i)+1));
23 E(i) = p * B / (C(i)+log(p*d)); % the breakdown electric field
24 alfa(i) = p * A * exp(B*p/E(i));
25 gamma_new(i) = 1 / (exp(alfa(i)*d)-1); % calculating gamma after the solver
26 error(i) = abs(gamma_new(i)-gamma(i)); % checking the accuracy of the solver
27
28 V(i) = B*p*d/(C(i)+log(p*d)); % the breakdown voltage
29 end

```

B.2 ENERGY EFFICIENCY AND CONVERSION YIELD CALCULATION

This code was used to calculate the chemical-to-electrical energy conversion efficiency, and the H₂O-to-H₂ and CO₂-to-CO conversion yields based on the volumetric flow rate of influent gas at a given temperature, pressure and humidity, average power consumption and gas concentrations at the reactor effluent. This script was written in Visual Basics.

```

1 Function PlasmaCalc(ConcCO2 As Double, ConcCO As Double, ConcO2 As Double,
2 ConcH2 As Double, Humidity As Double, VolFlowRate As Double, Power As
3 Double) As Double

```

```

4      ' This code calculates the electrical-to-chemical conversion efficiency for
5          humidified CO2
6      ' by Onur Taylan, March 2013
7      ' Inputs:      ConcX [%] where X is the specified species
8      '              Humidity [-]
9      '              VolFlowRate [m3/s]
10     '              Power [W]
11     ' Outputs:     PlasmaEfficiency [-]
12     '              PlasmaYieldH2 [-]
13     '              PlasmaYieldCO [-]
14     '              SpecificEnergy [J/m3]
15
16     Dim ResultMatrix(4)
17     ' Constants
18     DH_CO = 110.53 * 1000      ' kJ/kmol
19     DH_CO2 = 393.52 * 1000    ' kJ/kmol
20     DH_H2O = 241.82 * 1000    ' kJ/kmol
21     DH_O2 = 0 * 1000          ' kJ/kmol
22     DH_rxn = 282.99 * 1000    ' kJ/kmol
23     DH_rxnH2O = 241.82 * 1000' kJ/kmol
24     Density_CO2 = 1.842       ' kg/m3
25     Density_CO = 1.165        ' kg/m3
26     Density_O2 = 1.331        ' kg/m3
27     Density_H2 = 0.0852       ' kg/m3

```

```

28     Density_H2O = 1 / 43.36    ' kg/m3
29     MCO2 = 44    ' kg/kmol
30     MCO = 28    ' kg/kmol
31     MO2 = 32    ' kg/kmol
32     MH2 = 2    ' kg/kmol
33     MH2O = 18    ' kg/kmol
34     Ptot = 101.3    ' kPa
35     Psat = 3.169    ' kPa at 25degC for H2O
36     Temperature = 25 + 273.15    ' K
37     Rbar = 8.314    ' kJ/kmol/K
38
39     ' Calculations for flow rates in the reactor influent
40     MoleFlowRateInTot = Ptot * VolFlowRate / Temperature / Rbar    ' kmol/s
41     MoleFlowRateCO2In = MoleFlowRateInTot * (Ptot - Humidity * Psat) / Ptot
42     ' kmol/s
43     MoleFlowRateH2OIn = MoleFlowRateInTot * (Humidity * Psat) / Ptot    ' kmol/s
44     MassFlowRateH2OIn = MoleFlowRateH2OIn * MH2O    ' kmol/s
45     MassFlowRateCO2In = MoleFlowRateCO2In * MCO2    ' kmol/s
46     MassFlowRateInTot = MassFlowRateH2OIn + MassFlowRateCO2In    ' kg/s
47
48     ' Calculations for flow rates in the reactor effluent
49     Mout = (ConcCO * MCO + ConcO2 * MO2 + ConcCO2 * MCO2 + ConcH2 *
50     MH2 + ConcH2Oout * MH2O)
51     xH2 = ConcH2 * MH2 / Mout

```

```

52     xCO = ConcCO * MCO / Mout
53     MassFlowRateCO = xCO * MassFlowRateInTot    'kg/s
54     MassFlowRateH2 = xH2 * MassFlowRateInTot    'kg/s
55     MoleFlowRateH2 = MassFlowRateH2 / MH2      'kmol/s
56     MoleFlowRateCO = MassFlowRateCO / MCO      'kmol/s
57
58     ' Calculation for the energy efficiency, yields and specific energy
59     ResultMatrix(1) = (MoleFlowRateCO * DH_rxn + MoleFlowRateH2 *
60         DH_rxnH2O) / (Power / 1000)            ' PlasmaEfficiency
61     ResultMatrix(2) = (MoleFlowRateH2) / (MoleFlowRateH2OIn) ' PlasmaYieldH2
62     ResultMatrix(3) = (MoleFlowRateCO) / (MoleFlowRateCO2In) ' PlasmaYieldCO
63     ResultMatrix(4) = (Power) / (VolFlowRate)   ' SpecificEnergy
64
65     PlasmaCalc = ResultMatrix
66
67     End Function

```

Appendix C

Gas Chromatograph Analysis

A gas chromatograph analyzes the composition and concentration of sample gas by flowing it through long capillary tubes, called column, with a carrier gas as mobile phase. The columns are generally packed with specific fillings as stationary phase so that the components of the sample gas can be separated based on their physical and chemical properties. At the exit of the column, detectors are used to identify the component based on their retention times.

In this study, gas chromatograph (Shimadzu GC-2014) was used to identify the gases and their concentrations at the influent and effluent of the reactor. Three stainless steel columns (Sigma-Aldrich Supelco) were used; (i) HayeSep N with a length of 3 m, inner diameter of 2.1 mm, (ii) HayeSep T with a length of 2 m, inner diameter of 2.1 mm, and (iii) mole sieve 5A with a length of 2.5 m, inner diameter of 2.1 mm. Argon was used as the carrier gas in both columns. At the end of columns, the gas chromatograph had two detectors, flame ionization detector (FID) as Channel 1, and the thermal conductivity detector (TCD) as Channel 2. FID was equipped with a methanizer that was heated up to 380°C. FID is mainly used to detect hydrocarbons, and was used to determine CO₂ and CO concentrations in this study. Whereas, TCD detect components based on the thermal conductivity differences, and was used to detect H₂, O₂ and N₂ in this study.

C.1 CALIBRATION OF GAS CHROMATOGRAPH

Before analyzing the gases in the gas chromatograph (Shimadzu GC-2014), it is calibrated for 6 different gases using a gas calibration standard (SCOTTY 48). This standard contains 1 mol% each of CO₂, CH₄, CO, H₂ and O₂ in 95 mol% of N₂. This gas

sample was injected to the gas chromatograph using glass syringes (Hamilton SampleLock Series 1700) of 50, 100 and 250 μL . Using three different volumes allows three-point, linear calibrations for each gas as shown below. This section shows the results of gas chromatograph calibration in terms of area versus concentration plots for each gas and their corresponding parameters of goodness of fit.

C.1.1 Carbon Dioxide

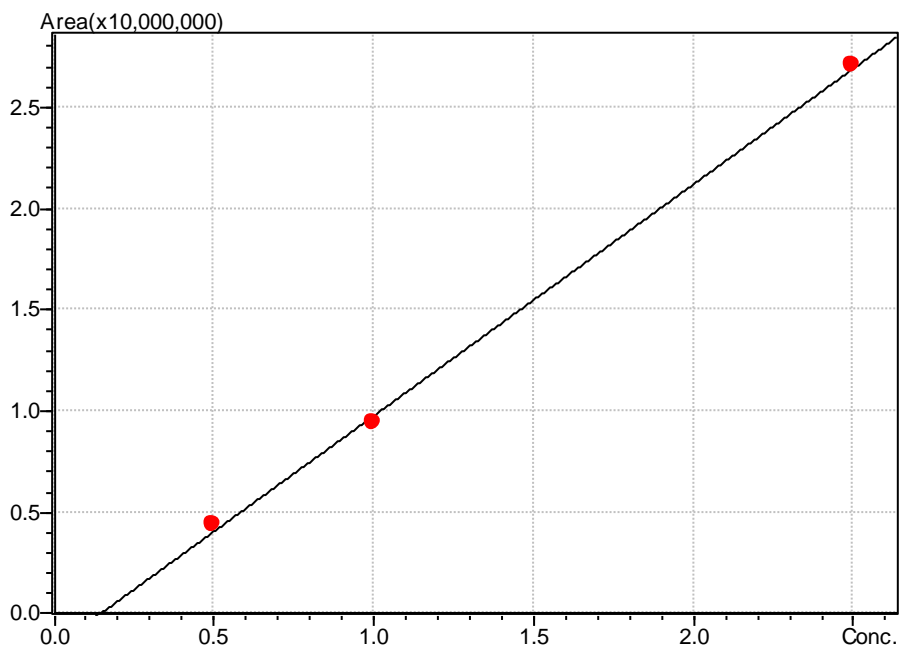


Figure C.1. Calibration curve for carbon dioxide.

$$Y = aX + b$$

$$a = 1.142785 \times 10^7$$

$$b = -1612773$$

$$R^2 = 0.9990703$$

$$R = 0.9995351$$

$$\text{Mean RF} : 9680544$$

RF SD : 1034810

RF %RSD : 10.68959

C.1.2 Methane

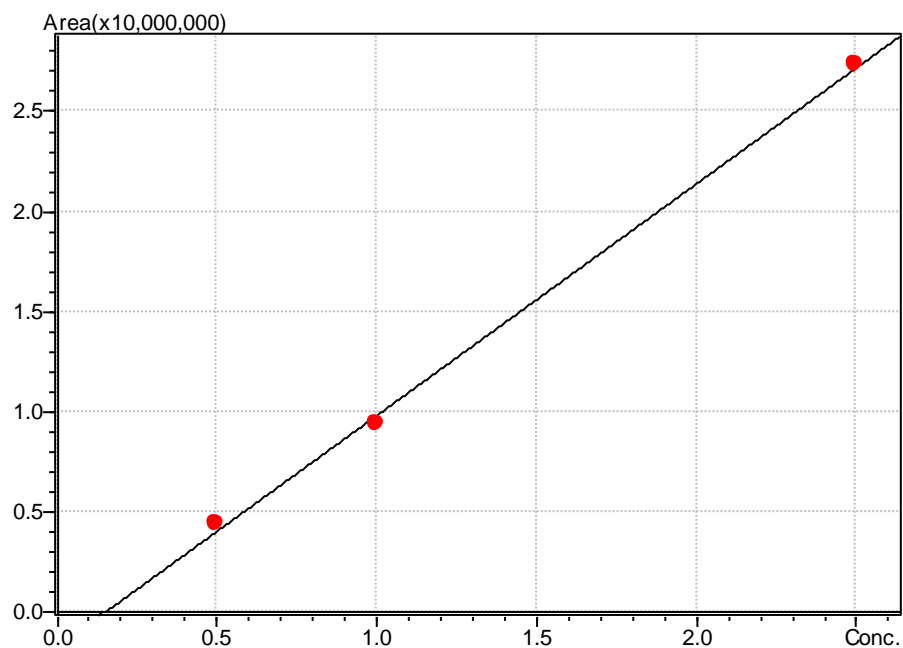


Figure C.2. Calibration curve for methane.

$$Y = aX + b$$

$$a = 1.156086 \times 10^7$$

$$b = -1675576$$

$$R^2 = 0.9987459$$

$$R = 0.9993728$$

Mean RF : 9756479

RF SD : 1052440

RF %RSD : 10.78709

C.1.3 Carbon Monoxide

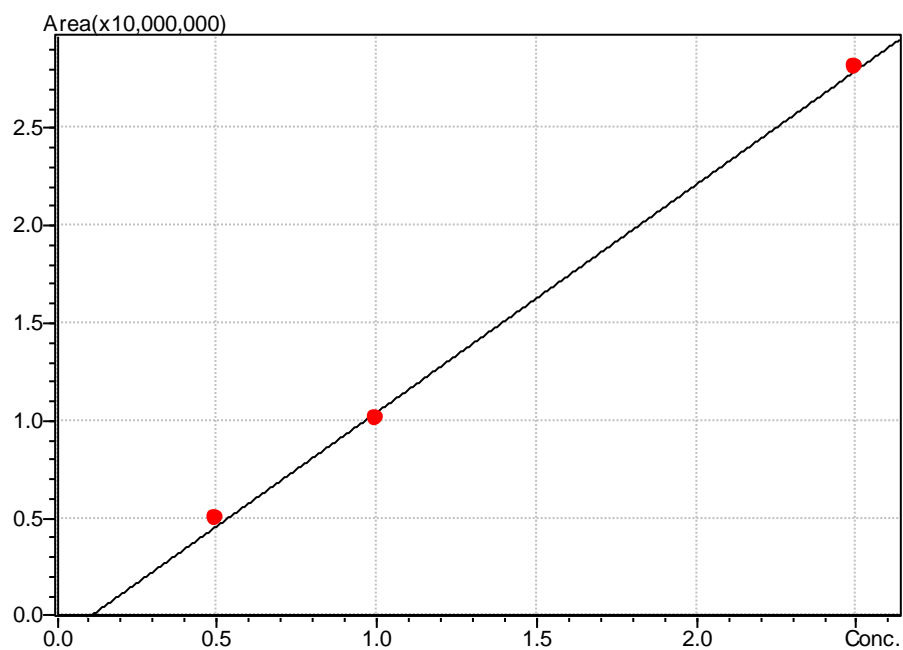


Figure C.3. Calibration curve for carbon monoxide.

$$Y = aX + b$$

$$a = 1.168457 \times 10^7$$

$$b = -1198152$$

$$R^2 = 0.9991273$$

$$R = 0.9995635$$

$$\text{Mean RF} : 1.040642 \times 10^7$$

$$\text{RF SD} : 733330.9$$

$$\text{RF \%RSD} : 7.046911$$

C.1.4 Hydrogen

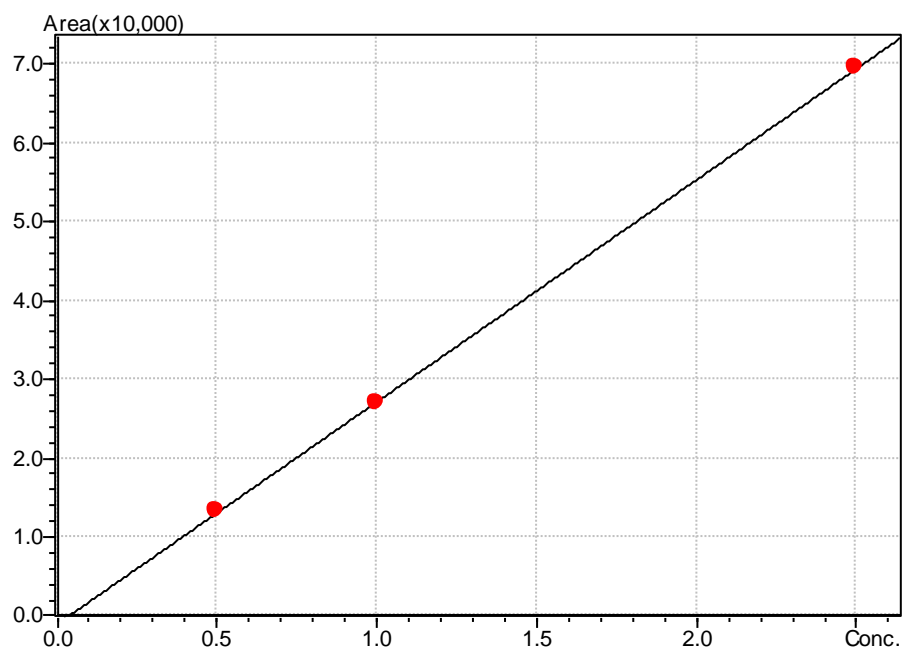


Figure C.4. Calibration curve for hydrogen.

$$Y = aX + b$$

$$a = 28177.91$$

$$b = -957.2831$$

$$R^2 = 0.9999700$$

$$R = 0.9999850$$

$$\text{Mean RF} : 27128.64$$

$$\text{RF SD} : 645.3993$$

$$\text{RF \%RSD} : 2.379033$$

C.1.5 Oxygen

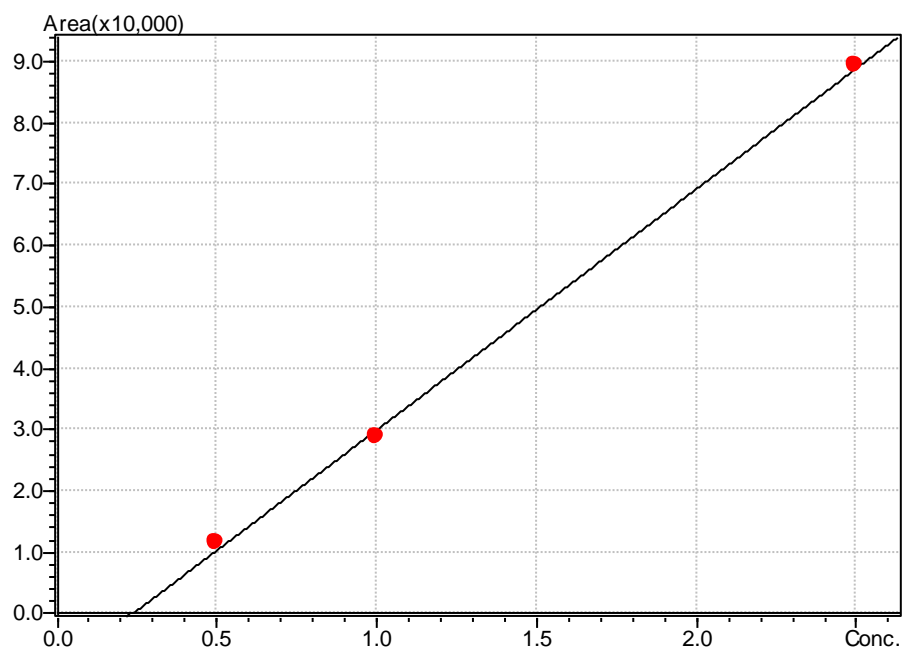


Figure C.5. Calibration curve for oxygen.

$$Y = aX + b$$

$$a = 39269.29$$

$$b = -9154.454$$

$$R^2 = 0.9991745$$

$$R = 0.9995872$$

$$\text{Mean RF} : 29154.91$$

$$\text{RF SD} : 6418.117$$

$$\text{RF \%RSD} : 22.01385$$

C.1.6 Nitrogen

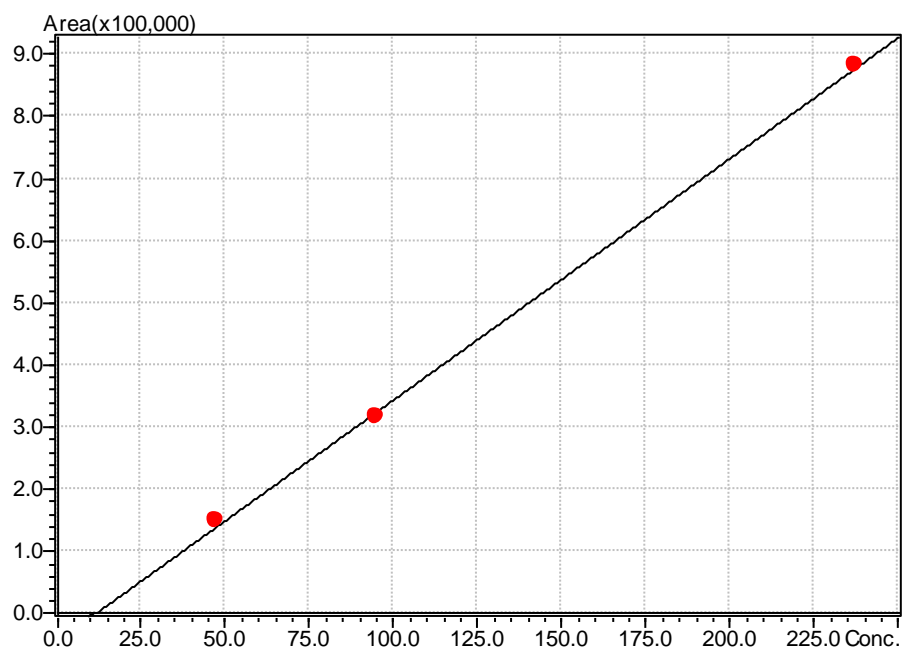


Figure C.6. Calibration curve for nitrogen.

$$Y = aX + b$$

$$a = 3885.657$$

$$b = -43382.52$$

$$R^2 = 0.9995371$$

$$R = 0.9997685$$

$$\text{Mean RF} : 3387.422$$

$$\text{RF SD} : 301.5211$$

$$\text{RF \%RSD} : 8.901197$$

C.2 SAMPLE CHROMATOGRAM

This section shows a sample chromatogram to exemplify the analyses made by the gas chromatograph. The chromatogram shown below was for CO₂ dissociation using

microhollow cathode discharge reactor at different applied voltages and an inlet flow rate of 100 mL/min. The gas samples were taken at the reactor effluent using a 250- μ L syringe, and injected into the gas chromatograph. The results of the analysis of gas chromatograph are given in terms of chromatograms as shown below. The gas appears at a particular time, called retention time, on chromatograms and the area under each peak is used to find the corresponding gas concentration using the calibration results shown in the previous section.

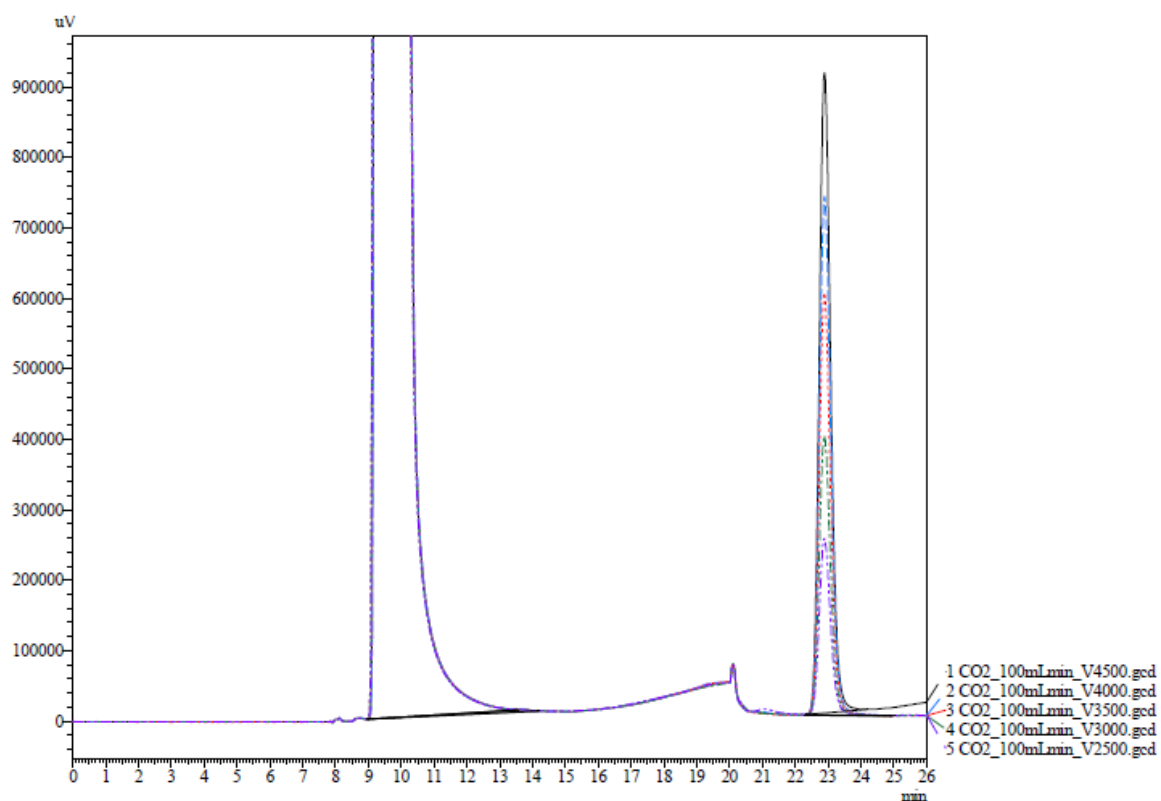


Figure C.7. Sample chromatogram of Channel 1 (FID) of the gas chromatograph for CO₂ dissociation at different applied voltages and an inlet flow rate of 100 mL/min.

Table C.1. Sample gas chromatograph results of Channel 1 (FID) for CO₂ dissociation at different applied voltages and inlet flow rate of 100 mL/min.

CO₂

Title	Sample Name	Sample ID	Ret.Time	Area	Height	Area%	Conc.	Units
CO2_100mLmin_V4500.gcd	CO2 4500 V	15	9.369	1752996629	51989589	98.755	98.490	mol %
CO2_100mLmin_V4000.gcd	CO2 4000 V	14	9.373	1763504091	52210900.8	98.990	95.902	mol %
CO2_100mLmin_V3500.gcd	CO2 3500 V	13	9.336	1844996852	53772042.4	99.214	98.868	mol %
CO2_100mLmin_V3000.gcd	CO2 3000 V	12	9.332	1858569894	54127815.7	99.485	99.595	mol %
CO2_100mLmin_V2500.gcd	CO2 2500 V	11	9.335	1831471626	53629438.6	99.670	99.117	mol %

CO

Title	Sample Name	Sample ID	Ret.Time	Area	Height	Area%	Conc.	Units
CO2_100mLmin_V4500.gcd	CO2 4500 V	15	22.887	22098235	908082.1	1.245	1.159	mol %
CO2_100mLmin_V4000.gcd	CO2 4000 V	14	22.89	17988785.3	736223.2	1.010	1.005	mol %
CO2_100mLmin_V3500.gcd	CO2 3500 V	13	22.883	14616998.5	599638.9	0.786	0.897	mol %
CO2_100mLmin_V3000.gcd	CO2 3000 V	12	22.884	9620028.9	395786.4	0.515	0.591	mol %
CO2_100mLmin_V2500.gcd	CO2 2500 V	11	22.885	6061932.1	249815.4	0.330	0.303	mol %

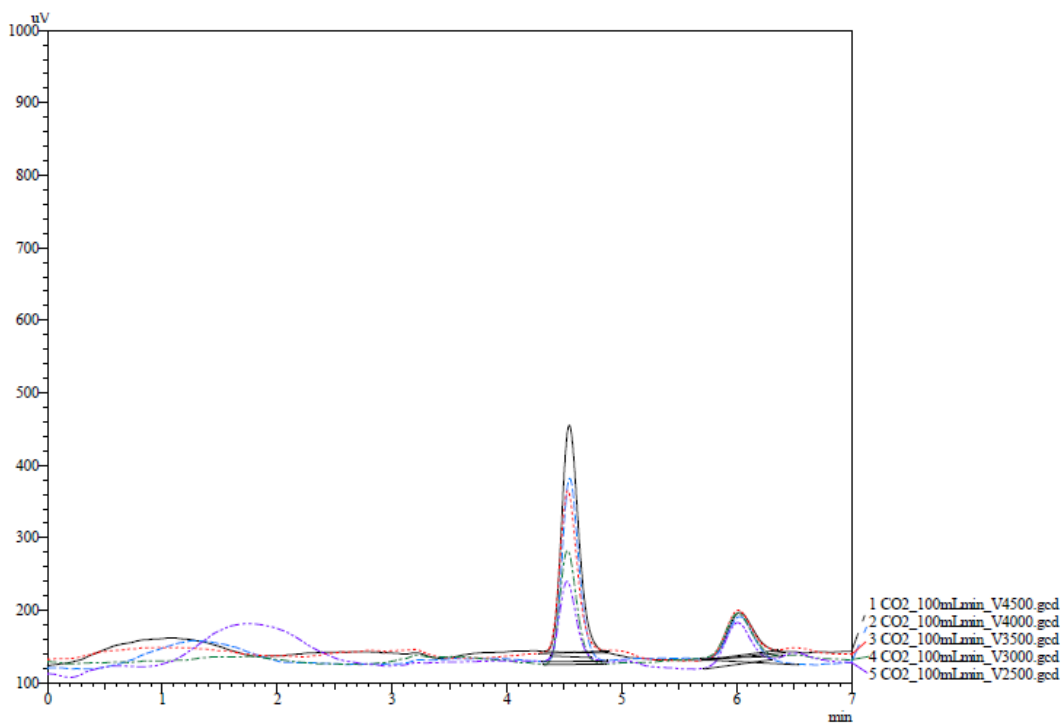


Figure C.8. Sample chromatogram of Channel 2 (TCD) of the gas chromatograph for CO₂ dissociation at different applied voltages and an inlet flow rate of 100 mL/min.

Table C.2. Sample gas chromatograph results of Channel 2 (TCD) for CO₂ dissociation at different applied voltages and inlet flow rate of 100 mL/min.

O₂

Title	Sample Name	Sample ID	Ret. Time	Area	Height	Area%	Conc.	Units
CO2_100mLmin_V4500.gcd	CO2 4500 V	15	4.544	3254.2	312.2	76.530	0.074	mol%
CO2_100mLmin_V4000.gcd	CO2 4000 V	14	4.548	2597.6	251.9	71.678	0.067	mol%
CO2_100mLmin_V3500.gcd	CO2 3500 V	13	4.531	2348.5	222.4	70.807	0.067	mol%
CO2_100mLmin_V3000.gcd	CO2 3000 V	12	4.529	1630.6	156.8	62.795	0.047	mol%
CO2_100mLmin_V2500.gcd	CO2 2500 V	11	4.525	994.6	103.3	53.729	0.005	mol%

N₂

Title	Sample Name	Sample ID	Ret. Time	Area	Height	Area%	Conc.	Units
CO2_100mLmin_V4500.gcd	CO2 4500 V	15	6.028	998	60.8	23.470	0.220	mol%
CO2_100mLmin_V4000.gcd	CO2 4000 V	14	6.028	1026.4	61.5	28.322	0.222	mol%
CO2_100mLmin_V3500.gcd	CO2 3500 V	13	6.018	968.3	62.1	29.193	0.207	mol%
CO2_100mLmin_V3000.gcd	CO2 3000 V	12	6.01	966.1	60.2	37.205	0.207	mol%
CO2_100mLmin_V2500.gcd	CO2 2500 V	11	6.007	856.5	56.6	46.271	0.202	mol%

Appendix D

Modeling of Electric Field Distribution in a Microhollow Cathode Discharge Reactor prior to Carbon Dioxide Dissociation

This appendix reports a numerical study on electric field distribution in a microhollow cathode discharge (MHCD) plasma reactor prior to carbon dioxide dissociation. These reactors can produce non-equilibrium plasmas and can be a promising technology for converting carbon dioxide into valuable chemicals and renewable fuels. However, these applications are currently in their early stages. In order to understand the effects of major design and operational parameters on the reactor performance of a MHCD system, electric field distribution was modeled and simulated before the first discharge occurred. In this study, different types of dielectrics including mica, alumina, acrylic and quartz were used, and applied DC voltage was varied from 250 to 10,000 V. First the operating voltage regions of this reactor were determined based on the breakdown thresholds of the dielectric and gas phase. Then, the effects of applied voltage on the discharge volume and power requirement of operation were determined. Results showed that the reactor with mica as the dielectric material showed the largest operating voltage range, as well as the highest power requirement. In addition, the discharge volume increased with applied voltage and it was possible to discharge about 96% of the gas in the MHCD reactor with mica at 10 kV.

Prior to this study, a number of modeling studies have been published for the use of microdischarge plasma reactors. For instance, Kothnur *et al.* [106] modeled 1-D, parallel-plate DC microdischarge plasma reactor with a dielectric gap of 250 μm using helium at a pressure of 250 Torr. They showed that the gas temperature in the discharge gap could be as high as 1500 K, even for voltages about 200 V. Additionally, Kushner

[107] numerically investigated the dynamics and transport of plasma in a cylindrical microdischarge device. He also analyzed multistage microdischarge reactors where two metal-dielectric-metal configurations were stacked together. The peak electron densities and gas temperatures of a multistage reactor were comparable to those of a single-stage reactor, and the current was shared equally by each stage. In another study, a tubular microdischarge thruster was modeled for microsattellites by Sitaraman and Raja [18]. Argon was fed to the thruster, and a peak voltage of 600 V was applied at either 10 or 20 MHz, and thrust of 278 μN and power dissipation of 84 mW were estimated at 20 MHz with an flow rate of 0.55 mg/s.

This appendix reports a simple model to assist the material choice and applied voltage selection in a microdischarge plasma reactor, specifically a microhollow cathode discharge (MHCD) plasma reactor for CO_2 dissociation in terms of avoiding dielectric breakdown, discharge gas volume and power consumption.

D.1 MODELING ANALYSIS

Figure 3.1 shows the schematic of the system modeled in this study. The system consisted of a dielectric material with a thickness of 150 μm and two electrodes aligned as shown in Figure 3.1. Each electrode had a thickness of 10 μm . A hole was featured through these three layers with a diameter of 400 μm . These dimensions were chosen based on a MHCD reactor prototyped in this dissertation. The length and width of materials were sufficiently large not to affect the electric field in the hole. The hole was filled with pure carbon dioxide at a pressure of 1 atm and temperature of 20°C. Finally, it was assumed that during the operation of the reactor the material properties were constant at the system temperature and pressure, i.e., it was assumed that non-thermal plasma conditions were satisfied.

D.1.1 Governing Equation

In order to estimate the volume of CO₂ discharge, the volume of the reactor was calculated in which the local electric field was larger than the breakdown threshold of CO₂. For this, the electric field distribution within the plasma reactor was determined from the charge conservation equation according to [147-149],

$$\frac{\partial \rho}{\partial t} + \nabla \cdot \vec{J} = 0 \quad (\text{D.1})$$

where ρ is the electric charge density in C/m³, t is the time in s, and J is the current density in A/m². The current density can be written in terms of electric field, E , without an external current source as follows [149],

$$\vec{J} = \left(\sigma + \varepsilon_o \varepsilon_r \frac{\partial}{\partial t} \right) \vec{E} \quad (\text{D.2})$$

where σ is the electrical conductivity in S/m, f is the frequency in Hz, ε_o is the permittivity of vacuum which is constant and equal to 8.854×10^{-12} F/m, ε_r is the relative permittivity which is the ratio of absolute permittivity of a material to the permittivity of vacuum, and E is the electric field in V/m. The electric field can be given as [148, 149],

$$\vec{E} = -\nabla V \quad (\text{D.3})$$

where V is the electrical voltage.

Finally, the theoretical power required to discharge the gas in the MHCD reactor was calculated as [150],

$$P = \int_{\forall} \vec{J} \cdot \vec{E} d\forall \quad (\text{D.4})$$

where \forall is the volume of the reactor in m³.

D.1.2 Boundary and Initial Conditions

Due to symmetry, the electrode choice to apply voltage was arbitrary, and according to the configuration given in Figure 3.1a, the top electrode was grounded and the bottom electrode was subjected to DC voltage such that,

$$\begin{aligned} V_{top} &= 0 \\ V_{bottom} &= V_{applied} \end{aligned} \quad (D.5)$$

where $V_{applied}$ is the applied voltage in V. In this study, the applied voltage was varied from 250 to 10,000 V to dissociate CO₂. The outer surfaces and the inlet and exit ports of the reactor were taken as electrically insulated such that,

$$\hat{n} \cdot \vec{J} = 0 \quad (D.6)$$

Initially, the electric field in the system was zero.

D.1.3 Material Properties

Finally, Table D.1 summarizes the material properties used in this study, including the electrical conductivity and relative permittivity of the electrodes, dielectric materials and gas.

D.1.4 Method of Solution

The electric field distribution in the system was solved using AC/DC module of COMSOL Multiphysics[®] version 4.3, finite element analysis software. A 3-D tetrahedral mesh which consists of 50,314 elements was applied for finite element analysis.

Moreover, the breakdown electric field was solved iteratively as in Section 2.2.3, and applied as the threshold value for the discharge formation to the electric field obtained from finite element analyses. Based on these equations, the breakdown electric

Table D.1. Electrical properties of the materials used in MHCD plasma reactor simulations at room temperature and pressure [151].

Material	Electrical Conductivity σ (S/m)	Relative Permittivity ϵ_r	Breakdown Electric Field E_{br} (V/m)	Reference
<i>Dielectric</i>				
Acrylic	1.00×10^{-18}	2.6	19.7×10^6	[152-154]
Alumina	1.00×10^{-15}	10.1	13.4×10^6	[154-156]
Quartz	1.00×10^{-12}	4.2	13.8×10^6	[154, 157]
Mica	2.01×10^{-15}	6.0	118×10^6	[154, 157]
<i>Electrode</i>				
Aluminum	3.77×10^7	1.0	-	[157]
<i>Medium</i>				
CO ₂	5.00×10^{-15}	1.0	<i>from Paschen curve</i>	[158]

field of CO₂ was calculated as 1.2×10^7 V/m at the dielectric gap of 400 μm . With this threshold value, it was possible to estimate the discharge gas volume by integrating the differential volumes in which the electric field is greater than the breakdown electric field.

Additionally, a sensitivity analysis was performed to ensure that the obtained parameters were independent of mesh size and convergence criteria for the case with aluminum electrodes and quartz as the dielectric material. When the number of mesh elements increased from 50,314 to 100,065, the relative difference between the electric field values was within 0.4%, but the simulation time was doubled. Additionally, the convergence criterion was decreased by an order of magnitude, and the results were in agreement within 0.01%. All simulations were performed on a computer with 64-bit Intel Xeon E5430 processor at 2.66 GHz and 16.0 GB of RAM.

D.2 SIMULATION RESULTS

D.2.1 Effects of Dielectric Material and Applied Voltage

In simulations, MHCD plasma reactor was considered with aluminum electrodes and different dielectric materials, and the operating voltage range of the reactor for each material was identified. Figure D.1 shows the maximum electric field in the dielectric materials and in CO₂ as the gas phase as a function of applied voltage. The figure also shows the corresponding breakdown electric fields of the dielectric materials as given in Table D.1, as well as the electric field required to discharge CO₂. Both electric fields increased linearly with the applied voltage, where the field in the gas phase had a larger gradient than that in the dielectrics.

The operating range of the MHCD plasma reactor can be defined as the voltage region for which the electric field was larger than the breakdown threshold of the gas phase and smaller than the breakdown threshold of the dielectric. In this way, the discharge occurs in the gas phase rather than in the dielectric. Figure D.1 shows that the dielectric materials can be listed from the largest to the smallest operating range as mica, acrylic, quartz and alumina. Table D.2 summarizes the lower and upper voltage limits of the MHCD reactor with each dielectric material. From these results, it can be concluded that the dielectric with greater breakdown electric field should be used for a larger operating voltage range of MHCD plasma reactor. Additionally, the lower limit did not depend on the dielectric material and found to be 1 kV. Moreover, dielectrics with higher relative permittivity showed lower maximum electric fields in the gas phase.

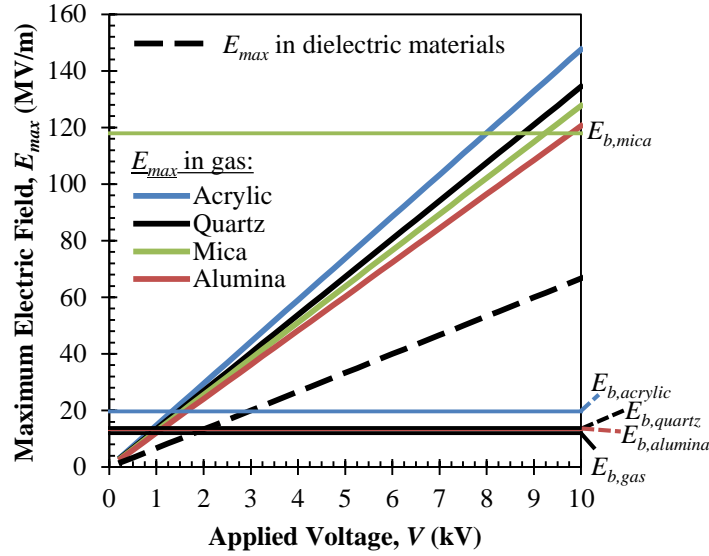


Figure D.1. Maximum electric field in the gas and the dielectric as a function of applied voltage for the microdischarge plasma reactor with aluminum electrodes.

Table D.2. Lower and upper limits for operating voltage range of microdischarge plasma reactor.

Dielectric	Lower Voltage Limit (V)	Upper Voltage Limit (V)
Mica	1000	> 10,000
Acrylic	1000	3,250
Quartz	1000	2,500
Alumina	1000	2,500

Figure D.2 shows the estimated volume of the discharged CO₂ as a function of the applied voltage within the working voltage range of the MHCD reactor with aluminum electrodes and mica as dielectric material. Results with mica were given here since it had the largest operating voltage range among the other investigated dielectric materials. As the applied voltage increased, the dissociated gas volume approached to the total gas volume in the reactor. The figure indicates that the discharge volume increased to about 93% of the total reactor volume at an applied voltage of 10 kV. Thus, it is suggested to

apply voltages near the dielectric breakdown threshold of the dielectric material to maximize the discharge gas volume. Similar results were obtained for other dielectric materials within their operating voltage ranges.

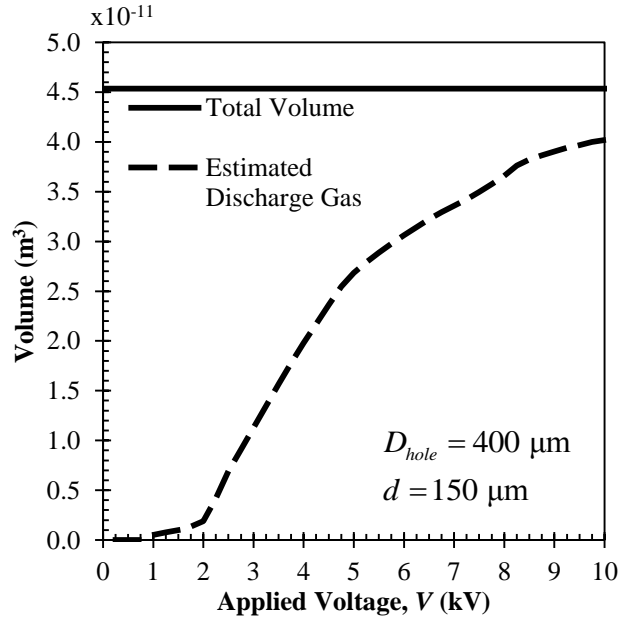


Figure D.2. Estimated discharge gas volume as a function of applied voltage for the MHCD plasma reactor with aluminum electrodes and mica as the dielectric material.

In addition, Figure D.3 shows the electrical power required to discharge CO₂ as a function of applied voltage for the operating voltage ranges of each dielectric material. As in the previous cases, aluminum electrodes were considered in this figure. It shows that the power requirements increased with applied voltage quadratically. As in the operating voltage ranges, the power requirement of a dielectric with higher breakdown voltage was higher. Thus, reactor with mica had the highest and the reactor with alumina had the lowest power requirement among the investigated four dielectric materials. At 1 kV, reactors with mica, acrylic, quartz and alumina required power of 0.22, 0.11, 0.08

and 0.002 W, respectively, whereas the power requirements increased to 1.38, 0.68, 0.52 and 0.008 W at 2.5 kV.

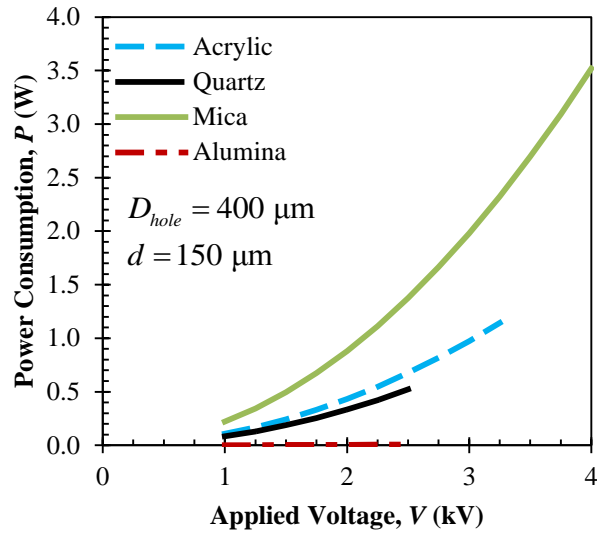


Figure D.3. Required power as a function of applied voltage for the MHCD plasma reactor with aluminum electrodes.

D.2.2 Effects of Hole Size and Dielectric Thickness

The simulations were also performed to investigate the effects of geometrical parameters of the MHCD reactor on electric field distribution and estimated discharge CO_2 volume. In these simulations, mica was selected as the dielectric material since it showed the highest operating range among the other investigated dielectric materials. The results showed that the discharge hole diameter, D_{hole} , did not affect the maximum electric field strength in both dielectric and gas. Additionally, Figure D.4 shows the estimated discharge CO_2 volume as functions of hole diameter from 100 to 900 μm , and the ratio of the estimated discharge volume to the total volume of the gas in the discharge hole. The results showed that the estimated discharge volume increased with increasing

hole diameter, and at a hole diameter of 400 μm , it was possible to discharge about 92% of the total gas volume in the discharge hole. Based on the electric field distribution, this volume ratios were lower at other hole sizes and varied between 60% and 92% as shown in Figure D.4.

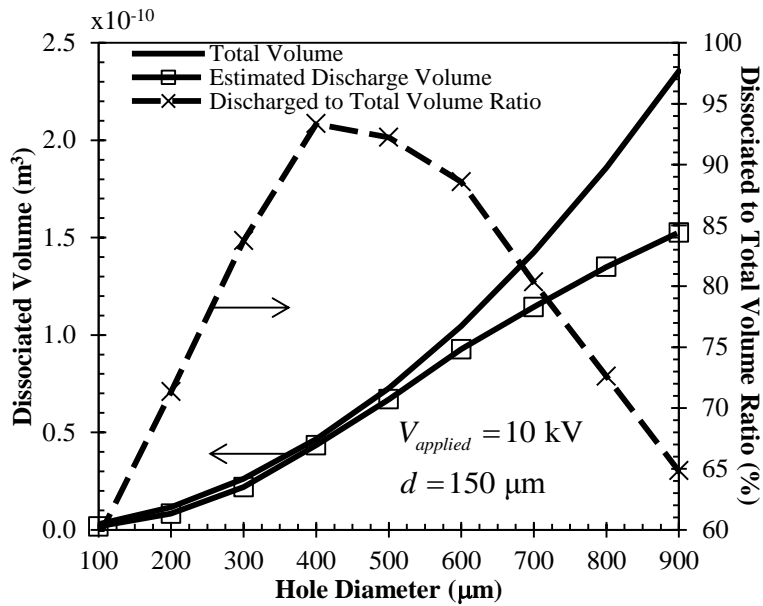


Figure D.4. Estimated discharge gas volume as a function of discharge hole diameter of the MHCD plasma reactor at an applied voltage of 10 kV with aluminum electrodes and mica as the dielectric material.

Moreover, the dielectric thickness was varied from 300 to 1000 μm and its effect on the electric field distribution was analyzed at an applied voltage of 10 kV and a discharge hole diameter of 400 μm . The simulation results showed that the maximum electric field in the reactor decreased as the dielectric thickness increased. At a constant applied voltage, thicker dielectric material showed lower electric field strength as electric field is a function of distance between the electrodes. Additionally, Figure D.5 shows the estimated discharge CO_2 volume as functions of dielectric thickness from 300 to 1000

μm , and the ratio of the estimated discharge volume to the total volume of the gas in the discharge hole. The results showed that the estimated discharge volume increased linearly with dielectric thickness, whereas the estimated discharge gas volume to total volume varied between 86% and 92%. The maximum ratio was observed as 91.6% at a dielectric thickness of 300 μm and the minimum was observed as 86.6% at a dielectric thickness of 700 μm .

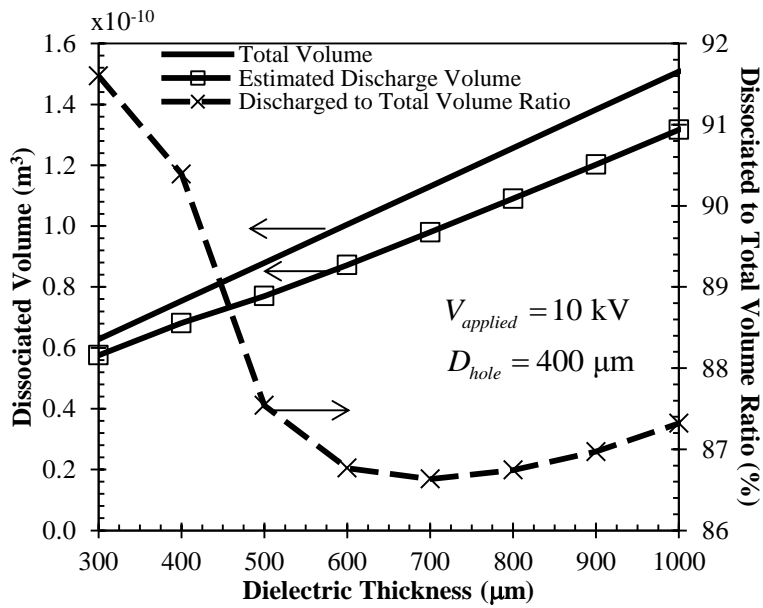


Figure D.5. Estimated discharge gas volume as a function of dielectric thickness of the MHCD plasma reactor at an applied voltage of 10 kV with aluminum electrodes and mica as the dielectric material.

D.3 MODELING SUMMARY

A numerical study was performed on the electric field in a MHCD plasma reactor prior to discharge in order to assist the design of the reactor for higher CO_2 dissociation. The effects of dielectric materials, applied voltage, discharge hole diameter and dielectric thickness on the electric field, discharge volume and power requirement were investigated through a three-dimensional finite element model. Based on the electric field

distribution and the breakdown electric field values of the gas and the dielectric material, operating voltage ranges were identified for each analyzed case. For each operating voltage range, discharge CO₂ volume and power requirement of the reactor were calculated. Based on the obtained results the following conclusions can be made:

- Dielectric material choice affected the operating voltage range of MHCD plasma reactor, as different dielectric materials showed different maximum electric fields in the dielectric. Mica had the largest operating range, whereas acrylic showed the highest electric field in the gas phase.
- Electric field in the gas phase and in the dielectric material increased linearly with applied voltage. However, electric field in the dielectric material was independent of the dielectric material.
- Estimated discharge gas volume increased with increasing applied voltage for all the dielectric materials. A MHCD reactor with mica as dielectric material could discharge up to 93% of CO₂ in the reactor at 10 kV.
- Power requirement increased quadratically with increasing applied voltage. Mica showed the highest power requirement which was two orders of magnitude higher than the power requirement of alumina.
- The estimated discharge volume increased with increasing hole size and dielectric thickness. However, the ratio of estimated discharge volume to the total volume of the gas showed the highest value as 93% at a discharge hole diameter of 400 μm and a dielectric thickness of 150 μm. This ratio was lower for the reactor with thicker dielectric layer.

Although the results of this model overestimated the experimental results, they were able to capture the trends of the experimental results.

References

- [1] International Energy Agency. Global carbon-dioxide emissions increase by 1.0 Gt in 2011 to record high. IEA Newsroom: OECD/IEA; 2012.
- [2] Kirkpatrick AT. Carbon dioxide dissociation applet. Fort Collins, CO: The College of Engineering at Colorado State University; 1996.
- [3] Nowotny J, Sorrell C, Sheppard L, Bak T. Solar-hydrogen: Environmentally safe fuel for the future. *International Journal of Hydrogen Energy*. 2005;30:521-44.
- [4] Yanpeng S, Yong N, Angshan W, Dengxiang J, Fengwen Y, Jianbing J. Carbon dioxide reforming of methane to syngas by thermal plasma. *Plasma Science and Technology*. 2012;14:252.
- [5] Bromberg L, Cohn DR, Rabinovich A, Alexeev N, Samokhin AV, Hadidi K, et al. Onboard plasmatron hydrogen production for improved vehicles. Cambridge, MA: Plasma Science and Fusion Center, Massachusetts Institute of Technology; 2006.
- [6] Bromberg L, Cohn DR, Rabinovich A, O'Brien C, Hochgreb S. Plasma reforming of methane. *Energy & Fuels*. 1998;12:11-8.
- [7] Li D, Li X, Bai M, Tao X, Shang S, Dai X, et al. CO₂ reforming of CH₄ by atmospheric pressure glow discharge plasma: A high conversion ability. *International Journal of Hydrogen Energy*. 2009;34:308-13.
- [8] Liu C-j, Xu G-h, Wang T. Non-thermal plasma approaches in CO₂ utilization. *Fuel Processing Technology*. 1999;58:119-34.
- [9] Gesser H, Hunter N, Probawono D. The CO₂ reforming of natural gas in a silent discharge reactor. *Plasma Chemistry and Plasma Processing*. 1998;18:241-5.

- [10] Tao X, Bai M, Li X, Long H, Shang S, Yin Y, et al. CH₄-CO₂ reforming by plasma-challenges and opportunities. *Progress in Energy and Combustion Science*. 2011;37:113-24.
- [11] Shimizu T, Sakiyama Y, Graves DB, Zimmermann JL, Morfill GE. The dynamics of ozone generation and mode transition in air surface micro-discharge plasma at atmospheric pressure. *New Journal of Physics*. 2012;14:103028.
- [12] Hensel K, Machala Z, Tardiveau P. Capillary microplasmas for ozone generation. *European Physical Journal, Applied Physics*. 2009;47:R55.
- [13] Sung Y-M, Sakoda T. Optimum conditions for ozone formation in a micro dielectric barrier discharge. *Surface and Coatings Technology*. 2005;197:148-53.
- [14] Mariotti D, Sankaran RM. Microplasmas for nanomaterials synthesis. *Journal of Physics D: Applied Physics*. 2010;43:323001.
- [15] Shimizu Y, Sasaki T, Chandra Bose A, Terashima K, Koshizaki N. Development of wire spraying for direct micro-patterning via an atmospheric-pressure UHF inductively coupled microplasma jet. *Surface and Coatings Technology*. 2006;200:4251-6.
- [16] Becker K, Koutsospyros A, Yin S-M, Christodoulatos C, Abramzon N, Joaquin J, et al. Environmental and biological applications of microplasmas. *Plasma Physics and Controlled Fusion*. 2005;47:B513.
- [17] Choi JH, Han I, Baik HK, Lee MH, Han D-W, Park J-C, et al. Analysis of sterilization effect by pulsed dielectric barrier discharge. *Journal of Electrostatics*. 2006;64:17-22.

- [18] Sitaraman H, Raja L. Simulation studies of RF excited micro-cavity discharges for micro-propulsion applications. *Journal of Physics D: Applied Physics*. 2012;45:185201.
- [19] Holt G, Stewart S, Mauldin J, Campbell T, Eckhoff P, Elmasri H, et al. Relative navigation, microdischarge plasma thruster, and distributed communications experiments on the FASTRAC Mission. 17th Annual AIAA/USU Conference on Small Satellites 2003.
- [20] Sitaraman H, Raja L. Simulation studies of alternating-current microdischarges for microthruster applications. *Proceedings of the 48th AIAA Aerospace Sciences Meeting, AIAA-2010-231-2010* 2010.
- [21] Deconinck T, Mahadevan S, Raja LL. Computational simulation of coupled nonequilibrium discharge and compressible flow phenomena in a microplasma thruster. *Journal of Applied Physics*. 2009;106:063305-13.
- [22] Deconinck T, Mahadevan S, Raja LL. Simulation of a direct-current microdischarge for the micro plasma thruster. *Plasma Science, IEEE Transactions on*. 2008;36:1200-1.
- [23] Iza F, Kim GJ, Lee SM, Lee JK, Walsh JL, Zhang YT, et al. Microplasmas: Sources, particle kinetics, and biomedical applications. *Plasma Processes and Polymers*. 2008;5:322-44.
- [24] Stoffels E, Sakiyama Y, Graves DB. Cold atmospheric plasma: charged species and their interactions with cells and tissues. *Plasma Science, IEEE Transactions on*. 2008;36:1441-57.
- [25] Fridman A, Kennedy LA. *Plasma physics and engineering*. Boca Raton, FL: CRC; 2004.

- [26] Petitpas G, Rollier JD, Darmon A, Gonzalez-Aguilar J, Metkemeijer R, Fulcheri L. A comparative study of non-thermal plasma assisted reforming technologies. *International Journal of Hydrogen Energy*. 2007;32:2848-67.
- [27] Paulmier T, Fulcheri L. Use of non-thermal plasma for hydrocarbon reforming. *Chemical Engineering Journal*. 2005;106:59-71.
- [28] Stark RH, Schoenbach KH. Direct current glow discharges in atmospheric air. *Applied Physics Letters*. 1999;74:3770-2.
- [29] Mohamed A-A, Block R, Schoenbach KH. Direct current glow discharges in atmospheric air. *Plasma Science, IEEE Transactions on*. 2002;30:182-3.
- [30] Lodes A, Curry R. Atmospheric glow discharge plasmas using a microhollow cathode device. *Pulsed Power Conference, 2009 PPC'09 IEEE: IEEE; 2009*. p. 975-9.
- [31] Gomes M, Sismanoglu B, Amorim J. Characterization of microhollow cathode discharges. *Brazilian Journal of Physics*. 2009;39:25-30.
- [32] Boeuf J, Pitchford L, Schoenbach K. Predicted properties of microhollow cathode discharges in xenon. *Applied Physics Letters*. 2005;86:071501--3.
- [33] Schoenbach KH, El-Habachi A, Shi W, Ciocca M. High-pressure hollow cathode discharges. *Plasma Sources Science and Technology*. 1997;6:468.
- [34] Foest R, Schmidt M, Becker K. Microplasmas, an emerging field of low-temperature plasma science and technology. *International Journal of Mass Spectrometry*. 2006;248:87-102.
- [35] Papadakis A, Rossides S, Metaxas A. Microplasmas: A review. *Open Applied Physics Journal*. 2011;4:45-63.

- [36] Taylan O, Berberoglu H. Fuel production using concentrated solar energy. In: Rugescu R, editor. Application of Solar Energy. Rijeka, Croatia: InTech; 2013. p. 33-67.
- [37] Steinfeld A, Palumbo R. Solar thermochemical process technology. Encyclopedia of Physical Science and Technology. 2001;15:237-56.
- [38] Steinfeld A, Meier A. Solar fuels and materials. Encyclopedia of Energy. Amsterdam: Elsevier; 2004. p. 623–37.
- [39] Baykara S. Experimental solar water thermolysis. International Journal of Hydrogen Energy. 2004;29:1459-69.
- [40] Steinfeld A. Solar hydrogen production via a two-step water-splitting thermochemical cycle based on Zn/ZnO redox reactions. International Journal of Hydrogen Energy. 2002;27:611-9.
- [41] Funke HH, Diaz H, Liang X, Carney CS, Weimer AW, Li P. Hydrogen generation by hydrolysis of zinc powder aerosol. International Journal of Hydrogen Energy. 2008;33:1127-34.
- [42] Abanades S, Charvin P, Lemont F, Flamant G. Novel two-step SnO₂/SnO water-splitting cycle for solar thermochemical production of hydrogen. International Journal of Hydrogen Energy. 2008;33:6021-30.
- [43] Meier A, Steinfeld A. Solar thermochemical production of fuels. Advances in Science and Technology. 2011;74:303-12.
- [44] Chueh WC, Haile SM. Ceria as a thermochemical reaction medium for selectively generating syngas or methane from H₂O and CO₂. ChemSusChem. 2009;2:735-9.
- [45] Kappauf T, Fletcher EA. Hydrogen and sulfur from hydrogen sulfide - VI. Solar thermolysis. Energy. 1989;14:443-9.

- [46] Zaman J, Chakma A. Production of hydrogen and sulfur from hydrogen sulfide. *Fuel Processing Technology*. 1995;41:159-98.
- [47] Steinfeld A. Solar thermochemical production of hydrogen - a review. *Solar Energy*. 2005;78:603-15.
- [48] Harvey WS, Davidson JH, Fletcher EA. Thermolysis of hydrogen sulfide in the temperature range 1350-1600 K. *Industrial & Engineering Chemistry Research*. 1998;37:2323-32.
- [49] Perret R. Solar thermochemical hydrogen production research (STCH), Thermochemical cycle selection and investment priority. Albuquerque, New Mexico and Livermore, California: Sandia National Laboratories; 2011.
- [50] Perkins C, Weimer AW. Solar-thermal production of renewable hydrogen. *AIChE Journal*. 2009;55:286-93.
- [51] Zedtwitz P, Steinfeld A. The solar thermal gasification of coal-energy conversion efficiency and CO₂ mitigation potential. *Energy*. 2003;28:441-56.
- [52] Maag G, Zanganeh G, Steinfeld A. Solar thermal cracking of methane in a particle-flow reactor for the co-production of hydrogen and carbon. *International Journal of Hydrogen Energy*. 2009;34:7676-85.
- [53] Hirsch D, Epstein M, Steinfeld A. The solar thermal decarbonization of natural gas. *International Journal of Hydrogen Energy*. 2001;26:1023-33.
- [54] Ozalp N, Kogan A, Epstein M. Solar decomposition of fossil fuels as an option for sustainability. *International Journal of Hydrogen Energy*. 2009;34:710-20.
- [55] Rodat S, Abanades S, Coulié J, Flamant G. Kinetic modelling of methane decomposition in a tubular solar reactor. *Chemical Engineering Journal*. 2009;146:120-7.

- [56] Abanades S, Flamant G. Hydrogen production from solar thermal dissociation of methane in a high-temperature fluid-wall chemical reactor. *Chemical Engineering and Processing: Process Intensification*. 2008;47:490-8.
- [57] Almodaris M, Khorasani S, Abraham JJ, Ozalp N. Simulation of solar thermo-chemical hydrogen production techniques. *ASME/JSME 2011 8th Thermal Engineering Joint Conference*. Honolulu, Hawaii, USA: ASME; 2011. p. T20059-17.
- [58] Rodat S, Abanades S, Flamant G. High-temperature solar methane dissociation in a multitubular cavity-type reactor in the temperature range 1823– 2073 K. *Energy & Fuels*. 2009;23:2666-74.
- [59] Yeheskel J, Epstein M. Thermolysis of methane in a solar reactor for mass-production of hydrogen and carbon nano-materials. *Carbon*. 2011;49:4695-703.
- [60] Abanades S, Flamant G. Experimental study and modeling of a high-temperature solar chemical reactor for hydrogen production from methane cracking. *International Journal of Hydrogen Energy*. 2007;32:1508-15.
- [61] Abanades S, Flamant G. Production of hydrogen by thermal methane splitting in a nozzle-type laboratory-scale solar reactor. *International Journal of Hydrogen Energy*. 2005;30:843-53.
- [62] Klein HH, Karni J, Rubin R. Dry methane reforming without a metal catalyst in a directly irradiated solar particle reactor. *Journal of Solar Energy Engineering*. 2009;131:021001.
- [63] Rodat S, Abanades S, Flamant G. Co-production of hydrogen and carbon black from solar thermal methane splitting in a tubular reactor prototype. *Solar Energy*. 2011;85:645-52.

- [64] Maag G, Rodat S, Flamant G, Steinfeld A. Heat transfer model and scale-up of an entrained-flow solar reactor for the thermal decomposition of methane. *International Journal of Hydrogen Energy*. 2010;35:13232-41.
- [65] Kamka F, Jochmann A, Picard L. Development status of BGL gasification. *International Freiberg Conference on IGCC & XtL Technologies*. Freiberg, Germany 2005. p. 1.
- [66] Higman C, Burgt Mvd. *Gasification*. Second ed. Oxford, UK: Gulf Professional Publishing; 2008.
- [67] Basu P. *Biomass gasification and pyrolysis: practical design and theory*. Burlington, MA: Academic Press; 2010.
- [68] Kodama T, Kondoh Y, Tamagawa T, Funatoh A, Shimizu K, Kitayama Y. Fluidized bed coal gasification with CO₂ under direct irradiation with concentrated visible light. *Energy & Fuels*. 2002;16:1264-70.
- [69] Aoki A, Ohtake H, Shimizu T, Kitayama Y, Kodama T. Reactive metal-oxide redox system for a two-step thermochemical conversion of coal and water to CO and H₂. *Energy*. 2000;25:201-18.
- [70] Flechsenhar M, Sasse C. Solar gasification of biomass using oil shale and coal as candidate materials. *Energy*. 1995;20:803-10.
- [71] Van Heek K. General aspects and engineering principles for technical application of coal gasification. In: Figueiredo JL, Moulijn JA, editors. *Carbon and Coal Gasification: Science and Technology*. Alvor, Portugal: Springer; 1986. p. 383-402.

- [72] Devi L, Ptasinski KJ, Janssen FJJG. A review of the primary measures for tar elimination in biomass gasification processes. *Biomass and Bioenergy*. 2003;24:125-40.
- [73] Weimer A, Perkins C, Mejjic D, Lichty P. Rapid solar-thermal conversion of biomass to syngas. In: Colorado TUo, editor. United States: WO Patent WO/2008/027,980; 2008.
- [74] Bellan PM. *Fundamentals of plasma physics*. Cambridge, UK: Cambridge University Press; 2006.
- [75] Fridman A. *Plasma chemistry*. New York, NY: Cambridge University Press; 2008.
- [76] Tendero C, Tixier C, Tristant P, Desmaison J, Leprince P. Atmospheric pressure plasmas: A review. *Spectrochimica Acta Part B: Atomic Spectroscopy*. 2006;61:2-30.
- [77] Kogelschatz U. Dielectric-barrier discharges: their history, discharge physics, and industrial applications. *Plasma Chemistry and Plasma Processing*. 2003;23:1-46.
- [78] Moreau E. Airflow control by non-thermal plasma actuators. *Journal of Physics D: Applied Physics*. 2007;40:605.
- [79] Forte M, Leger L, Pons J, Moreau E, Touchard G. Plasma actuators for airflow control: measurement of the non-stationary induced flow velocity. *Journal of Electrostatics*. 2005;63:929-36.
- [80] Becker K, Schoenbach K, Eden J. Microplasmas and applications. *Journal of Physics D: Applied Physics*. 2006;39:R55.

- [81] Fridman A, Gutsol A, Cho Y. Non-thermal atmospheric pressure plasma. In: Fridman A, Cho Y, editors. *Advances in Heat Transfer: Transport Phenomena in Plasma*. Oxford, UK: Elsevier; 2007. p. 1-142.
- [82] Meek JM, Craggs JD. *Electrical breakdown of gases*. London, UK: Oxford University Press; 1978.
- [83] Arora R, Mosch W. *High voltage and electrical insulation engineering*. Hoboken, NJ: Wiley-IEEE Press; 2010.
- [84] Raizer YP, Kisin VI, Allen JE. *Gas discharge physics*: Springer-Verlag Berlin; 1991.
- [85] Gutsol A. Symbiosis between low temperature plasma and high temperature chemistry. 20th International Symposium on Plasma Chemistry (ISPC-20). Philadelphia, PA 2011. p. 494.
- [86] Lindner PJ, Besser R. Hydrogen production by methanol reforming in a non-thermal atmospheric pressure microplasma reactor. *International Journal of Hydrogen Energy*. 2012;37:13338-49.
- [87] Subrahmanyam C, Magureanu M, Renken A, Kiwi-Minsker L. Catalytic abatement of volatile organic compounds assisted by non-thermal plasma: Part 1. A novel dielectric barrier discharge reactor containing catalytic electrode. *Applied Catalysis B: Environmental*. 2006;65:150-6.
- [88] Cal MP, Schluep M. Destruction of benzene with non-thermal plasma in dielectric barrier discharge reactors. *Environmental Progress*. 2004;20:151-6.
- [89] Jahanmiri A, Rahimpour M, Shirazi MM, Hooshmand N, Taghvaei H. Naphtha cracking through a pulsed DBD plasma reactor: Effect of applied voltage, pulse repetition frequency and electrode material. *Chemical Engineering Journal*. 2012.

- [90] Indarto A. A review of direct methane conversion to methanol by dielectric barrier discharge. *Dielectrics and Electrical Insulation, IEEE Transactions on*. 2008;15:1038-43.
- [91] Aghamir F, Matin NS, Jalili A, Esfarayeni M, Khodagholi M, Ahmadi R. Conversion of methane to methanol in an ac dielectric barrier discharge. *Plasma Sources Science and Technology*. 2004;13:707.
- [92] Indarto A, Choi JW, Lee H, Song HK. The kinetic studies of direct methane oxidation to methanol in the plasma process. *Chinese Science Bulletin*. 2008;53:2783-92.
- [93] Larkin DW, Lobban LL, Mallinson RG. The direct partial oxidation of methane to organic oxygenates using a dielectric barrier discharge reactor as a catalytic reactor analog. *Catalysis Today*. 2001;71:199-210.
- [94] Indarto A, Choi JW, Lee H, Song HK. Methane conversion using dielectric barrier discharge: comparison with thermal process and catalyst effects. *Journal of Natural Gas Chemistry*. 2006;15:87-92.
- [95] Okumoto M, Su Z, Katsura S, Mizuno A. Dilution effect with inert gas in direct methanol synthesis from methane using nonthermal plasma. *IEEE*; 1997. p. 2027-31.
- [96] Okumoto M, Mizuno A. Conversion of methane for higher hydrocarbon fuel synthesis using pulsed discharge plasma method. *Catalysis Today*. 2001;71:211-7.
- [97] Nozaki T, Hattori A, Okazaki K. Partial oxidation of methane using a microscale non-equilibrium plasma reactor. *Catalysis Today*. 2004;98:607-16.

- [98] Mfopara A, Kirkpatrick MJ, Odic E. Dilute methane treatment by atmospheric pressure dielectric barrier discharge: effects of water vapor. *Plasma Chemistry and Plasma Processing*. 2009;29:91-102.
- [99] Jun K, Jacobson JM. Effective carbon dioxide reduction into carbon monoxide using millichannel embedded in-line dielectric barrier discharge reactor. 14th International Conference on Miniaturized Systems for Chemistry and Life Sciences. Groningen, The Netherlands 2010. p. 321-3.
- [100] Liang WJ, Fang HP, Li J, Zheng F, Li JX, Jin YQ. Performance of non-thermal DBD plasma reactor during the removal of hydrogen sulfide. *Journal of Electrostatics*. 2011;69:206-13.
- [101] Kappes T, Schiene W, Hammer T. Energy balance of a dielectric barrier discharge reactor for hydrocarbon steam reforming. 8th International Symposium of High Pressure Low Temperature Plasma Chemistry. Pyhajarve, Estonia 2002. p. 196-200.
- [102] Spencer LF, Gallimore AD. Efficiency of CO₂ dissociation in a radio-frequency discharge. *Plasma Chemistry and Plasma Processing*. 2011;31:79-89.
- [103] Zheng G, Jiang J, Wu Y, Zhang R, Hou H. The mutual conversion of CO₂ and CO in dielectric barrier discharge (DBD). *Plasma Chemistry and Plasma Processing*. 2003;23:59-68.
- [104] Li XS, Zhu AM, Wang KJ, Xu Y, Song ZM. Methane conversion to C₂ hydrocarbons and hydrogen in atmospheric non-thermal plasmas generated by different electric discharge techniques. *Catalysis Today*. 2004;98:617-24.
- [105] Shin J, Raja LL. Microdischarge-assisted ignition of dielectric-barrier high-pressure glow discharges. *Applied Physics Letters*. 2006;88:021502-3.

- [106] Kothnur PS, Yuan X, Raja LL. Structure of direct-current microdischarge plasmas in helium. *Applied Physics Letters*. 2003;82:529-31.
- [107] Kushner MJ. Modelling of microdischarge devices: plasma and gas dynamics. *Journal of Physics D: Applied Physics*. 2005;38:1633.
- [108] Qiu H, Martus K, Lee W, Becker K. Hydrogen generation in a microhollow cathode discharge in high-pressure ammonia–argon gas mixtures. *International Journal of Mass Spectrometry*. 2004;233:19-24.
- [109] Hsu DD, Graves DB. Microhollow cathode discharge reactor chemistry. *Plasma Chemistry and Plasma Processing*. 2005;25:1-17.
- [110] Delacourt C, Ridgway PL, Kerr JB, Newman J. Design of an electrochemical cell making syngas (CO+H₂) from CO₂ and H₂O reduction at room temperature. *Journal of The Electrochemical Society*. 2008;155:B42-B9.
- [111] Kumar B, Smieja JM, Sasayama AF, Kubiak CP. Tunable, light-assisted co-generation of CO and H₂ from CO₂ and H₂O by Re (bipy-tbu)(CO)₃Cl and p-Si in non-aqueous medium. *Chemical Communications*. 2011;48:272-4.
- [112] Furler P, Scheffe JR, Steinfeld A. Syngas production by simultaneous splitting of H₂O and CO₂ via ceria redox reactions in a high-temperature solar reactor. *Energy & Environmental Science*. 2012;5:6098-103.
- [113] Scheffe JR, Welte M, Steinfeld A. Thermal reduction of ceria within an aerosol reactor for H₂O and CO₂ splitting. *Industrial & Engineering Chemistry Research*. 2014.
- [114] Ermanoski I, Siegel NP, Stechel EB. A new reactor concept for efficient solar-thermochemical fuel production. *Journal of Solar Energy Engineering*. 2013;135:031002.

- [115] Smestad GP, Steinfeld A. Review: Photochemical and thermochemical production of solar fuels from H₂O and CO₂ using metal oxide catalysts. *Industrial & Engineering Chemistry Research*. 2012;51:11828-40.
- [116] Bader R, Venstrom LJ, Davidson JH, Lipiński W. Thermodynamic analysis of isothermal redox cycling of ceria for solar fuel production. *Energy & Fuels*. 2013;27:5533-44.
- [117] Jin F, Zeng X, Liu J, Jin Y, Wang L, Zhong H, et al. Highly efficient and autocatalytic H₂O dissociation for CO₂ reduction into formic acid with zinc. *Scientific Reports*. 2014;4.
- [118] Luggenhölscher D, Böhm P, Müller S, Du B, Sadeghi N, Czarnetzki U. Diagnostics of ns-microplasmas at atmospheric pressures 7th International Workshop on Microplasmas. Beijing, China: Tsinghua University; 2013.
- [119] Moran MJ, Shapiro HN. *Fundamentals of engineering thermodynamics*. Fifth ed: Wiley; 2006.
- [120] Hsu DD, Graves DB. Microhollow cathode discharge stability with flow and reaction. *Journal of Physics D: Applied Physics*. 2003;36:2898.
- [121] Aubert X, Bauville G, Guillon J, Lacour B, Puech V, Rousseau A. Analysis of the self-pulsing operating mode of a microdischarge. *Plasma Sources Science and Technology*. 2007;16:23.
- [122] Chabert P, Lazzaroni C, Rousseau A. A model for the self-pulsing regime of microhollow cathode discharges. *Journal of Applied Physics*. 2010;108:113307.
- [123] Lazzaroni C, Chabert P. Discharge resistance and power dissipation in the self-pulsing regime of micro-hollow cathode discharges. *Plasma Sources Science and Technology*. 2011;20:055004.

- [124] Lazzaroni C, Chabert P. A global model of the self-pulsing regime of micro-hollow cathode discharges. *Journal of Applied Physics*. 2012;111:053305--8.
- [125] Du B, Mohr S, Luggenhölscher D, Czarnetzki U. An atmospheric pressure self-pulsing micro thin-cathode discharge. *Journal of Physics D: Applied Physics*. 2011;44:125204.
- [126] Taylan O, Berberoglu H. Dissociation of carbon dioxide using a microdischarge plasma reactor. *ASME 2013 International Mechanical Engineering Congress & Exposition*. San Diego, California, USA: ASME; 2013. IMECE2013-64632.
- [127] Hutchinson IH. *Principles of plasma diagnostics*: Cambridge University Press; 2005.
- [128] Goldston RJ, Rutherford PH. *Introduction to plasma physics*: CRC Press; 1995.
- [129] Rousseau A, Aubert X. Self-pulsing microplasma at medium pressure range in argon. *Journal of Physics D: Applied Physics*. 2006;39:1619.
- [130] He S, Ouyang J, He F, Jia H. Self-pulsing operating mode of hollow cathode discharge in noble gas. *Physics of Plasmas*. 2012;19:023504.
- [131] Dong L, Ran J, Mao Z. Direct measurement of electron density in microdischarge at atmospheric pressure by Stark broadening. *Applied Physics Letters*. 2005;86:161501.
- [132] Qi B, Huang J, Gao L, Qiu Y. Electron density measurements in an atmospheric pressure argon discharge by means of plasma radiation. *Physics of Plasmas (1994-present)*. 2009;16:083301.
- [133] Shrestha R, Tyata R, Subedi D. Effect of applied voltage in electron density of homogeneous dielectric barrier discharge at atmospheric pressure. *Himalayan Physics*. 2013;4:10-3.

- [134] Augustynski J, Kedzierzawski P, Jermann B. Electrochemical reduction of CO₂ at metallic electrodes. In: Inui T, Anpo M, Izui K, Yanagida S, Yamaguchi T, editors. *Advances in Chemical Conversions for Mitigating Carbon Dioxide* 1998. p. 107-16.
- [135] Kedzierzawski P, Augustynski J. Poisoning and activation of the gold cathode during electroreduction of CO₂. *Journal of The Electrochemical Society*. 1994;141:L58-L60.
- [136] Deguchi M, Yotsuhashi S, Hashiba H, Yamada Y, Ohkawa K. Enhanced capability of photoelectrochemical CO₂ conversion system using an AlGa_N/Ga_N photoelectrode. *Japanese Journal of Applied Physics*. 2013;52:08JF7.
- [137] Chueh WC, Falter C, Abbott M, Scipio D, Furler P, Haile SM, et al. High-flux solar-driven thermochemical dissociation of CO₂ and H₂O using nonstoichiometric ceria. *Science*. 2010;330:1797-801.
- [138] Bradford M, Vannice M. CO₂ reforming of CH₄. *Catalysis Reviews*. 1999;41:1-42.
- [139] Fidalgo B, Menéndez J. Study of energy consumption in a laboratory pilot plant for the microwave-assisted CO₂ reforming of CH₄. *Fuel Processing Technology*. 2012;95:55-61.
- [140] Schoenbach K, Moselhy M, Shi W, Bentley R. Microhollow cathode discharges. *Journal of Vacuum Science & Technology A: Vacuum, Surfaces, and Films*. 2003;21:1260-5.
- [141] Kothnur P, Raja L. Simulation of direct-current microdischarges for application in electro-thermal class of small satellite propulsion devices. *Contributions to Plasma Physics*. 2007;47:9-18.

- [142] Osaki T, Mori T. Role of potassium in carbon-free CO₂ reforming of methane on K-promoted Ni/Al₂O₃ catalysts. *Journal of Catalysis*. 2001;204:89-97.
- [143] Lennon E, Burke A, Besser R. Operating modes and power considerations of microhollow cathode discharge devices with elongated trenches. *Current Applied Physics*. 2012;12:1064-73.
- [144] Sismanoglu B, Amorim J. Microhollow cathode discharge and breakdown in micron separations. *The European Physical Journal Applied Physics*. 2008;41:165-72.
- [145] Munoz-Serrano E, Hagelaar G, Callegari T, Boeuf J, Pitchford L. Properties of plasmas generated in microdischarges. *Plasma Physics and Controlled Fusion*. 2006;48:B391.
- [146] Ghorbanzadeh A, Lotfalipour R, Rezaei S. Carbon dioxide reforming of methane at near room temperature in low energy pulsed plasma. *International Journal of Hydrogen Energy*. 2009;34:293-8.
- [147] Howell JR, Siegel R, Menguc MP. *Thermal radiation heat transfer*. 5th ed. Boca Raton, FL: CRC Press; 2011.
- [148] Kovetz A. *Electromagnetic theory*. Cambridge, UK: Oxford University Press; 2000.
- [149] Celozzi S, Araneo R, Lovat G. *Electromagnetic shielding*. Hoboken, NJ: Wiley; 2008.
- [150] Deconinck TD. *Simulation studies of direct-current microdischarges for electric propulsion*. Austin, TX: University of Texas; 2008.

- [151] Taylan O, Berberoglu H. Dissociation of carbon dioxide using a non-thermal plasma reactor. ASME 2013 Summer Heat Transfer Conference. Minneapolis, MN: ASME; 2013. HT2013-17559.
- [152] Zheng W, Wong SC. Electrical conductivity and dielectric properties of PMMA/expanded graphite composites. *Composites Science and Technology*. 2003;63:225-35.
- [153] Xu K, Erricolo D, Dutta M, Strosio MA. Electrical conductivity and dielectric properties of PMMA/Graphite nanoplatelet ensembles. *Superlattices and Microstructures*. 2012.
- [154] Lide DR. *CRC handbook of chemistry and physics: A ready-reference book of chemical and physical data*. 80 ed. New York: CRC Press; 2000.
- [155] Krupka J, Derzakowski K, Riddle B, Baker-Jarvis J. A dielectric resonator for measurements of complex permittivity of low loss dielectric materials as a function of temperature. *Measurement Science and Technology*. 1999;9:1751.
- [156] Auerkari P. *Mechanical and physical properties of engineering alumina ceramics*. Finland: VTT Technical Research Center of Finland; 1996.
- [157] COMSOL. *COMSOL materials library*. 4.3 ed. Burlington, MA: COMSOL; 2012.
- [158] Michels A, Michels C. The Influence of pressure on the dielectric constant of carbon dioxide up to 1000 atmospheres between 25° and 150°C. *Philosophical Transactions of the Royal Society of London Series A, Containing Papers of a Mathematical or Physical Character*. 1933;231:409-34.